

MICROFIBROUS ENTRAPPED CATALYSTS AND SORBENTS:  
MICROSTRUCTURED HETEROGENEOUS CONTACTING  
SYSTEMS WITH ENHANCED EFFICIENCY

Except where reference is made to the work of others, the work described in this dissertation is my own or was done in collaboration with my advisory committee.  
This dissertation does not include proprietary or classified information.

---

Ranjeeth Reddy Kalluri

Certificate of Approval:

---

Yoon Y. Lee  
Professor  
Chemical Engineering

---

Bruce J. Tatarchuk, Chair  
Professor  
Chemical Engineering

---

W. Robert Ashurst  
Assistant Professor  
Chemical Engineering

---

Christopher J. Roy  
Affiliated Associate Professor  
Aerospace Engineering

---

Joe F. Pittman  
Interim Dean  
Graduate School

MICROFIBROUS ENTRAPPED CATALYSTS AND SORBENTS:  
MICROSTRUCTURED HETEROGENEOUS CONTACTING  
SYSTEMS WITH ENHANCED EFFICIENCY

Ranjeeth Reddy Kalluri

A Dissertation  
Submitted to  
the Graduate Faculty of  
Auburn University  
in Partial Fulfillment of the  
Requirements for the  
Degree of  
Doctor of Philosophy

Auburn, Alabama  
May 10, 2008

MICROFIBROUS ENTRAPPED CATALYSTS AND SORBENTS:  
MICROSTRUCTURED HETEROGENEOUS CONTACTING  
SYSTEMS WITH ENHANCED EFFICIENCY

Ranjeeth Reddy Kalluri

Permission is granted to Auburn University to make copies of this dissertation at its discretion, upon request of individuals or institutions and at their expense. The author reserves all publication rights.

---

Signature of Author

---

Date of Graduation

## VITA

Ranjeeth Reddy Kalluri, son of Chittaranjan Reddy Kalluri and Uma Devi Kalluri, was born in Hyderabad, Andhra Pradesh, India. He graduated from Atomic Energy Central School–III, Hyderabad, India in May 1996. He attended Little Flower Junior College in Hyderabad, India, from August 1996 to May 1998. He then entered Osmania University, Hyderabad, India in September, 1998, and graduated with a Bachelor of Technology degree in Chemical Engineering in May, 2002. He entered Graduate School at Auburn University, in August, 2002 for Doctorate of Philosophy.

DISSERTATION ABSTRACT

MICROFIBROUS ENTRAPPED CATALYSTS AND SORBENTS: NOVEL  
MICROSTRUCTURED HETEROGENEOUS CONTACTING  
SYSTEMS WITH ENHANCED EFFICIENCY

Ranjeeth R. Kalluri

Doctor of Philosophy, May 10, 2008  
(B. Tech., Osmania University, India, 2002)

215 Typed Pages

Directed by Bruce J. Tatarchuk

Catalyst/adsorbent particles were entrapped in sinter-locked networks of microfibers to form composite materials for use in heterogeneous catalysis and adsorption applications. These novel microstructured materials called as microfibrous entrapped catalysts/sorbents (MFECS), which have high voidages and uniform structures showed great enhancement in reaction rates and significant reduction in pressure drops in many heterogeneous contacting applications. In this work two different case studies - Hexane adsorption on activated carbon and Ozone catalytic decomposition for aircraft cabin air purification - were used to demonstrate and understand the anomalous reactivity enhancement in MFECS. Theoretical as well as experimental comparisons of MFECS

were made with the conventional reactor systems in both the cases. Further, 2D Computational Fluid Dynamics (CFD) studies were used to analyze the effect of fibers on mass transfer rates in these microstructured geometries.

Hexane breakthrough experiments showed that, the negative effect of the axial dispersion and channeling were predominantly present in packed beds of small particle diameters ( $< 3\text{mm}$ ). On the other hand, high voidages and uniformity of MFES decreased the axial dispersion and channeling effects and increased the radial dispersion of the adsorbate, thus improving the fluid phase mass transport rates.

In the ozone decomposition study, performance comparisons of microfibrous entrapped catalysts (MFEC) were made with monoliths of various cells per square inch (cpsi) and packed beds of various particle sizes for catalytic ozone decomposition. The analysis showed that the monoliths are severely affected by external mass transfer limitations, while the MFEC systems with lower pleat factor and packed beds were restricted by high pressure drops. But MFEC systems with higher pleat factor were able to combine the dual advantages of low pressure drops with high mass transfer rates and there by exceed the performance of the monoliths and packed beds.

Further, CFD analysis in 2D channel geometries showed that the presence of fibers caused significant improvement in mass transfer rates at higher Re numbers. This increase was found to be due to elimination of peaking velocities i.e. creation of plug flow conditions.

The two case studies and the CFD analysis have demonstrated the potential advantages of MFECS as heterogeneous contacting systems for use in high throughput applications as well as for applications requiring multi-log-removal capability.

## ACKNOWLEDGMENTS

Many people have helped me on my way to the successful completion of this dissertation and I would like to express my appreciation to all of them. Firstly, I would like to express my sincere gratitude to Dr. Bruce Tatarchuk for his financial support and guidance. I would like to acknowledge US Army (TARDEC) for funding this research. I would also like to acknowledge Dr. Yoon Lee, Dr. Robert Ashurst, and Dr. Chris Roy for serving on my committee. Thanks are also due to Dr. Daniel Harris for serving as the outside reader for this dissertation. I express my appreciation to all the members of Center for Microfibrous Materials Manufacturing for their kind help, especially Mr. Dwight Cahela, Dr. Don Cahela, Ms Megan Schumacher and Mr. Ron Putt. I am also thankful to Eric Luna, Hungyun Yang, Dan Kennedy, Robert Payne, Sachin Nair and Shirsh Punde for their useful discussions and thoughtful suggestions. I am also grateful to Sue Ellen Abner for the administrative support she has provided me throughout my graduate studies.

I thank Ravi Duggirala & Pavan Veluri for assistance with CFD softwares and their valuable friendship. I would like to thank Shilpa and Vivek Gaur for all their help and friendship. Thanks are also due to my best friends outside Auburn – Anand, Chakradhar, Krishna, Rajesh, Srikanth & Tarun for all the memorable time we spent together during our undergrad.

I am greatly indebted to my parents for inculcating in me the ability to think through issues creatively and logically. My sincere gratitude and appreciation are also due to my parents, my sister Rajini and my brother-in-law Hemambar for their constant love, encouragement and motivation, without which this dissertation would not have been possible. Finally, I would like to thank my wife Mani for supporting me in all the good and the difficult times, without whom it is impossible for me to visualize my life. With an immense gratification, I would like to dedicate this work to my parents and my wife.



Style manual or journal used: *Catalysis Today*

Computer software used: *Microsoft Word*

## TABLE OF CONTENTS

LIST OF TABLES .....	xvii
LIST OF FIGURES .....	xix
 CHAPTER I. INTRODUCTION AND LITERATURE REVIEW .....	 1
I.1. Motivation.....	1
I.2. Analogy between Catalytic reactors and Adsorption Systems .....	3
I.3. Microfibrous Entrapped Catalysts/Sorbents (MFEC/MFEC).....	3
I.3.1. Introduction .....	3
I.3.2. Method of Preparation.....	6
I.3.2.1. Pre-form Preparation .....	7
I.3.2.2. Pre-oxidation .....	8
I.3.2.3. Sintering.....	8
I.3.2.4. Catalyst/Active Material Impregnation .....	8
I.4. Heterogeneous Contacting Systems in Use .....	9
I.4.1. Packed Beds .....	10
I.4.2. Monolith Substrates .....	11
I.4.3. Catalytic Foams .....	13
I.4.4. Micro-Channel reactors .....	14
I.4.5. Wire Mesh Screens .....	15
I.4.6. Fluidized beds .....	16

I.5. Major Criteria in Reactor/Adsorbent Bed Design .....	17
I.6. Factors Affecting Reactor Performance.....	17
I.6.1. Surface Reaction Rate.....	18
I.6.2. Intraparticle Mass Transfer Rate.....	19
I.6.3. Fluid-Solid Interphase Mass Transfer Rate .....	19
I.6.4. Deviations from Plug Flow .....	21
I.6.4.1. Axial Molecular Diffusion.....	21
I.6.4.2. Interstitial Velocity Variations Due to Formation of (Parabolic) Velocity Profiles .....	22
I.6.4.3. Eddy diffusion (or turbulence) in axial direction .....	23
I.6.4.4. Wall Channeling.....	23
I.6.4.5. Intra-bed Channeling or Flow Maldistributions .....	24
I.6.5. Heat Transfer Rates .....	25
I.7. Catalyst/Adsorbent Characterization Techniques .....	26
I.7.1. Particle Size Characterization.....	26
I.7.2. Surface Area Measurements .....	27
I.7.3. Pore Size Distribution.....	28
I.7.4. Scanning Electron Microscopy .....	29
I.8. Computational Fluid Dynamics (CFD) .....	29
I.8.1. Discretization Method .....	31
I.8.2. Limitations of CFD.....	33

## CHAPTER II. HEXANE BREAKTHROUGH TESTS ON MFES AND PACKED

BEDS .....	34
II.1. Introduction.....	34
II.2. Experimental Details.....	35
II.2.1. Materials .....	35
II.2.2. Surface Characterization of Pica Activated carbon .....	36
II.2.3. Experimental Set-up.....	36
II.2.4. Experimental Breakthrough tests.....	39
II.2.5. Adsorption equilibrium experiments .....	41
II.3. Mathematical Model .....	42
II.3.1. Mass balance .....	43
II.3.2. Initial and boundary conditions .....	43
II.3.3. Gas phase mass transfer .....	43
II.3.4. Axial Dispersion .....	44
II.3.5. Intraparticle mass transfer.....	47
II.3.6. Adsorption isotherm and capacity calculation .....	48
II.3.7. Simplification and numerical solution of the governing equations .....	48
II.4. Results and Discussion .....	50
II.4.1. Surface Characterization.....	50
II.4.2. Equilibrium isotherm .....	51
II.4.3. Breakthrough tests .....	52
II.5. Conclusions.....	63
II.6. Nomenclature.....	64

CHAPTER III. COMPOSITE BED DESIGN .....	67
III.1. Background.....	67
III.2. Experimental details.....	68
III.3. Results and Discussion .....	69
III.4. Conclusions.....	70
CHAPTER IV. PRESSURE DROP TESTS .....	71
IV.1. Background.....	71
IV.2. Experimental details.....	72
IV.3. Mathematical Model .....	74
IV.4. Results and Discussion .....	74
IV.5. Conclusions.....	75
CHAPTER V. CATALYTIC OZONE DECOMPOSITION.....	76
V.1. Introduction.....	76
V.2. Mathematical Models for the Different reactors.....	78
V.2.1. Packed Beds.....	80
V.2.2. Monoliths .....	81
V.2.3. MFEC.....	83
V.2.4. Surface reaction rate .....	85
V.2.5. Performance Evaluation Criteria.....	85
V.3. Experimental Details.....	87
V.3.1. Materials and Methods.....	87

V.3.2. Commercial Monolith Based Catalytic Converter.....	89
V.3.3. Experimental Setup.....	89
V.3. Theoretical Results and Discussion .....	90
V.3.1. Comparisons among Packed Beds.....	90
V.3.2. Comparisons among Monoliths .....	93
V.3.3. Comparisons among MFEC Pleat Factors.....	95
V.3.4. Comparisons among Different Reactor Types.....	98
V.4. Experimental Results of Monoliths and MFEC.....	100
V.5. Conclusions.....	101
V.6. Nomenclature.....	103

## CHAPTER VI. CFD ANALYSIS OF THE EFFECT OF FIBERS ON MASS

TRANSFER RATES IN 2D CHANNEL GEOMETRIES.....	106
VI.1. Introduction.....	106
VI.1.1. Background.....	106
VI.1.2. Overview/Approach of the Study .....	109
VI.2. Geometries Used.....	110
VI.2.1 Mass Transfer study.....	110
VI.2.1 Static Mixing study .....	112
VI.3. Design of the Study (Flow Conditions and Geometry Variations).....	113
VI.3.1. Mass Transfer Study.....	113
VI.3.2. Static Mixing Study .....	119
VI.4. Numerical Simulations .....	120

VI.4.1. Governing Equations .....	120
VI.4.2. Boundary Conditions .....	121
VI. 4. 2. 1. Mass Transfer Study .....	121
VI. 4. 2. 2. Static Mixing Study .....	123
VI.4.3. Grid Generation .....	124
VI. 4. 4. Discretization and Solution .....	126
VI. 4. 5. Iterative Convergence .....	126
VI. 4. 6. Grid Convergence .....	128
VI. 4. 7. Post-processing Calculations .....	130
VI. 5. Results.....	132
VI. 5.1. Mass Transfer Study .....	132
VI. 5.1. Static Mixing Study .....	148
VI. 6. Conclusions.....	151
VI. 7. Nomenclature.....	152

## CHAPTER VII. CONCLUSIONS AND RECOMEENDATIONS FOR FUTURE WORK .....

WORK .....	155
VII. 1. Conclusions .....	155
VII. 2. Recommendations for Future Work .....	156
VII. 2. 1. Optimization of MFEC/MFES Structures .....	156
VII. 2. 2. Reasons for Increased Flow Mal-distributions in small Particle beds .....	158
VII. 2. 3. Experiments Involving Spray Dried Spherical Particles .....	159

VII. 2. 4. Bed Voidage variations using capillary Tubes.....	159
VII. 2. 5. MFEC Ozone Converter Tests .....	160
VII. 2. 6. CFD Analysis .....	161
REFERENCES .....	162
APPENDICES .....	171
Appendix 1. Matlab Program to Simulate Hexane Breakthrough Curves .....	172
Appendix 2. Matlab Program for Reactor Comparisons for Ozone Conversion.....	174
2(a) Packed beds .....	174
2(b) Monoliths .....	175
2(c) MFEC .....	177
Appendix 3(a). FLUENT Journal File for Creating Planes in Channel Geometry.....	179
Appendix 3(b). FLUENT Journal File for Obtaining Velocity Profile for various Re...180	
Appendix 3(c). FLUENT Journal File for Running Various Re-Sc Cases in.....	183
Channel Geometry	



## LIST OF TABLES

Table 2.1	Experimental flow conditions used in hexane break through tests.....	39
Table 2.2	Properties of the MFES samples used in hexane tests.....	41
Table 2.3	Values of various parameters used in the model .....	49
Table 2.4	Properties of Pica activated carbon.....	51
Table 2.5	Experimental and predicted breakthrough times and adsorbent utilization values for packed beds of different particle sizes .....	55
Table 2.6	Comparisons of experimental and predicted breakthrough times and adsorbent utilizations .....	58
Table 2.7	Comparisons of bed properties, residence times and inverse Peclet number ( $1/Pe_L$ ) values for various for various cases shown in Fig. 2.7 .....	59
Table 3.1	Properties of the packed beds and MFES samples used in hexane tests .....	69
Table 3.2	Experimental breakthrough times and adsorbent utilization values for various bed configurations.....	70
Table 4.1	Details of sample properties used in pressure drop tests .....	72
Table 5.1	Conditions and parameters used in the model .....	79
Table 5.2	Packed bed particle diameters and bed properties used in the theoretical Comparisons .....	80
Table 5.3	Properties of various monoliths used in the theoretical comparisons.....	82
Table 5.4	MFEC cases and bed properties used in the theoretical comparisons .....	83
Table 6.1	Physical properties and operating conditions used in the preliminary mass Transfer study .....	114

Table 6.2	Matrix of various geometries used in the mass transfer study.....	118
Table 6.3	Operating and flow conditions used in static mixing study.....	119
Table 6.4	Grid convergence and discretization error analysis for open channel (Re = 100 and Sc = 0.5) .....	130
Table 6.5	Grid convergence and discretization error analysis for fiber channel (Re = 100, Sc = 0.5, ( $d_{ch}/d_f$ ) = 40, FV = 1.57% and (a/b) = 1.5) .....	130
Table 6.6	COV values for fiber and open geometries .....	151

## LIST OF FIGURES

Fig. 1.1	Micrographs of 150-250 $\mu\text{m}$ $\gamma\text{-Al}_2\text{O}_3$ entrapped in 4 & 8 $\mu\text{m}$ (1:1 ratio) stainless steel fibers - Unsintered media showing cellulose .....	4
Fig. 1.2	SEM image of activated carbon (180–250 $\mu\text{m}$ ) entrapped in 19 $\mu\text{m}$ diameter bicomponent polymer microfibers.....	5
Fig. 1.3	Packed Bed Schematic.....	10
Fig. 1.4	Schematic view of the parallel channels in a monolith substrate .....	12
Fig. 1.5	Commercial Monolith substrate with triangular channels.....	13
Fig. 1.6	Metal foam catalytic support .....	14
Fig. 1.7	Example of a wire mesh substrate assembly .....	16
Fig. 2.1	Schematic description of the experimental apparatus .....	37
Fig. 2.2	(a) N <sub>2</sub> Adsorption isotherm on carbon .....	50
Fig. 2.2	(b) Carbon pore size distribution .....	51
Fig. 2.3	Experimental equilibrium data of hexane/Pica activated carbon & the Freundlich isotherm fit at 313K.....	52
Fig. 2.4	Experimental breakthrough curves from undiluted packed beds of various particle sizes.....	54
Fig. 2.5	Model predictions of the breakthrough curves of undiluted packed beds of various particle sizes.....	55
Fig. 2.6	Experimental breakthrough curves of packed beds (PB) of various bed dilution levels and MFES beds of various bed voidages .....	56
Fig. 2.7	Model predictions of breakthrough curves of packed beds with various bed dilutions and MFES beds of various voidages.....	58

Fig. 2.8	Model predictions of breakthrough curves of packed beds (PB) of various bed dilutions and MFES#2 bed.....	
Fig. 3.1	Schematic diagram of composite bed architecture .....	68
Fig. 3.2	Breakthrough curves of composite bed and its corresponding components .....	70
Fig. 4.1	Pressure drop measurement apparatus.....	73
Fig. 4.2	Pressure drop results of microfibrinous media samples .....	75
Fig. 5.1	MFEC ozone converter design with PF = 4.0 .....	88
Fig. 5.2	Variation of $\chi$ for packed beds with particle size and velocity .....	91
Fig. 5.3	Variation of effective reaction rate constants per unit catalyst particle volume for packed beds with particle size and velocity .....	92
Fig. 5.4	Variation of inter-phase mass transport constants per unit catalyst particle volume for packed beds with particle size and velocity .....	93
Fig. 5.5	Variation of $\chi$ for monoliths with cpsi and velocity.....	94
Fig. 5.6	Variation of effective reaction rate constants per unit catalyst volume for monoliths with cpsi and velocity .....	94
Fig. 5.7	Variation of inter-phase transport constants per unit catalyst volume for monoliths with cpsi and velocity .....	95
Fig. 5.8	Variation of $\chi$ with velocity for MFEC of various PF .....	96
Fig. 5.9	Variation of effective reaction rate constants per unit catalyst volume with velocity, for MFEC of various PF .....	97
Fig. 5.10	Variation of effective reaction rate constants per unit catalyst volume for with velocity MFEC of various PF .....	97
Fig. 5.11	Variation of $\chi$ for various reactor geometries with velocity .....	98
Fig. 5.12	Experimental conversion comparisons of commercial monoliths converters with MFEC of PF=4.0.....	100
Fig. 5.13	Experimental pressure drop comparisons of commercial monoliths converters with MFEC of PF=4.0.....	101

Fig. 6.1 (a) Fixed bed of particles without fibers.....	107
Fig. 6.1 (b) Fixed bed of particles with fibers.....	108
Fig. 6.2 (a) and (b) Geometries used in the mass transfer study.....	111
Fig. 6.3 (a) and (b) Geometries used in the static mixing study .....	113
Fig. 6.4 Re and Sc ranges for various gas and liquid phase applications .....	116
Fig. 6.5 (a) Quadrilateral structured mesh (interior and boundary layer) in open geometry without fibers; (b) and (c) Triangular unstructured mesh in the interior with quadrilateral structured boundary layer on fibers and walls in fiber geometries .....	125
Fig. 6.6 Normalized residual convergence plot in open channel geometry (Re = 100 and Sc = 0.5) .....	127
Fig. 6.7 Normalized residual convergence plot in fiber channel geometry (Re = 100, Sc = 0.5, $(d_{ch}/d_f) = 40$ , FV = 1.57% and $(a/b) = 1.5$ ) .....	128
Fig. 6.8 Log reductions for H <sub>2</sub> S/H <sub>2</sub> and Hexane/Air systems for various velocities ( $d_{ch} = 400 \mu\text{m}$ , $d_f = 10 \mu\text{m}$ , FV = 1.57% and $(a/b) = 1.5$ ).....	133
Fig. 6.9 Mass transfer coefficients for H <sub>2</sub> S/H <sub>2</sub> and Hexane/Air systems for various velocities ( $d_{ch} = 400 \mu\text{m}$ , $d_f = 10 \mu\text{m}$ , FV = 1.57% and $(a/b) = 1.5$ ).....	134
Fig. 6.10 Percentage increase in MT rate for H <sub>2</sub> S/H <sub>2</sub> and Hexane/Air systems For various velocities ( $d_{ch} = 400 \mu\text{m}$ , $(d_{ch}/d_f) = 40$ , FV = 1.57% and $(a/b) = 1.5$ ) .....	135
Fig. 6.11 Velocity profiles for Re=100 in (a) open channel geometry (b) fiber channel geometry ( $(d_{ch}/d_f) = 40$ , FV = 1.57% and $(a/b) = 1.5$ ).....	136
Fig. 6.12 Velocity contours for Re=100 in (a) open channel with parabolic velocity profile (b) open channel with flat velocity profile (c) fiber channel geometry ( $(d_{ch}/d_f) = 40$ , FV = 1.57% and $(a/b) = 1.5$ ).....	137
Fig. 6.13 Concentration contours of component A for Re = 100 and Sc = 0.5 in (a) open channel with parabolic velocity profile (b) open channel with flat velocity profile (c) fiber channel geometry ( $(d_{ch}/d_f) = 40$ , FV = 1.57% and $(a/b) = 1.5$ ).....	138

Fig. 6.14	Log reduction of component A for the open and the fiber channel (( $d_{ch}/d_f$ ) = 40, FV = 1.57% and (a/b) = 1.5) geometries for various Re and Sc .....	139
Fig. 6.15	Sh for the open and the fiber channel (( $d_{ch}/d_f$ ) = 40, FV = 1.57% and (a/b) = 1.5) geometries for various Re and Sc .....	140
Fig. 6.16	Effect of fiber diameter on percentage increase in mass transfer rate due to inclusion of fibers in channel geometries (FV = 1.57% and (a/b) = 1.5) .....	141
Fig. 6.17	Effect of fiber volume loading on percentage increases in mass transfer rates due to inclusion of fibers in channel geometries ( $d_{ch} = 400 \mu\text{m}$ , ( $d_{ch}/d_f$ ) = 40 and (a/b) = 1.5) .....	143
Fig. 6.18	Effect of fiber distribution (a/b) on percentage increases in mass transfer rates with inclusion fibers in channel geometries ( $d_{ch} = 400 \mu\text{m}$ , ( $d_{ch}/d_f$ ) = 40 and FV = 1.57%).....	144
Fig. 6.19	Percentage increase in mass transfer rates in open channels with flat velocity profiles and comparisons with that in a specific fiber channel geometry ( $d_{ch}/d_f = 80$ , FV = 1.57% and a/b = 1.5) .....	145
Fig. 6.20	Percentage increases in MT rates for $\text{H}_2\text{S}/\text{H}_2$ and Hexane/Air systems for various velocities ( $d_{ch} = 400 \mu\text{m}$ , ( $d_{ch}/d_f$ ) = 40, FV = 1.57% and (a/b) = 1.5), as obtained using direct simulations and also using the results from dimensionless analysis study .....	146
Fig. 6.21	Sh versus velocity for two different gas densities in the open channel geometry with rest of the physical quantities kept constant .....	147
Fig. 6.22	Sh vs velocity for two different gas viscosities in a fiber channel geometry ( $d_{ch} = 400 \mu\text{m}$ , ( $d_{ch}/d_f$ ) = 40, FV = 1.57% and (a/b) = 1.5) with rest of the physical quantities kept constant .....	148
Fig. 6.23	Velocity profiles for simulations demonstrating the extent of mixing for an open and a fiber geometry .....	149
Fig. 6.24	Concentration profiles showing the extent of mixing for an open and a fiber geometry .....	150
Fig. 6.25	Concentration profiles in the outlet planes of fiber and open geometries .....	150
Fig. 7.1	Small tube to particle diameters can be used to achieve varying voidages .....	160

## CHAPTER I

### INTRODUCTION AND LITERATURE REVIEW

#### **I.1. Motivation:**

Heterogeneous contacting systems are at the heart of many chemical and environmental processes. The development of novel heterogeneous contacting schemes with enhanced contacting efficiency is a key step towards miniaturization and process intensification of all the heterogeneous catalytic reactors and adsorption systems. To achieve this, increasingly greater stress is being laid upon micro-structured and/or micro-engineered systems which utilize high external surface areas to provide high transport rates. Microfibrous entrapped catalysts/sorbents (MFEC/MFES), a novel microstructured carrier technology developed at Auburn University [1.1-1.4], have shown great promise in this regard. Microfibrous entrapped ZnO/Silica adsorbent has shown 2-3 fold improvement over the packed beds breakthrough times in gas phase H<sub>2</sub>S removal [1.5-1.7]. Significant improvements have been reported with use of MFEC for preferential catalytic oxidation and low temperature oxidation of carbon monoxide in hydrogen-reformate streams [1.7, 1.8]. MFEC composites using a 16% Ni/Alumina catalyst have demonstrated two to six fold higher specific activities than conventional packed bed with similar catalyst loadings for toluene hydrogenation in a trickle bed reactor [1.9]. Also microfibrous entrapped carbon based adsorbents have shown notable benefits in

terms of pressure drop and gas life in various personal and collective protection applications [1.10].

While all these experimental studies have shown great advantages with use of microfibrinous materials, the underlying reasons that bring about the enhancement in reaction rates have not been fully understood. The primary reason that has been cited was the remarkably different internal structure of these materials compared to conventional contacting systems [1.9-1.11]. But further analysis of the effects of this unique internal structure on the contacting mechanisms (flow patterns or distributions) and the resulting transport rates occurring inside these materials needs to be made. This analysis and quantification is vital for optimizing the structural dimensions i.e., particle sizes, fiber diameters, voidages, catalyst loadings, etc., of microfibrinous systems in order to realize their full benefit. Hence, it is the intent of this research to enumerate the factors that cause the enhancement in contacting efficiency in microfibrinous entrapped particulates and study the significance of each of these factors in order to model the transport rates in these materials.

Further, favorable heat transfer characteristics and ignition-extinction patterns resulting from it, were found to contribute significantly [1.8, 1.9] for enhancement in reactivity (in microfibrinous systems) in some of the cases listed above (CO oxidation, toluene hydrogenation, etc). While this is true, not all the instances listed above were influenced by heat transfer effects, and even ones which had appreciable heat transfer effects had other underlying reasons that brought about the enhancement in overall reactivity in microfibrinous entrapped catalysts/sorbents. So in this study the heat transfer



effects were purposefully circumvented with help of careful experimental design in order to recognize and study the primary causes of the higher reactivity in MFEC/MFES.

## **I.2. Analogy between Catalytic Reactors and Adsorption Systems**

All the heterogeneous contacting systems discussed in the following sections are more or less applicable to catalytic as well as adsorption applications. Between the heterogeneous catalytic reactors and the adsorption systems, the contacting systems used and the corresponding governing equations (mass, heat and momentum balances) are more or less the same. The only major difference being adsorption systems are unsteady state processes and involve a transient term in their models while catalytic processes (with negligible catalyst poisoning) are mostly steady state and do not involve the transient term. Hence in this research both the systems are studied in parallel as the analysis from one can be directly imported to the other.

## **I.3. Microfibrous Entrapped Catalysts/Sorbents (MFEC/MFEC)**

### **I.3.1. Introduction**

Figs. 1.1 and 1.2 show typical micrographs of metal and polymer microfibrous media respectively. These micro-engineered heterogeneous contacting materials are typically made of 50 to 300 $\mu$ m catalyst/sorbent particles entrapped in 2-20  $\mu$ m diameter fibers. The adsorbents or catalysts particles are held in space by 3-dimensional sinter-locked network of microfibers, resembling a “frozen-fluidized bed”. The choice of fiber material - Polymer, ceramic or metal can be made depending upon requirements of the reaction/adsorption process under consideration.

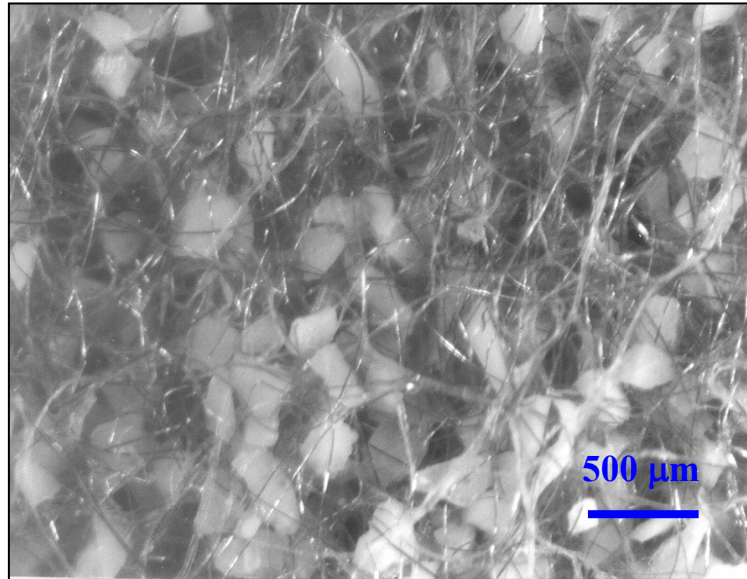


**Fig. 1.1 (a)**

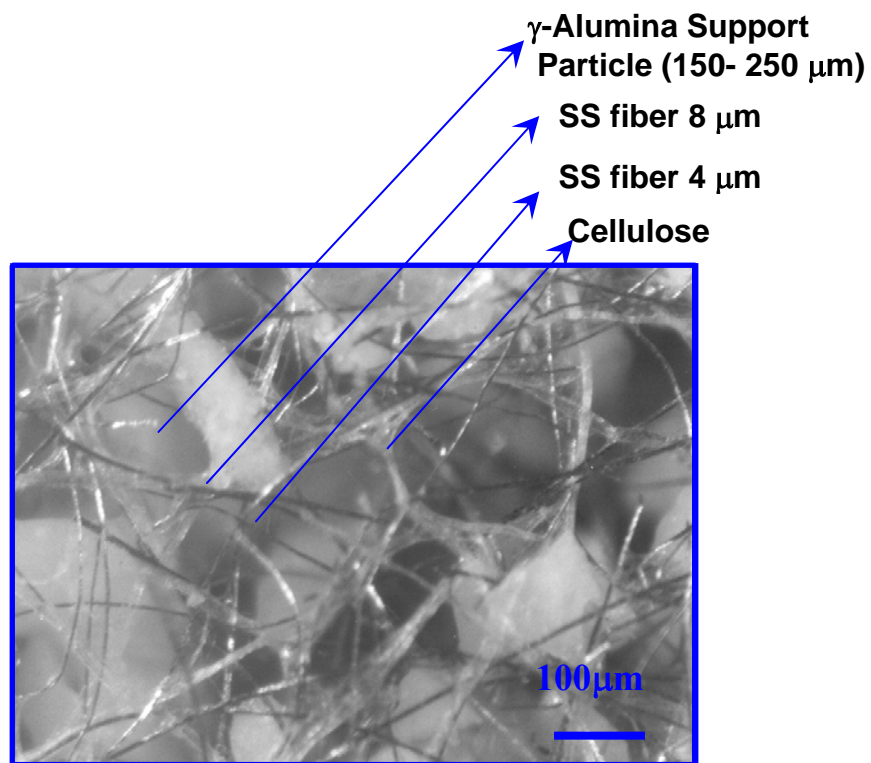


**Fig. 1.1 (b)**

**Figs. 1.1 (a) and (b) Micrographs of 150-250μm  $\gamma$ -Al<sub>2</sub>O<sub>3</sub> entrapped in 4 & 8μm (1:1 ratio) stainless steel (SS) - Unsintered media showing cellulose**

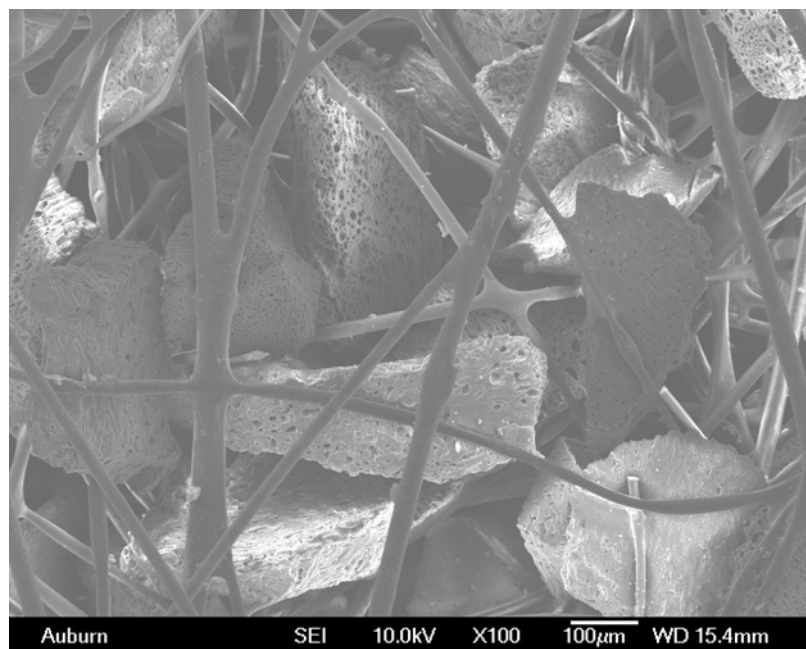


**Fig. 1.2(a)**

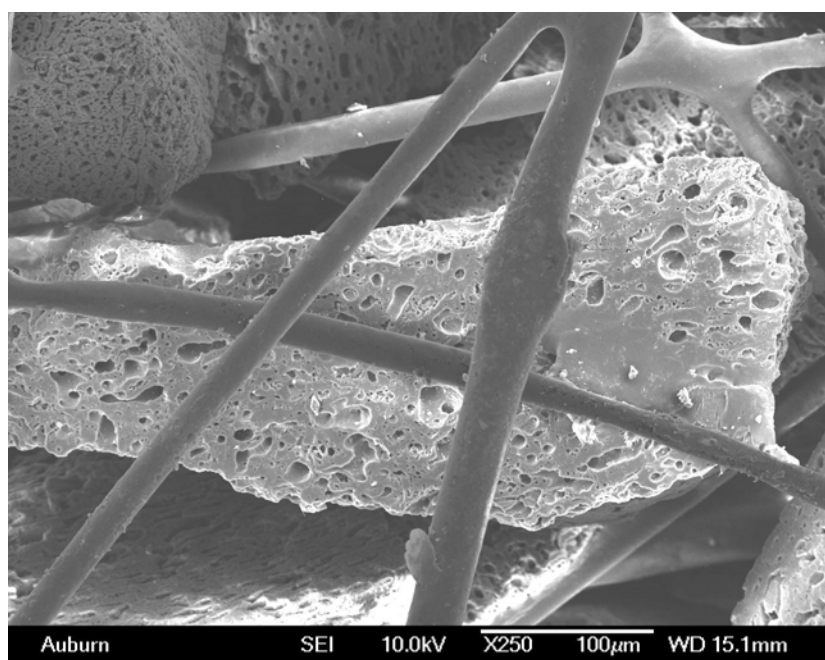


**Fig. 1.2(b)**

**Fig. 1.2(a) & (b) SEM image of activated carbon (180–250μm) entrapped in 19μm diameter bicomponent polymer microfibers**

The smaller particles used in microfibrinous systems, as opposed to larger particles (>1mm) that are typically used in the conventional packed bed systems help reduce the intra-particle and the inter-particle transport resistances significantly. Microfibrinous materials also possess other inherent beneficial properties that are a direct result of their preparation procedure. They are prepared in wet lay process, in which microfibers and catalyst particles assemble in a self-correcting highly viscous flow field (in water) to form extremely uniform structures; this uniformity eliminates “channeling” or “flow maldistributions” almost completely. As the catalyst/sorbent particulates are held by high aspect ratio fibers of secondary material, the voidages of microfibrinous sorbents can be varied from typical packed bed values all the way up to theoretical limit of 0.99; the typical voidages used are between 0.8-0.9 with about 0.01-0.03 volume fraction fibers and the rest catalyst or adsorbent. These unique properties of this material as it will be further demonstrated helps decrease axial dispersion and improve radial dispersion, create plug flow like conditions. Another exceptional benefit with these materials is the flexibility to pleat, which helps achieve higher residence times and lower pressure drops.

### **I.3.2 Method of Preparation**

The exact method of preparation of microfibrinous media varies depending on the fiber materials and diameters used. Specific methods of preparation of different types of MFECS have been discussed in detail elsewhere [1.9, 1.11 and 1.12]. A generic procedure for preparation of MFECS is described here.

The raw materials used in this process are:

1. Microfibers (metal, ceramic or polymer)

2. Catalyst support/ adsorbent particles
3. Cellulose
4. Viscosity modifiers and miscellaneous

In brief, there are four steps involved in the preparation:

1. Pre-form preparation
2. Pre-oxidation (optional)
3. Sintering
4. Catalyst impregnation (optional)

#### **I.3.2.1. Pre-form Preparation**

The first step involves a wet-lay preparation of paper-like sheets of microfibrinous media called as pre-forms. In this step, a homogeneous suspension of microfibers and cellulose is created by dispersing necessary weights of these solids in excess water using a blender. If necessary, to achieve a well dispersed mixture (suspension in water) small quantities of suitable viscosity modifiers like HEC (Hydroxy ethyl cellulose) can also be used. The resulting suspension is put into a head box of a paper making equipment. Required weights of catalyst supports and/or adsorbents are then added to the head box with simultaneously stirring of the contents and finally the excess water in the suspension is drained. The catalyst/adsorbent particles get entrapped in fiber matrix as they settle along with the cellulose and microfibers to form thin sheets of pre-forms on the bottom screen in the wet-lay equipment. These pre-forms are carefully removed and dried at temperatures of 40-100 C to get rid of the water. In the dried sheets cellulose acts as binder to hold the entire structure together.

#### **I.3.2.2. Pre-oxidation**

This step is optional. The dried pre-forms are cut to required sizes, layered, as required and then oxidized in air diluted with  $N_2$  at about 300C. The purpose of this step is to eliminate cellulose and the associated carbon from the samples. The structure of the perform sheets thus rid of cellulose is extremely weak and needs extreme care while handling.

#### **I.3.2.3. Sintering**

The pre-oxidized sheets or sheets directly obtained in step 1 are sintered at suitable temperature depending on the fiber material. Sintering of metal microfibers is done in hydrogen atmospheres at about 900-1000 C, while ceramic and polymer fibers are sintered in air at 700-1000C and 150-200 C respectively. During this process the fibers bond with each other to form a robust matrix. BET surface areas and pore volumes of several common catalyst supports like  $\gamma$ -alumina and silica gel, were relatively unaffected by the high temperature and/or Hydrogen treatment involved in sintering [1.9]. Hence the overall process of preparation of MFECS doesn't cause any significant degradation of most of the catalyst supports or adsorbents.

#### **I.3.2.4. Catalyst/Active Material Impregnation**

This step is needed only in applications requiring dispersion of the any active material on the high surface area support particles entrapped in the fiber matrices. The catalysts/active materials can be impregnated by conventional methods like incipient

wetness technique, followed by calcination in air at required temperature. Details of pseudo-incipient wetness technique, a variation of the incipient wetness method which is mostly used with MFECS, are discussed elsewhere [1.9].

#### **I.4 Heterogeneous Contacting Systems in Use**

Heterogeneous catalytic reactors and adsorption systems are commonplace in many chemical processing and separation applications. Although heterogeneous contacting systems have been in use and researched for quite a long time, there is still a lot of scope for improving their efficiency. Also as they have widespread applications in industry, improvements in their design, however small, can help realize major benefits. This section gives a brief review of various heterogeneous contacting systems in use in the industry, while the important criteria in choosing a system and major factors affecting the performance of the contacting systems are discussed in the sections following this.

Currently the various configurations being used for heterogeneous contacting include: packed beds, fluidized beds, moving bed reactors, structured configurations like monoliths, wire-meshes, catalytic foams, etc. Each of these configurations has specific advantages and disadvantages. While fluidized beds and packed beds use extruded or sized particles, monoliths, foams and wire- mesh reactors employ catalysts in the form of wall-coatings. These systems can be broadly classified into fixed beds and moving beds. Some of the major contacting systems of interest are discussed in this section. All the systems that are discussed in here except fluidized beds are fixed bed configurations. While there exist other variants of moving bed (recirculating bed, moving-packed bed

etc.) to keep things concise, only fluidized beds will be discussed here. More information on the other kinds of reactors can be found elsewhere [1.13,1.14].

#### **I.4.1 Packed Beds**

Packed beds are the most conventional and basic forms of heterogeneous contacting systems widely used in the industry. They consist of structured or unstructured packing or particles (of any size and shape) placed in the form of a bed inside a reactor tube. Typically particles ranging from a couple of mm in diameter to a centimeter are used in industrial reactors and adsorption columns. As packed beds are the earliest form of heterogeneous contacting, a lot of information about them has been published [1.13, 1.14] and the basics about packed bed behavior are well understood. A schematic of a packed bed reactor is shown in Fig. 1.3.

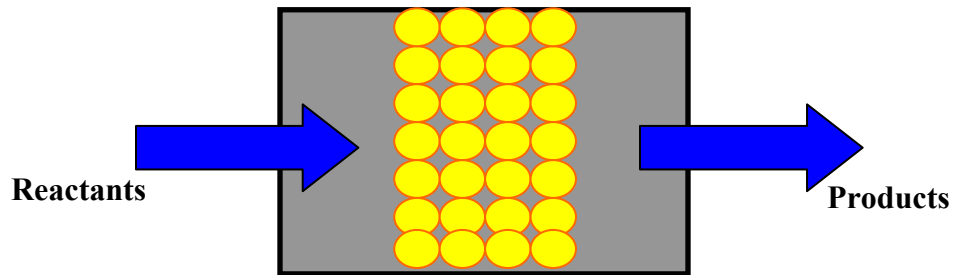


**Fig. 1.3 Packed Bed Schematic**

Although their construction is simple, they suffer from some serious setbacks like wall and intra-bed channeling, flow maldistributions, and axial diffusion. If not for these non idealities which are oftentimes significant, packed beds can be said to have plug flow conditions. Although small particle packed beds provide high intra and inter particle transport rates, there is a tendency for elutriation and plugging [1.13] and pressure drops



are high. In processes involving large heat effects effective temperature control of large packed beds can be difficult as they have poor thermal conductivity; this causes undesired temperature gradients. Also the packed beds are not well suited for applications involving frequent regeneration and the units may be difficult to service. Furthermore the particles in a tightly packed bed tend to relocate and settle when subject to external motion or vibrations, creating dead or un-occupied void volumes which further result in significant differences in bed distribution. All these factors make packed beds a less efficient method of contacting and also less suitable for mobile applications.

#### **I.4.2 Monolith Substrates**

While packed beds and fluidized beds are the traditional heterogeneous contacting systems, in the last three decades or so monolith substrates and foams have gained significance in automotive and stationary environmental pollution control applications [1.15, 1.16]. Details about the manufacturing process and industrial applications of monoliths can be found elsewhere [1.15, 1.17, 1.52]. Monoliths can consist of triangular, square, hexagonal or other regular-shaped channels (mostly parallel to the flow direction) coated with thin layers of catalyst/catalyst support on the channel walls. The basic channel or honeycomb unitary structures are made from extruded ceramic or corrugated metal sheets. The ceramic substrates are mostly made of cordierite. The monolith manufacturing process involves wash coating a slurry catalyst support and a binder on the channel walls of honeycomb structures followed by drying at high temperature. The catalysts are then impregnated into the high surface area support by standard impregnation techniques. The thickness of the wash-coat, number of cells per square inch

(cpsi) and wall-thickness can be varied according to the specific requirements of a given application. Fig. 1.4 shows a schematic of monolith substrate and Fig. 1.5 shows a 400 cpsi commercial monolithic ozone converter for plasma generation units.

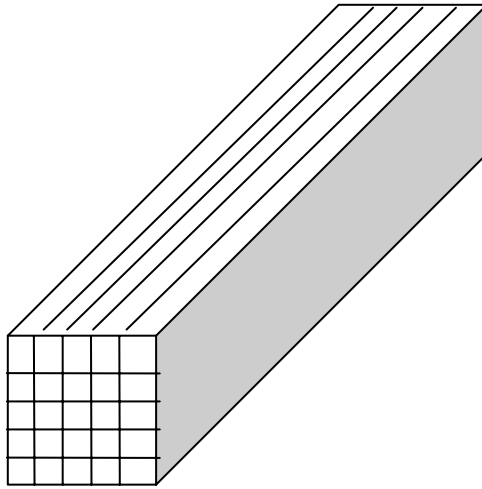


Fig. 1.4 Schematic view of the parallel channels in a monolith substrate

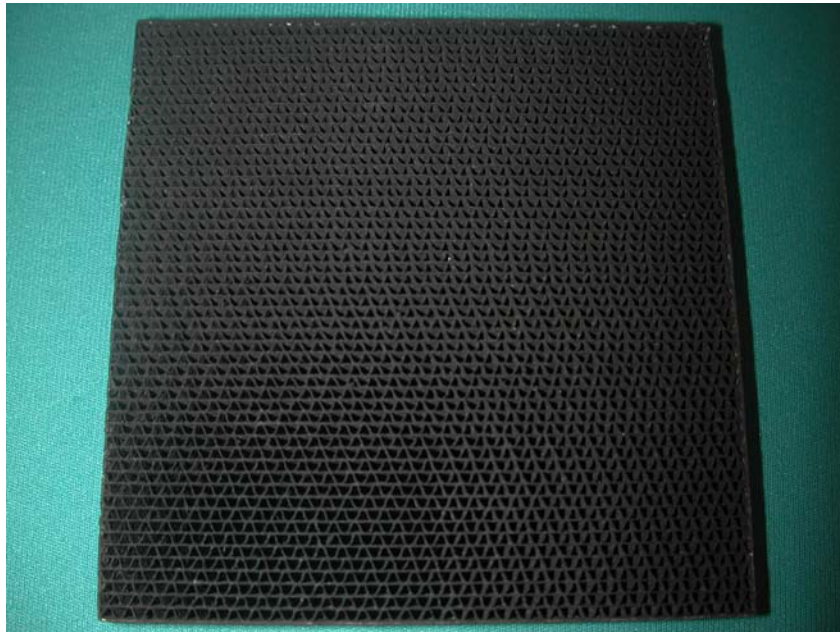


Fig. 1.5 Commercial Monolith substrate with triangular channels

Comprehensive reviews of the applicability of monoliths, their advantages and disadvantages have been reported elsewhere [1.18-1.19,1.50]. The major advantage with monolith substrates is the significantly lower pressure drop or flow resistance they offer compared to other forms of contacting. But monolithic catalyst substrates are mostly constrained by inter-phase mass and heat transport resistances, low intra-bed heat transfer and suppressed radial mixing limitations. The limited inter-phase transport rates are due to the well developed laminar flows occurring in the parallel straight channels of monoliths while radial mixing is constrained by impermeable channel walls. The above limitations are partly resolved using multiple short monoliths in series with intermediate mixing of flow streams from the flow channels. Also, metal corrugated structures which have thinner wall thicknesses and better heat transfer properties are being becoming increasingly popular. The accumulation of wash-coat near the wall-corners, which is almost inevitable in practice, is a serious concern in any monolith manufacturing process as it makes the catalyst layer thickness non-uniform. In spite of their high performance and robust structures, the above limitations along with high initial costs restrict the wide spread usage of monoliths.

#### **I.4.3 Catalytic Foams**

Catalytic foams are another form of multi-phase contacting which have gained significance in the late twentieth century. They consist of high voidage porous ceramic or metallic reticulated foams, washcoated with catalyst support of required thickness. Impregnation of metal/ metal oxide catalyst is done over the washcoated support. The major advantage of catalytic foams over parallel channel monoliths is the high

interconnectivity of the pore structure, which promotes proper radial mixing. Fig. 1.6 shows a metal-foam before washcoating. Catalytic foam structures are being used in some air-purification and filtration applications like the monolith substrates [1.20, 1.21]. Richardson et al [1.21-1.23] have published correlations for pressure drops and mass and heat transfer rates in catalytic foams.

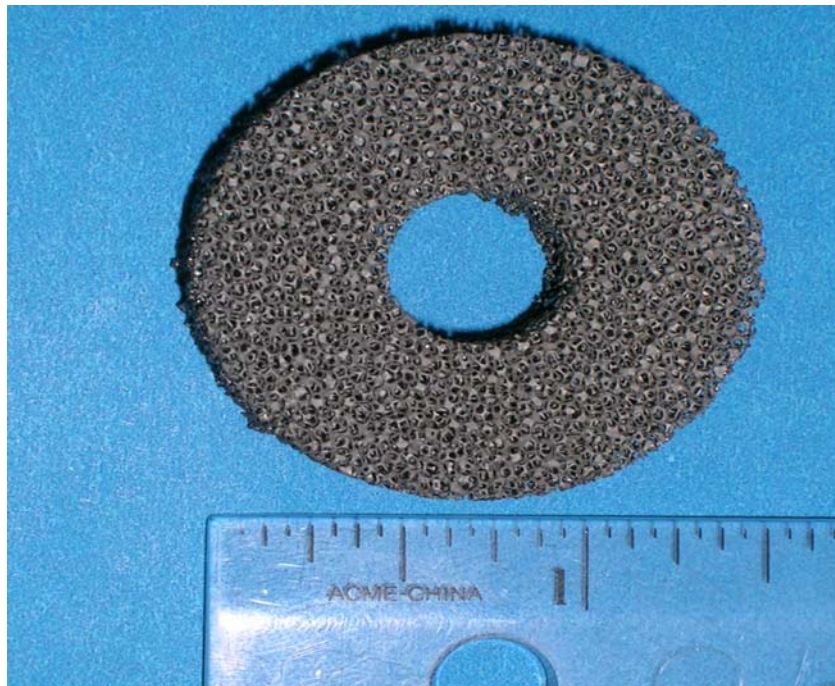


**Fig. 1.6 Metal foam catalytic support**

#### **I.4.4 Micro-Channel Reactors**

In the last decade or so, micro-channel reactor development has escalated, owing to their excellent transport rates and temperature control [1.24-1.27]. With micro-fabrication techniques becoming more commonplace micro-channel reactors are gaining significance. They can be made from various materials: stainless steel [1.28], glass

[1.29], silicon [1.30] and polymer [1.30]. These reactors enable high throughput catalyst screening, micro-sensors and lab-on-chip concepts. The washcoating and impregnation process in these reactors is more or less similar to the monolith reactors. While these reactors are best suited for high-end applications their initial costs prohibit their usage for day-to-day applications.

#### **I.4.5 Wire Mesh Screens**

The wire-mesh honeycomb is a relatively new concept; a wire-mesh module is constructed from alternating sheets of corrugated and flat wire mesh screens [1.31]. Other designs include regularly spaced flat metal screens stacked in series. The wire surface of each mesh is pre-coated with high surface area particles to form a certain thickness of porous-sintered layer. The precious metals or the metal oxide catalysts are impregnated onto this high surface area support. This kind of design permits free radial flow because the channel walls have hole-openings of wire mesh. The wires also provide for direct electrical heating when required. Also, the accumulation of wash-coat is reported to be greatly minimized. While this concept has good potential, it is still being researched and hasn't evolved into a full-scale commercial product. Fig. 1.7 shows a wire-mesh type of reactor.

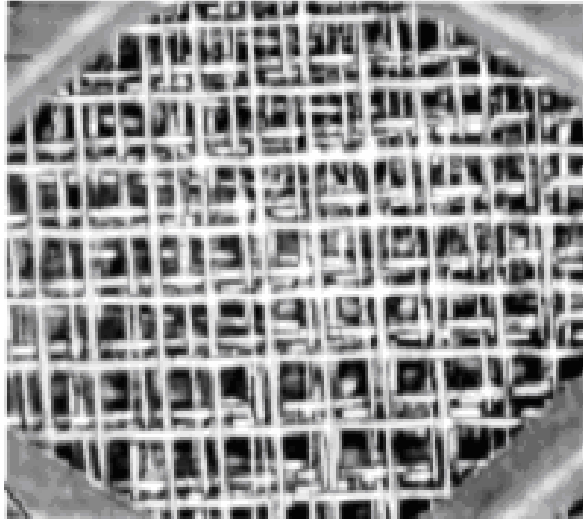


Fig. 1.7. Example of a wire mesh substrate assembly  
(From: [www.precision-combustion.com](http://www.precision-combustion.com))

#### **I.4.6 Fluidized beds**

Fluidized beds are one of the major forms of moving bed configurations. There exists vast literature on mass and heat transports and dispersion coefficients on these reactors. Kunni and Levenspiel [1.32] present a comprehensive account on this subject. These reactors consist of fluidized catalyst particles suspended in the moving gas/liquid reactant stream. The major advantage with this configuration is the elimination of hot-spots and reaction runaways which cause meltdowns and even explosions. The rapid-mixing of solids allows for excellent temperature control; as solid particles (the major heat sink) are in the fluidized phase the effective thermal conductivity of the bed is greatly increased compared to the fixed beds. These reactors can also use smaller particles which reduce transport resistances. Also regeneration of catalysts in these reactors is easy as the catalyst in the fluidized form can be pumped from one unit to another.

But the flow patterns in the fluidized beds are extremely complex and are completely understood. There exists considerable amount of by-passing and back mixing and the flow is far from plug-flow conditions, which makes for really inefficient contacting. Also as the velocities maintained are always higher than the minimum fluidization velocity, the pressure drops can be high.

### **I.5 Major Criteria in Reactor Design**

Some of the major criteria in designing any reaction system for a given application are to:

- Decrease pressure drop
- Increase conversion
- Increase selectivity
- Increase catalyst/ sorbent life
- Decrease weight of catalyst or sorbent needed
- Decrease weight and volume of the reactor

### **I.6 Factors Affecting Reactor/Adsorption System Performance**

In a heterogeneous process, the reactants/adsorbates are generally in gas or liquid phase and the catalyst/adsorbent is in solid phase. Unlike other separation processes, this allows for separation of catalyst/adsorbents and reactants/adsorbates very easily. This is a significant and economically attractive aspect of heterogeneous systems. In most of the applications catalysts/adsorbents are highly valuable and their recovery is mandatory. But as the reaction/adsorption occurs at the fluid-solid interface there are additional steps

involved in the process that can hinder the reaction rates. In any heterogeneous process, the reaction occurs by a sequence of elementary steps that includes diffusion of reactants to the particle surface, diffusion in the pores, adsorption of reactants on to the catalytic sites, surface reaction, desorption of products and diffusion of products back into the flow stream. Hence the corresponding rates of occurrence of each of the above said steps contribute to the overall reaction rates.

All the design criteria mentioned in section 1.5 depend largely on the surface reaction rates as well as the mass, heat and momentum transfer rates inside a catalytic reactor. For a given catalyst loading or kind of adsorbent used the surface reaction or adsorption rates are constant for any type of reactor. But the choice of the contacting system/geometry remarkably influences the pressure drop, intra-particle and inter-phase (heat and mass) transport rates, axial diffusion and flow mal-distributions, and hence can affect the conversion, the selectivity, the amount of catalyst needed and the operating costs of the process.

A lot of literature exists about the external and internal mass transfer and surface reactions and the models used for their rates. Although they are critical steps in any fluid-solid contacting process including the cases pertaining to the present study, as they are well discussed in the literature, the discussion about them will be kept short. The focus here will be laid on other factors which are of interest to the present research.

### **1.6.1 Surface Reaction Rate**

The surface reaction for any catalytic reaction consists of multiple steps – adsorption of reactants, reactions of adsorbed species with other adsorbed or gas phase



species and desorption of products. Any of the above steps could be rate determining. The surface reaction rates generally follow an Arrhenius rate law. The surface reaction rates could be of any order depending on the exact mechanism and reactant compositions. More information about can be found elsewhere [1.13, 1.14].

### **1.6.2 Intraparticle Mass Transfer Rate**

In most of the fluid-solid reaction catalytic reaction systems catalyst is dispersed on a high surface area porous material. So the reactants need to diffuse into the particles and products need to diffuse out of the particles. Also in the adsorption processes the adsorbate molecules need to diffuse into the adsorbent pores. This additional step can become rate limiting and needs to be accounted for in the adsorbent or catalyst bed rate calculations. The intraparticle transport resistances are modeled using effectiveness factors and effective factor estimation for various types of geometries are explained elsewhere [1.13].

### **1.6.3 Fluid-Solid Interphase Mass Transfer Rate**

In any fluid-solid contacting process the gas phase diffusion of chemical species to the solid surface and back into the bulk fluid phase are key steps and often times can become rate limiting. There are various correlations available in the literature for estimation of fluid phase mass transfer correlations for various system geometries,  $Re$  and  $Sc$  ranges. Detailed reviews about the mass transfer correlations in packed beds [1.33] and monoliths [1.34,1.35] are given elsewhere.

For the particle sizes typically used in MFES, the  $Re$  are less than one for most of the gas phase applications. While there exist many semi-empirical correlations which can estimate the Sherwood numbers/mass transfer rates in packed beds at higher  $Re$  ( $>10$ ) with reasonable accuracy, most of the existent correlations or theoretical equations predict the values which are off by up to four orders of magnitude [1.36-1.39] for lower  $Re$ . Also, the  $Sh$  in low  $Re$  were far below the theoretical limit of  $Sh = 2.0$  expected based on the  $Sh$  calculations for a sphere placed in an infinitely stationary fluid medium. Various reasons have been cited for the observed mass transfer rates to be far below the theoretically expected values. It has been widely reported that in small particle packed beds negative effects of channeling and axial diffusion can create large deviations from plug-flow models. Hence, the resulting fluid-solid mass and heat transfer rates are far below the expected values.

In practice the fluid phase effective mass transfer rates are inseparable from the effects of axial dispersion, but conventional chemical reaction engineering models have mostly excluded these effects from fluid phase mass transfer coefficients. To avoid any ambiguity, the term “interphase mass transfer” in the discussion henceforth, represents only the mass transfer across the fluid film (on the particle) and does not include any of the deviations encountered from plug flow conditions due to axial dispersion effects discussed above. The overall process is then modeled as a plug flow case combined with appropriate effective axial dispersion coefficients.

#### **I.6.4 Deviations from Plug Flow**

Following are the factors that can cause axial dispersion in fixed beds:

- (a) Axial molecular diffusion (fluid and solid phase).
- (b) Interstitial velocity variations due to formation of (parabolic) velocity profiles.
- (c) Eddy diffusion (caused by turbulence) in axial direction.
- (d) Channeling near the tube wall due to the associated bed voidage variation.
- (e) Intrabed channeling or flow maldistributions due to particle clustering or non-uniformity in bed packing.

The significance of each of the above depends on the various factors like particle sizes, bed to particle diameter ratios,  $Re$ ,  $Sc$ , etc., associated with any process. These factors will be briefly reviewed here and some of these will be explored in detail in various chapters in this dissertation.

##### **I.6.4.1 Axial Molecular Diffusion**

Axial molecular diffusion is the most common factor that can cause deviations from plug flow and it has been widely studied. It has been known for a long time that in the low  $Re$  regime, molecular diffusion in the axial direction can greatly lower the concentration potentials and hence slow down the reaction rates. Levenspeil [1.13] has given a detailed account of various gas and liquid phase dispersion coefficients and comparisons of real and plug flow reactors for various kinetics.

While gas phase axial diffusion has been widely studied some other studies have highlighted the presence of axial molecular diffusion in the solid phase. Suzuki and Smith

suggested that the effect of diffusion through the porous particles had to be included in the axial dispersion correlations for packed beds. On a similar note, Wakao et al [1.37] suggested that the axial dispersion coefficients calculated for inert particles (molecular diffusion in gases) can not be applied to reactive conditions. According to these authors the concentration profiles inside the particles were not center symmetric for the applications involving fast surface reaction rates and low Re and the diffusion of chemical species through the solid phase can not be neglected. They developed modified axial dispersion correlations to account for both solid phase and gas phase diffusion based on first order kinetics. They also corrected many prior results by including this effect [1.42]. Many other studies [1.41, 1.45 and 1.54] also have noted the significance of axial diffusion in low Re flows.

But many studies found the estimation of axial dispersion coefficients based on the molecular diffusion alone in gases to be insufficient to explain the discrepancy in mass transfer coefficients at low Re [1.37, 1.41].

#### **1.6.4.2 Interstitial Velocity Variations due to Formation of (Parabolic) Velocity Profiles**

Taylor and Aris [1.55] were among the first to suggest that the formation of parabolic velocity profiles in tubular reactors can cause axial dispersion. They have derived the exact equations for predicting axial dispersion coefficients in plain tubular reactors (without packing). Lewnspiel [1.13] and Fogler [1.14] provide a detailed account of this derivation. Basing on these Edwards and Richardson developed an improved axial dispersion correlation for packed bed reactors. This is one of the earliest and most widely

used axial dispersion correlation available in literature [1.44, 1.53], and it accounts for molecular diffusion and velocity variations (solid-phase diffusion is not included). The influence of the interstitial velocity variations on the mass transfer rates in microstructured geometries is studied in detail in chapter VI.

#### **I.6.4.3 Eddy diffusion (or turbulence) in axial direction**

Eddy diffusion like molecular diffusion can contribute to axial dispersion. Eddy diffusion can become prominent at high Re where turbulence occurs in the flow. Plots of dispersion coefficients in turbulent regimes in pipes are shown elsewhere [1.13]. However, as the Reynolds numbers for flow conditions used in MFECS are low ( $Re < 100$ ), there is no turbulence, i.e., there is no mixing caused by eddies and hence the mass transfer to the solid surface and dispersion are not influenced by this factor.

#### **I.6.4.4 Wall Channeling**

Some other studies have attributed the low Sh values in low Re regime to “wall-channeling,” which can become significant in reactors and adsorbent columns with low bed-to-particle diameter ratios [1.38, 1.47-1.49]. It has been shown in these studies that the voidage of packed beds varies in a sinusoidal fashion near the reactor walls and gradually becomes uniform towards the center of the bed. This variation in the voidage causes flow maldistributions. A ratio of reactor-to-particle-diameter greater than 10:1 has been recommended by Klerk [1.48] to avoid fluid channeling near the wall. In this work reactor-to-particle-diameter ratios greater than 10 were used to overcome this effect.

Also, Rexwinkel *et al.* [1.46] corrected many experimental results present in the literature for the effect of wall channeling and axial molecular diffusion and found that these factors could not completely explain the observed deviations in Sh. They suggested that the discrepancy in mass transfer coefficients at low Re can also arise due to “wrong interpretation” of experimental data in high dilution beds and attributed it to the presence of large differences between the local concentration experienced by the particle and the mixed cup concentration of the whole bed cross-section.

#### **1.6.4.5 Intra-bed Channeling or Flow Maldistributions**

Apart from the axial molecular diffusion, eddy diffusion and wall channeling, the other significant aspect in small particle diameter beds is the flow maldistribution. Langer *et al* [1.43] made a comprehensive review of Sherwood numbers at low Reynolds number flows; they observed that axial dispersion effects in shallow and/or small diameter particle beds can be unpredictable and the effective axial dispersion coefficients ( $d_p < 3.0\text{mm}$ ) can be much higher than that expected based on molecular diffusion alone. They proposed that this discrepancy is a consequence of the increasing tendency of smaller particle beds towards “cluster” formation, which leads to intra-bed channeling or flow maldistributions; they also noted that the extent of the particle clustering and hence the dispersion coefficients increased with a decrease in the particle size. This undesirable effect resulted in a substantial drop in the catalyst or adsorbent performance.

To account for this effect, they proposed a particle diameter dependent correlation for Peclet number as well as the radial dispersion factor in axial dispersion correlations originally proposed by Edwards and Richardson. These corrections are widely used by

many authors [1.44]. While the exact reasons for the increase in tendency for cluster formation is not clear, the theory and the resulting semi-empirical equations proposed by Langer et al agreed well with the experimental results obtained from many studies. Other studies further confirmed the presence of flow maldistributions and their significance [1.45, 1.46 and 1.50]. Tsotasas [1.45] also found the non-uniformities in beds of fine-grained particles to be significant and wall channeling and interparticle velocity variations to be insignificant in packed beds. Edwards and Richardson [1.53] also pointed to the possible effect of intrabed channeling in small particle beds. These effects are studied in detail in chapter II.

#### **1.6.5 Heat Transfer**

If present, temperature differences in the bed could become another major factor influencing the reactor or adsorbent bed performance. The temperature differences could occur when exothermic or endothermic reactions are involved or when external heating/cooling is required to alter the reaction kinetics. The exothermic conditions can lead to hot spots and can also lead to multiple steady states. The theory of non linear dynamics arising from heat transfer effects and non linear kinetics has been the focus of many studies, the details about these can be found elsewhere [1.14, 1.40]. In this study, these effects were circumvented with help of careful experimental designs. This was purposefully done to isolate the effects of other factors affecting the reaction rates in MFECS.

## **I.7. Catalyst/Adsorbent Characterization Techniques**

Catalyst/Adsorbent characterization involves measurement of critical parameters and properties. This is an essential part of catalyst/adsorbent development. Characterization allows for proper assessment and improvement of catalyst/ adsorbent performance. A wide range of techniques are available for characterization of catalyst/adsorbent properties and measuring activities. Not all the techniques are useful for a given application. Depending on the objectives of the experiment and the capabilities and limitations of the technique, a proper selection of technique needs to be made. A detailed account of various catalyst characterization techniques is given elsewhere [1.56]. In this section a brief overview of a few characterization techniques which were used in this study are discussed.

### **I.7.1 Particle Size Characterization**

Determination of particle size distribution of powders is a critical step in almost all particular solids processing techniques. The particle size of a catalyst/ adsorbent particles dictates the intraparticle and fluid-particle interphase transport rates. Particle size distributions can be analyzed by various techniques like sieving, gravitational sedimentation, microscopy based techniques and laser light diffraction, etc. A detailed account of these particle size characterization techniques is given elsewhere [ ]. In this work sieving was the only method used.

Although sieving is one of the oldest powder classification techniques it is among the most widely used, simplest and least expensive techniques for determination of particle size distribution over a broad size range of particles. The method, consists of



shaking (agitating) the powder sample through a set of standardised sieves stacked in series in decreasing order of the mesh sizes. Size of a particle fraction is reported in terms of the mesh sizes between which it is retained or an average particle size of the sieves can be used.

### **I.7.2 Surface Area Measurements**

Total surface area of a support/adsorbent is one of the most important particle parameters. For a catalyst or sorbent (chemisorption) support it determines the area available for dispersion of impregnated species and for an adsorbent in physisorption process it provides more area for adsorption of adsorbate molecules. The measurement of surface area involves principles of physical adsorption. The method of measuring total surface area of a catalyst involves principles of physical adsorption/desorption of a particular molecular species on the surface of the high surface area material. If the conditions under which a complete adsorbed layer averaging one molecular layer thick can be established and the area covered per molecule is known, then the quantity of the adsorbed material gives directly the total surface area of the sample. The most common method of measuring surface area, and used very routinely in catalyst studies is that developed by Brunauer, Emmett and Teller (BET) in 1938. A Quantachrome BET surface area measurement was used in this study for measuring total surface areas of high surface area supports and adsorbents.

### **I.7.3. Pore Size Distribution**

Pore Volume Distributions can be determined by either gas adsorption porosimetry (typically N<sub>2</sub>, Ar or CO<sub>2</sub>) or mercury intrusion porosimetry. Gas porosimetry measures pores from 17 Angstroms to about 4000 Angstroms in diameter, where as Mercury porosimetry is applicable to pores from 0.006  $\mu\text{m}$  up to 900  $\mu\text{m}$  in diameter. Gas adsorption will measure pore size by recording isotherms from low pressures to saturation pressure. The pressure range is determined by the size range of the pores to be measured. Isotherms of microporous materials are measured over a pressure range of approximately 0.00001 mmHg to 0.1 mmHg. Isotherms of mesoporous materials are typically measured over a pressure range of 1 mmHg to approximately 760 mmHg. Once details of the isotherm curve are accurately expressed as a series of pressure vs. quantity adsorbed data pairs, a number of different theories or models can be applied to determine the pore size distribution. Available micropore methods include: Density Functional Theory (DFT), MP-Method, Dubinin Plots (Dubinin-Radushkevich D-R, Dubinin-Astakov D-A), and Horvath-Kawazoe (H-K) calculations. Available Mesopore methods include: Barrett, Joyner and Halenda method (BJH), and Density Functional Theory (DFT).

Mercury intrusion porosimetry involves placing the sample in a penetrometer, then surrounding the sample with mercury. Mercury is a non-wetting liquid to most materials and resists entering voids, doing so only when pressure is applied. The pressure at which mercury enters a pore is inversely proportional to the size of the opening to the void. As mercury is forced to enter pores within the sample material, the change is measured in capacitance of capillary of the penetrometer, this capacitance is proportional

to the intrusion volume. This intrusion volume is recorded with the corresponding pressure or pore size. In this study only gas sorption techniques were used.

#### **I.7.4. Scanning Electron Microscopy**

In a typical SEM, electrons are thermionically emitted from a tungsten or lanthanum hexaboride ( $\text{LaB}_6$ ) cathode and are accelerated towards an anode; alternatively, electrons can be emitted via field emission (FE). The electron beam, which typically has an energy ranging from a few hundred eV to 100 keV, is focused by one or two condenser lenses into a beam with a very fine focal spot sized 0.4 nm to 5 nm. The energy exchange between the electron beam and the sample results in the emission of electrons and electromagnetic radiation, which can be detected to produce images of matter.

The samples containing non-metal fibers obtained for this work were pre-coated with carbon using SPI module carbon coater to avoid charge building inside the sample while performing SEM. The SEM images of microfibrinous materials were obtained using a JEOL JSM 840 (20 kV) SEM. The SEM images were recorded at magnification levels of 37 and 200 using an in-built digital camera.

#### **I.8. Computational Fluid Dynamics (CFD)**

Computational fluid dynamics (CFD) mainly deals with the numerical solution of the mass and momentum (Navier-Stokes) equations for problems involving fluid flow [1.57-159]. If required heat and/or species mass conservation equations can also be integrated into the CFD algorithms to find solutions for problems involving heat

transport, mass transport and/or reactions. The solution computed using CFD provides values of flow variables such as velocity, pressure, temperature, density, concentration, etc. at a large number of locations within the domain.

Many typical chemical processes involve reactions, heat generation, mass transfer and heat transfer in process flows. The fluid flows in most of the chemical process units are very complex and difficult to measure, and often times heat and mass transport occurs between multiple phases. Trouble-shooting as well as improvements in process efficiency requires solution to dependent variables at multiple data points in the fluid flow field and time, which are often unavailable. Given these experimental difficulties, computational fluid dynamics (CFD) methods can prove to be powerful design and analysis tools for chemical engineering applications. It can be applied to examine the influence of various parameters on flow behavior in different equipment designs, or to compare performance of a given design under different operating conditions. It conveniently allows for examining various concepts in a virtual setting, without actually building a physical model. Scale up related issues can also be easily eliminated as process equipment at its full-scale can be analyzed using CFD.

CFD has its origins mainly in the aerospace industry, as a design tool to model the complex flows around moving objects [1.57]. However, the usage of present day CFD tools has spread into almost every application involving fluid flow. CFD is increasingly being used to model heat and mass transport in many chemical processes like combustion, mixing, catalytic reactions, etc. [1.60–1.75]. A few studies which exemplify these applications are cited here. Calis et al. [1.60] have demonstrated the use of CFD to successfully estimate the pressure drops in novel structured packed beds. In a recent

study by Nijemeisland et al. [1.61], CFD was used for determining the optimal design of catalyst for steam reforming application. CFD simulations of chemically reactive flows in internal combustion engines [1.64, 1.65], catalytic combustion processes [1.66, 1.67] and flue gas treatment have also been reported [1.68]. Dynamic and static mixing equipment are at the heart of most chemical processing plants and many recent efforts have successfully used CFD to model these processes [1.72-1.76]. In this work, CFD is used to analyze the effect of inert fibers present in MFECS on the fluid-particle mass transfer rates (chapter VI).

### **1.8.1. Discretization Methods**

CFD involves discretization of partial differential equations and solving them numerically. It is mainly applied to problems where it is difficult to find an exact solution to the partial differential equations describing the problem. The exact solution may be difficult due to many reasons - physical complexity, nonlinearity, geometric complexity, etc. The various methods of discretization and solution of numerical equations used in CFD are described in detail elsewhere [1.57-1.59, 1.77-1.80]. A brief review of some of the methods used in this work is presented in this section. The three main approaches used for discretization are:

- Finite Difference Method (FDM)
- Finite Volume Method (FVM)
- Finite Element Method (FEM)

In FDM, the governing equations are discretized only at selected points in the domain [1.57, 1.59]. These points are called nodes and the solution is obtained only at

these points, the solution between the nodes is interpolated by simply connecting the nodes with straight lines. FDM is widely employed in CFD studies. In this method, Taylor series expansions are used to develop finite difference expressions for the various partial derivatives and depending on the required level of accuracy the corresponding higher order terms in the Taylor series expansions are neglected. These discretized finite difference equations are solved using any of the various implicit or explicit methods to obtain solution at various locations in the domain called nodes. FDM unlike the other two methods uses the differential form of governing equations.

In FVM, the governing equations are discretized and solved at selected regions in the domain called as volumes [1.77]. "Finite volume" refers to the small volumes surrounding each node point on a mesh. The distributions of each of the flow variables inside the control volumes can be constant, linear or higher order variations. This method uses the integral form of the conservation equations. In this method, the divergence theorem is employed to convert volume integrals in the partial differential equations that contain a divergence term to surface integrals. This method unlike the FDM does not require structured grids for its solution. It is widely used in many computational fluid dynamics packages.

FDM was used to model hexane breakthrough curves in chapter III in this work. The model used for this was a 1-dimensional transient system involving the solution of only species and mass conservation equations. This is not a CFD simulation in the strict sense as it did not involve solving the momentum balance equations. The commercial CFD software Fluent 6.3 is used in this work (Chapter VI) employs FVM. FEM is not used anywhere in this research.

### **I.8.2. Limitations of CFD**

CFD like any other technique has certain limitations. One of the primary limitations of CFD is that it can not reproduce the physical effects not included in the model. Also, representing some of the exact physics of the real world flows with precision can become computationally expensive. Possible examples [1.80] of this include, the difficulty with direct numerical simulation of the turbulent flows, modeling multiphase flows and solution of reactive flows with multiple reactions running in series and parallel. The difficulty with turbulent fluid motion is that it requires a spatial grid fine enough to capture the smallest length scales throughout the domain. This requires extensive computational resources even for the processes involving slightest complexity. This is overcome in most commercial software by using time averaged equations and modeling the resulting turbulent correlation terms. This and a variety of other turbulence models are also available but they can lead to significant inaccuracies under certain circumstances and the user needs to be cautious in applying them.

Further, the results obtained using CFD cannot be trusted without proper verification and error estimations. A detailed account of the convergence, code verification and error estimation is present elsewhere [1.57-1.59, 1.81] and a brief summary is given in chapter VI.

## **CHAPTER II**

### **HEXANE BREAKTHROUGH TESTS ON MFES AND PACKED BEDS**

#### **II.1. Introduction**

In this study hexane adsorption breakthrough curves from activated carbon beds were used to understand the significance of various factors influencing the overall adsorption rates in packed beds and microfibrinous entrapped sorbents. Theoretical as well as experimental comparisons of MFES were made with the packed beds of various particle sizes. The slope of a breakthrough curve represents the effective adsorption rate in the sorbent bed. Effect of particle diameter on the slope of the break through curves was studied to understand the influence of inter-particle and intra-particle transport rates.

Further, breakthrough curves from packed beds diluted with inerts have been used to demonstrate the presence of axial diffusion and flow maldistributions. Bed dilution has been used in many studies to analyze the effect of axial dispersion [2.1-2.4]. Also breakthrough curves from activated carbon particles entrapped in microfibrinous matrices were obtained. A mathematical model accounting for axial molecular diffusion and intra-bed flow maldistributions was used to explain the experimental results. Finally, with the help of these comprehensive set of experiments and mathematical analysis, the negative effect of channeling and axial dispersion on the performance of packed beds vis-à-vis the benefits of the uniformity and high voidages in MFES was examined.



## II.2. Experimental Details

### II.2.1. Materials

Hexane (Alfa-Aesar, USA) used as adsorbate in this work, consisted of 99% n-hexane and the rest other hexane isomers. The activated carbon adsorbent (bulk density 0.537g/cc) was obtained from Pica USA Inc in the form of 12x20 mesh (0.84-1.68 mm) size particles. This was ground and then sieved using a set of standard sieves to obtain following particle sizes ranges: 20x30 (595-841  $\mu\text{m}$ ), 30x45 (354-595  $\mu\text{m}$ ), 45x60 (250-354  $\mu\text{m}$ ), 60x80 (177-250  $\mu\text{m}$ ) and 80x100 (150-177 $\mu\text{m}$ ) mesh fractions.  $\gamma$ -Alumina (Alfa-Aesar) was used as a bed-support as well as an inert diluent for the ACP.  $\gamma$ -Alumina (bulk density 0.65g/cc) was chosen as it has negligible hexane adsorption capacity. It was obtained in form of 3.2mm cylindrical extrudates and was sized to similar size fractions as the activated carbon. All the above samples of carbon and alumina were dried at 373K for 48hours and stored in air tight containers before being used in the adsorption experiments.

Microfibrinous entrapped sorbents used in this study were made of 0.18-0.25 mm carbon particles and a 19 $\mu\text{m}$  diameter bicomponent (linear low density polyethylene on Polyethylene terephthalate) polymer fibers. The method of preparation of MFES involved a wet lay process for preparation of media sheets followed by sintering at a chosen temperature. In the wet lay process, a uniform suspension of 1.0g of 19  $\mu\text{m}$  polymer fibers and 3.0g of ACP in water was made by rapid stirring. The suspension was transferred into the head box of a paper making equipment, and the excess water was drained to obtain circular sheets (20.3cm diameter) of microfibrinous entrapped carbon media. These sheets were sintered in air at 450K for 5 min and further dried at 373 K for

48hrs. The sheets prepared in this manner had about 12% volume loading of carbon, 3% fibers and the rest voids (85%). Some of these sheets were then compressed using a hydraulic press, to create MFES samples of lower voidage (62.5%).

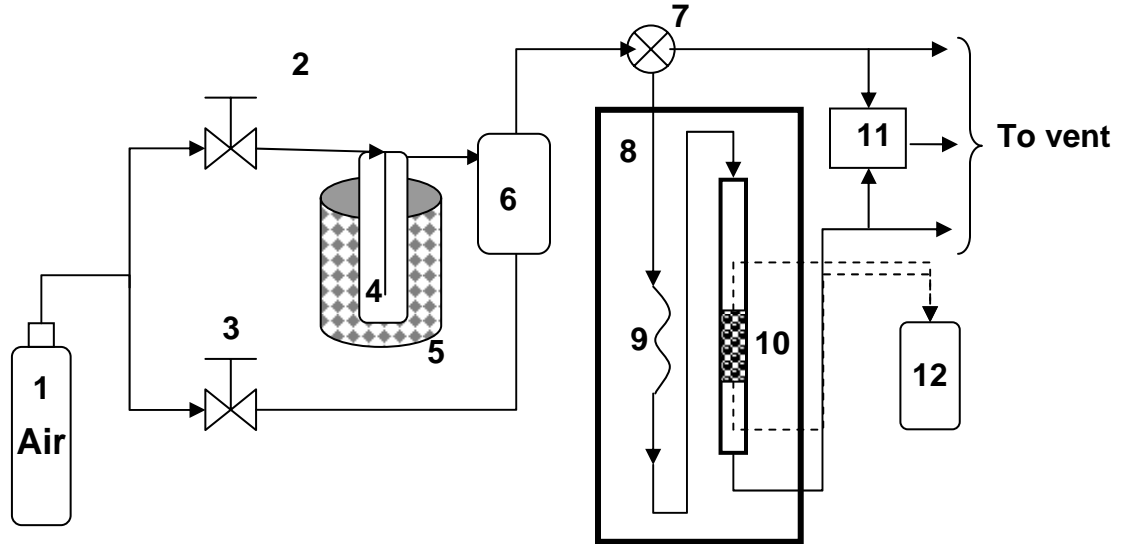
### **II.2.2 Surface Characterization of Pica Activated Carbon**

Surface characterization of fresh carbon as well as on a microfibrinous entrapped sample were done, to determine the effect of MFES preparation procedure on the surface properties. The surface area, total pore volume and pore size distribution of activated carbon was measured using N<sub>2</sub> adsorption/desorption isotherms at 77 K using an AUTOSORB (Quantachrome, USA) automated surface analyzer. Carbon samples were initially outgassed at 423 K for 9 hours before the analysis. The specific surface area was determined using BET isotherm model. BJH method was used to calculate the pore size distribution, pore volumes and average pore size of the sample.

### **II.2.3 Experimental Setup**

A schematic description of the experimental setup used in this study is shown in the Fig. 2.1. The setup can be said to consist of three sections: (a) gas-mixing section, (b) test section, (c) analytical section. In the gas-mixing section two electronic mass flow controllers (FMA-A24 series, Omega) both fed with compressed dry air, were used to gauge and control the flow rates of gas streams used in the generation of hexane challenge. Both the flow controllers were calibrated with a bubble-flow meter (not shown in the Fig.) prior to their use in the experiments. One of the air streams was saturated with hexane at 273K by passing it through a bubbler containing liquid hexane, immersed in an

ice bath. The ice bath was used to maintain a constant liquid hexane temperature which helped obtain a steady gas-phase hexane concentration throughout the course of the experiments. A specific concentration of hexane challenge was generated by diluting the hexane saturated air-stream with fresh air supplied from the second flow controller. The two streams were mixed in a glass chamber, which minimized the fluctuations in the challenge gas concentration. Also the two flow rates were adjusted to obtain a desired total flow entering the adsorbent column.



1. Compressed Air; 2. Mass flow controller-1; 3. Mass flow controller-2; 4.Hexane bubbler; 5. Ice Bath; 6.Glass chamber for gas mixing; 7.Three-way valve; 8.Temperature Controlled Enclosure; 9.Heat exchanger; 10.Adsorption column; 11.VOC detector; 12. Thermometer

**Fig.2.1 Schematic description of the experimental apparatus**

The test section had a temperature controlled oven (Blue-M, Stabil-Therm) which maintained a constant temperature with only  $\pm 0.2$  K variations. An adsorbent column – a glass cell of 210mm long and 25mm diameter - along with a 12.5 mm O.D., 2m long

stainless steel preheating section were located inside the oven. The challenge gas from the mixing chamber was first passed through preheating section (consisting of a stainless steel tube) to achieve a constant temperature before it was sent into the adsorbent column. The adsorbent bed was supported on a fine metal screen positioned on a constriction located at 150mm from the top of the glass adsorbent column. All the experiments were performed with a vertical adsorbent column and the gas flowing in the downward direction. For the particle sizes used in these tests, the ratios of inside diameter of adsorbent column to particle diameter were greater than 33:1. A ratio greater than 10:1 has been recommended by Tien [2.8] to avoid fluid channeling near the wall.

Two K-type thermocouples were placed co-axially in the center of the adsorbent column on the bed surface (one above and one below the adsorbent bed) to measure the bed temperature and any temperature rise across the bed associated with the adsorption process. The temperature of the test bed in all the experiments was maintained at 313 K ( $\pm 0.2$ K) with negligible variation across the bed. Under the test conditions used, the estimated pressure drop across the adsorbent bed was always less than 1 % of the inlet pressure; with the outlet of the adsorbent column let to atmosphere, the entire bed could be said to operate at atmospheric pressure.

The analytical section of the apparatus had a MiniRAE-2000 VOC detector (RAE systems Inc.) with built-in data logging capability. This was used to measure and record the hexane concentration in the inlet and outlet streams. The detector was calibrated with a 100ppm isobutylene calibration gas obtained from RAE systems Inc., and a pre-programmed span of 4.3 was applied to monitor the hexane concentration.

## II.2.4 Experimental Breakthrough Tests

Breakthrough tests were performed by passing the hexane challenge gas into an adsorbent bed and measuring the outlet concentration periodically until it reached the inlet concentration and no further adsorbate uptake by the adsorbent was observed. Three sets of experimental breakthrough tests were conducted. The flow conditions and the weight of ACP used were nearly identical for all the breakthrough tests. The experimental conditions and bed dimensions used are shown in Table 2.1.

**Table 2.1 Experimental flow conditions used in hexane break through tests**

Bed Diameter (mm)	25.0
Total bed height (mm)	18.0 – 40.0
Adsorbent charge (g)	1.45
Temperature (K)	313 ( $\pm 0.2$ )
Pressure (Pa)	$1.013 \times 10^5$
Inlet hexane mol. %	$3.2 \times 10^{-4}$ ( $\pm 2\%$ )
Inlet gas flow rate ( $\text{m}^3 \text{s}^{-1}$ at STP)	$31.795 \times 10^{-6}$ ( $\pm 0.5\%$ )

The first set of breakthrough tests were performed on dried activated carbon samples of different size fractions mentioned above. The test bed in packed bed experiments consisted of three layers: a 1.45g of the ACP sample sandwiched between two 2.0g  $\gamma$ -Alumina layers of the same size fraction on top and bottom. The alumina layers were used to obtain a developed flow pattern in the ACP layer and to avoid any entrance and exit effects on the breakthrough curves. These three layers were further supported on the metal screen placed at the column constriction described before. The second set of breakthrough tests involved diluting the 177-250 $\mu\text{m}$  size activated carbon particles with similar size  $\gamma$ -Alumina in various ratios (D=1 to 5). Calculated weights of

$\gamma$ -Alumina were used to create various volumetric dilutions. The same three-layer bed structure as in the first-set experiments was used here, the top and bottom layers being 2.0g  $\gamma$ -Alumina with diluted carbon bed sandwiched between them. The total bed volume varied with the extent of dilution. The bed voidage of the packed beds was about 0.43. Extreme care was taken to maintain uniform thickness of each of the three layers in all the packed bed experiments.

The final set of experiments involved MFES samples of two different voidages. Both the MFES samples were contained 0.18-0.25 mm ACP and same ACP to fiber ratios. In these experiments, circular discs of 25.4 mm diameter were punched out from bigger sheets of MFES media (prepared as described before). Since the microfibrinous media is flexible, discs slightly bigger in diameter than the adsorbent column diameter (25mm) were utilized in order to get a good seal at the glass wall. A calculated number of these discs containing about 1.45g of carbon were stacked and compressed as necessary to achieve a required void-fraction. It is not always possible to construct a MFES bed containing a specific weight of sorbent, so the closest possible weight was used and the time scale of the breakthrough curve data acquired was adjusted (section II.4.) in order to compare it with packed bed data. The variation in ACP weights in MFES was within 1% of the targeted 1.45g weight. These layered stacks of MFES were then loaded into the adsorbent column, supported directly on the metal screen. The volume of MFES beds for the same amount of carbon differed from that of the undiluted packed bed, because the voidages of the two differed significantly. The properties of the MFES samples used are shown in Table 2.2.

**Table 2.2 Properties of the MFES samples used in hexane tests**

	MFES # 1	MFES # 2
Carbon particle size (mm)	0.18-0.25	0.18-0.25
Fiber diameter ( $\mu\text{m}$ )	19	19
Particle vol. loading (%)	30	12
Fiber vol. loading (%)	7.5	3
Void vol. (%)	62.5	85
Particle to fiber vol. ratio	4	4

### **II.2.5. Adsorption Equilibrium Experiments**

The experiments to obtain adsorption isotherms were performed in the same apparatus described above, with the original adsorption column replaced by a 20cm long, 8mm ID glass cell. Undiluted packed beds of 60-80 mesh activated carbon supported on glass wool were used in these experiments. Depending on the challenge concentration the weight of adsorbent used in the experiments varied from 0.25g to 1.0g for these experiments; smaller quantities were used for smaller inlet concentrations. These variations in weight of adsorbent and the smaller diameter adsorption column were employed in order to expedite the data acquisition time. The adsorption isotherm was obtained by integrating (as described in section II.3.6) the areas above the breakthrough curves at various inlet gas concentrations.

Regeneration of adsorbent was done by flowing fresh air at 313 K over the saturated adsorbent for 48 hrs until no traceable hexane was seen in the outlet stream. The adsorption isotherm was also obtained for the regenerated adsorbent in same way as the fresh adsorbent.

### II.3. Mathematical Model

The mathematical model used to analyze the breakthrough data is based on the transient material balance, transport rates of hexane in the gas phase and inside the particle, equilibrium isotherm and a set of appropriate initial conditions and boundary conditions. The model employed also accounts for axial dispersion of adsorbate due to molecular diffusion as well as flow mal-distribution. By substituting appropriate bed voidages and external mass transfer coefficients the same model could be used for the breakthrough curves of both packed beds as well as microfibrous beds. The following assumptions, which reflect the experimental conditions in this study, were used.

1. Pressure drop across the bed is negligible ( $<1\%$  of absolute pressure).
2. Flow rate remains constant along the bed length. This is based on the above assumption and also the fact that the inlet concentration of the adsorbing species (hexane) is at trace levels ( $\sim 300$  ppmv).
3. Temperature is uniform throughout the bed. This assumption is valid as the adiabatic temperature rise is negligible.
  - Heat of Adsorption of n-Hexane on activated carbon,  $\Delta H_{ad} \approx 43\text{-}82$  kJ/g mole [2.5] depending on the surface coverage of Hexane.
  - Adiabatic temperature rise for complete adsorption,  $\Delta T_{ad} = \Delta H \times C_0 / C_p$
  - For complete adsorption a 300 ppmv n-Hexane in air inlet, with  $C_p = 1\text{ J/g/K}$ ,  
 $\Delta T_{ad} < 1^\circ\text{C}$
4. Instantaneous equilibrium exists between the gas phase hexane in the carbon pores and the hexane adsorbed on the carbon surface.



### II.3.1. Mass Balance

With the above assumptions the differential mass balance of hexane in  $z$  (axial or flow) direction in the bed of voidage  $\varepsilon_b$  results in the following equation.

$$\frac{\partial C_b}{\partial t} = D_z \frac{\partial^2 C_b}{\partial z^2} - u_{in} \frac{\partial C_b}{\partial z} - \left( \frac{1 - \varepsilon_b}{\varepsilon_b \cdot D} \right) \frac{\partial \bar{q}}{\partial t} \quad (2.1)$$

The terms in the above equation are transient, axial dispersion, convective and adsorbate uptake rate (by the adsorbent particles) in the order mentioned.

### II.3.2 Initial and Boundary Conditions

A step change in inlet concentration is induced at  $t=0$ .

$$t = 0, \quad 0 \leq z \leq L \quad C_b = 0, \quad \bar{q} = 0 \quad (2.2)$$

An inlet diffusion boundary condition has been used at the inlet.

$$z = 0, \quad t \geq 0 \quad C_0 = C_b - \frac{D_L}{u_{in}} \frac{\partial C_b}{\partial z} \quad (2.3)$$

At the out let boundary the following was used.

$$z = L, \quad t \geq 0 \quad \frac{\partial C_b}{\partial z} = 0 \quad (2.4)$$

### II.3.3 Gas Phase Mass Transfer

The gas film mass transfer rate to the particle surface was obtained using the following equation:

$$\frac{\partial \bar{q}}{\partial t} = k_m a_c (C_b - C_p) \quad (2.5)$$

The gas-solid mass transfer coefficients for packed beds as well as MFES were estimated using Pfeffer's equation (Equation 2.6) [2.7]. Pfeffer's equation was derived from a theoretical model and is specifically intended for particle beds operating in laminar flow conditions. It also has voidage dependent terms for predicting mass transfer coefficients in high voidage beds. Most of the other semi-empirical correlations widely used for predicting packed bed mass transfer coefficients, are applicable only over a limited voidage range and hence can not be used for MFES. Also, the applicability of this equation for packed beds has been verified for  $Re < 70$  by the author.

$$Sh = \frac{1.26(1 - \zeta)^{(1/5)} (Re.Sc)^{(1/3)}}{\psi} \quad (2.6)$$

where,

$$\psi = 2 - 3\zeta + 3\zeta^5 - 2\zeta^6 \quad (2.7)$$

$$\zeta = (1 - \varepsilon_b)^{(1/3)} \quad (2.8)$$

The mass transfer coefficients in diluted packed beds were assumed to be same as the undiluted beds. And for MFES, as there is no significant lateral mixing caused by the fibers in low  $Re$  gas flows, the presence of fibers was neglected in the mass transfer calculations.

### II.3.4 Axial Dispersion

The axial dispersion coefficients for packed beds were estimated using Edwards and Richardson's [2.6] semi-empirical correlation.

$$\frac{1}{Pe_{dp}} = \frac{\gamma_1 \varepsilon_b}{Re Sc} + \frac{1}{Pe_{\infty} (1 + \frac{\beta \gamma_1 \varepsilon_b}{Re Sc})} \quad (2.9)$$

$$Pe_L = Pe_{dp} \times \left(\frac{L}{d_p}\right) \quad (2.10)$$

In equation (2.9) the first term represents molecular diffusion in the axial direction.  $\gamma_1$ , the bed tortuosity factor, can be estimated using the following equation.

$$\gamma_1 = 0.45 + 0.55 \varepsilon_b \quad (2.11)$$

The second term in equation (2.9) was basically meant to account for axial dispersion due to interparticle velocity variations and eddy mixing; the term containing  $\beta$  in its denominator, relates to the effect of radial mixing on concentration gradients caused by interparticle velocity variations. Edwards and Richardson recommended values of  $Pe_{\infty} = 2.0$  and  $\beta=13$  for packed beds to account for this effect. But, they also noted that in fine particles beds, formation of intra-bed channels can produce axial dispersion coefficients higher than that predicted with the use of these values for  $\beta$  and  $Pe_{\infty}$  in equation (2.9). The contribution of the second term in equation (2.9) with these values of  $\beta$  and  $Pe_{\infty}$  is negligible at low Re. So, to include the effect of the intrabed channeling in packed bed dispersion coefficients, Langer *et al.* proposed a particle diameter dependent correlation for estimation of  $Pe_{\infty}$  [2.13] for particle diameters smaller than 0.3 cm. They also suggested the use of a  $\beta < 8$  for smaller particle beds. A value of  $\beta=1$  was used for undiluted packed beds in this study.

Bed dilution can decrease the effect of axial molecular diffusion as the axial concentration gradients are decreased with dilution; this effect is accounted for, in the

form of a proportionate increase in  $Pe_L$  (molecular diffusion contribution) with increase in bed length (resulting from the bed dilution). Bed dilution, on the other hand, does not directly affect channeling in packed beds. But, as bed dilution increases the fluid residence time in the bed, it permits proportionately more radial dispersion, which in turn can minimize the negative effect of channeling. To model these effects of channeling in diluted beds, the limiting Peclet number correlation proposed by Langer *et al.* and  $\beta$  were modified.

$$\begin{aligned} Pe_{\infty} &= 6.7 d_p / D & d_p < 0.3 \text{ cm} \\ &= 2.0 & d_p > 0.3 \text{ cm} \end{aligned} \quad (2.12)$$

$$\beta = 1 \times D \quad (2.13)$$

This inclusion of bed dilution factor ( $D$ ) in the above  $Pe_{\infty}$  and  $\beta$  calculations (equation 2.12 & 2.13 respectively) keeps the effect of channeling constant while increasing the radial dispersion proportionately with bed dilution. Without the inclusion of  $D$  in  $Pe_{\infty}$  correlation, the effect of channeling in diluted beds (as evident from  $Pe_L$  calculations) would be greatly underestimated due to the bed length increase. This dilution factor correction of  $Pe_{\infty}$  and  $\beta$  is valid only when flow channeling is the predominant form of the axial dispersion and turbulence or eddy mixing is negligible, which is the case in this study. Further, to analyze the individual effect of channeling and axial diffusion, some of the numerical simulations of breakthrough curves were also repeated with  $Pe_{\infty} = 2.0$  and  $\beta=13$ .

For MFES there were no preexistent correlations to predict the axial dispersion coefficients. But, as can be seen from a simple derivation of equation (2.9) given by

Ruthven [2.6], this Peclet number correlation has the required voidage dependent terms to account for the various effects of bed voidage. In absence of any other correlations specifically meant for high voidage beds, it was felt reasonable to apply it for MFES. Also, fibers are not expected to influence the axial dispersion in MFES for same reasons as that mentioned in section II.3.3 and their presence was also neglected in axial dispersion calculations, except for bed voidage calculations. Further the use of this correlation for MFES will be justified in the results section, as the results obtained using this were found to be in good agreement with the experimental results.

### II.3.5 Intraparticle mass transfer

Linear driving force model was used for modeling the intraparticle mass transfer rates.

$$\frac{\partial \bar{q}}{\partial t} = k_p (q_s - \bar{q}) \quad (2.14)$$

where  $k_p$ , the intraparticle mass transfer coefficient was estimated using following equation:

$$k_p = \frac{60 \varepsilon_p D_e}{d_p^2 K_0} \quad (2.15)$$

The effective particle diffusivity  $D_e$  in equation (2.15) was determined using the following equation.

$$\frac{1}{D_e} = \frac{\tau_p}{D_m} + \frac{1}{\frac{D_k}{\tau_p} + \frac{1 - \varepsilon_p}{\varepsilon_p} \frac{D_s}{\tau_s} K_0} \quad (2.16)$$

The surface diffusivity  $D_s$  of hexane on carbon was estimated from the empirical correlation developed by Gilliland *et al.* [2.8]. And the value of kinetic diffusivity was calculated using following equation [2.8].

$$D_k = 9700 r_0 \sqrt{\frac{T}{M}} \quad (2.17)$$

### II.3.6 Adsorption isotherm and capacity calculation

The Freundlich model was used for the adsorption equilibrium isotherm as there was good fit with the experimentally obtained equilibrium data (Section II.4.1) and also because of its simplicity in numerical calculations.

$$q_e = K_e C_b^{1/n} \quad (2.18)$$

The equilibrium capacities can be determined from breakthrough curves by integrating the area over the breakthrough curves as follows:

$$q_e = \left( \frac{u_{in}}{\rho_p L} \right) \left( \frac{\varepsilon_b}{1 - \varepsilon_b} \right) \times \int_0^\infty (C_0 - C) dt \quad (2.19)$$

And the adsorbent utilization was estimated as follows:

$$Adsorbent \text{ utilization} = \left\{ \int_0^{tb} \left( 1 - \frac{C}{C_0} \right) dt \right\} \left/ \left\{ \int_0^\infty \left( 1 - \frac{C}{C_0} \right) dt \right\} \right. \quad (2.20)$$

### II. 3.7 Simplification and numerical solution of the governing equations:

The following dimensionless concentration variables have been used in the above governing equations.

$$Y = C_b / C_0 \quad W = \bar{q} / q_0 \quad (2.21)$$

Rewriting equation (1) in terms of dimensionless parameters

$$\frac{\partial Y}{\partial \tau} = \frac{1}{Pe_L} \frac{\partial^2 Y}{\partial X^2} - \frac{\partial Y}{\partial X} - \left( \frac{1 - \varepsilon_b}{\varepsilon_b} \right) \frac{\partial W}{\partial \tau} \quad (2.22)$$

$$X = \frac{z}{L}, \quad \tau = \frac{tu}{L} \quad (2.23)$$

Equations (5) and (14) in dimensionless form are:

$$\frac{\partial W}{\partial \tau} = k_p \frac{L}{u_{in}} (W_s - W) = \frac{k_m a_c}{K_0} \frac{L}{u_{in}} (Y - Y_s) \quad (2.24)$$

These dimensionless coupled partial differential equations were solved using a semi-implicit finite difference numerical scheme to obtain the solutions. The finite difference scheme was second order accurate in both time and space. Hexane breakthrough curves for all the cases of MFES and packed beds used in experiments have been obtained for a step change in inlet concentration. The experimental operating conditions shown in Table 2.1, along with the various parameters values shown in Table 2.3 and equilibrium data obtained from the experiments (Section II.4.1) were used in these numerical simulations.

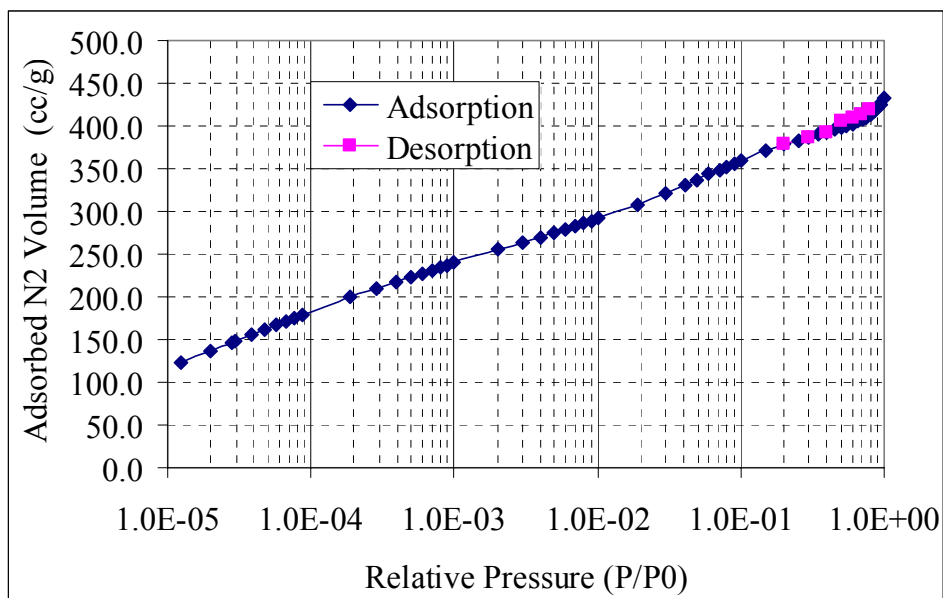
**Table 2.3. Values of various parameters used in the model.**

$D_m$ (m <sup>2</sup> s <sup>-1</sup> )	8.35 x 10 <sup>-6</sup>
$D_s$ (m <sup>2</sup> s <sup>-1</sup> )	2.0 x 10 <sup>-8</sup>
$r_0$ (m)	1.8 x 10 <sup>-9</sup>
$\varepsilon_p$	0.57
$\phi$	0.65
$\nu$	1.56 x 10 <sup>-5</sup>
$\tau_p, \tau_s$	4.0

## II.4. Results and Discussion

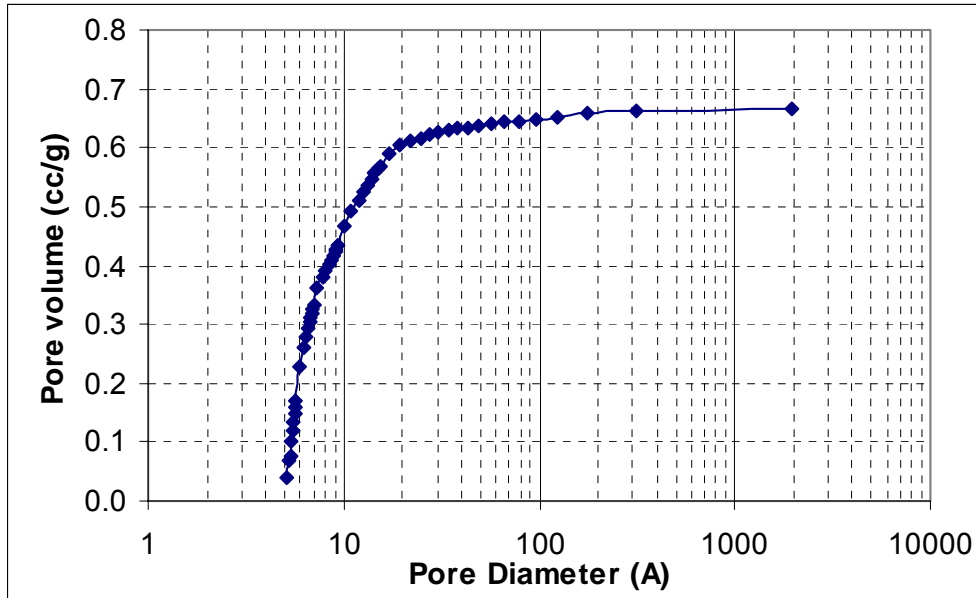
### II.4.1. Surface Characterization

Fig. 2.2(a) and (b) show  $N_2$  adsorption isotherm and pore size distribution graphs of fresh Pica carbon. Plots for MFES samples looked more or less similar to this plot. The BET surface area, total pore volumes and average pore diameter of fresh carbon as well as MFES sample are given in Table 2.4. The values of fresh and microfibrinous entrapped carbon both are almost similar and the difference is within the experimental error range.



**Fig.2.2(a)**





**Fig.2.2(b)**

**Fig. 2.2(a) N2 Adsorption isotherm on carbon and (b) Carbon pore size distribution**

**Table 2.4. Properties of Pica activated carbon**

Property of Activated Carbon	Fresh sample	MFES sample
BET Surface Area(m <sup>2</sup> /g)	1322	1255
Pore Volume - $\varepsilon_p$ (cc/g)	0.67	0.61
Average Pore Diameter - $r_0$ (Å)	20.3	19.3

#### **II.4.2. Equilibrium isotherm**

A summary of the adsorption equilibrium data, for a gas phase hexane concentration range of 25ppmv to 500ppmv at 313K, is shown in Fig. 2.3. This was an essential input needed for the mathematical model developed, and it is also important for

understanding the nature of the adsorption process. A good fit with Freundlich model ( $q_e = K_e C^{1/n}$ ) was obtained. A value of  $n=6.54$  ( $=1/0.153$ ) was obtained from the equilibrium data fit. The data shows a highly favorable isotherm. Fig. 2.3 also shows the isotherm for a regenerated sorbent. The regenerated carbon sorbent has a decreased capacity compared to the fresh sorbent. This shows that a part of the hexane adsorbed on the fresh sorbent is irreversibly adsorbed.

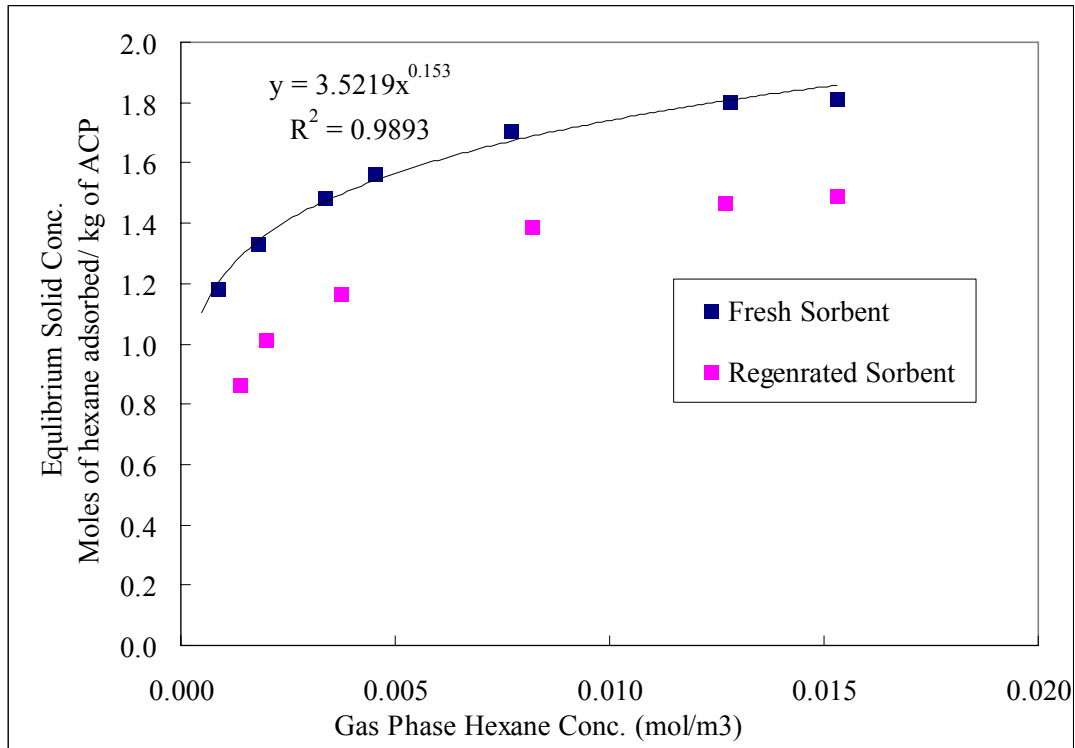


**Fig. 2.3. Experimental equilibrium data of hexane/Pica activated carbon & the Freundlich isotherm fit at 313K**

#### II.4.3 Breakthrough tests

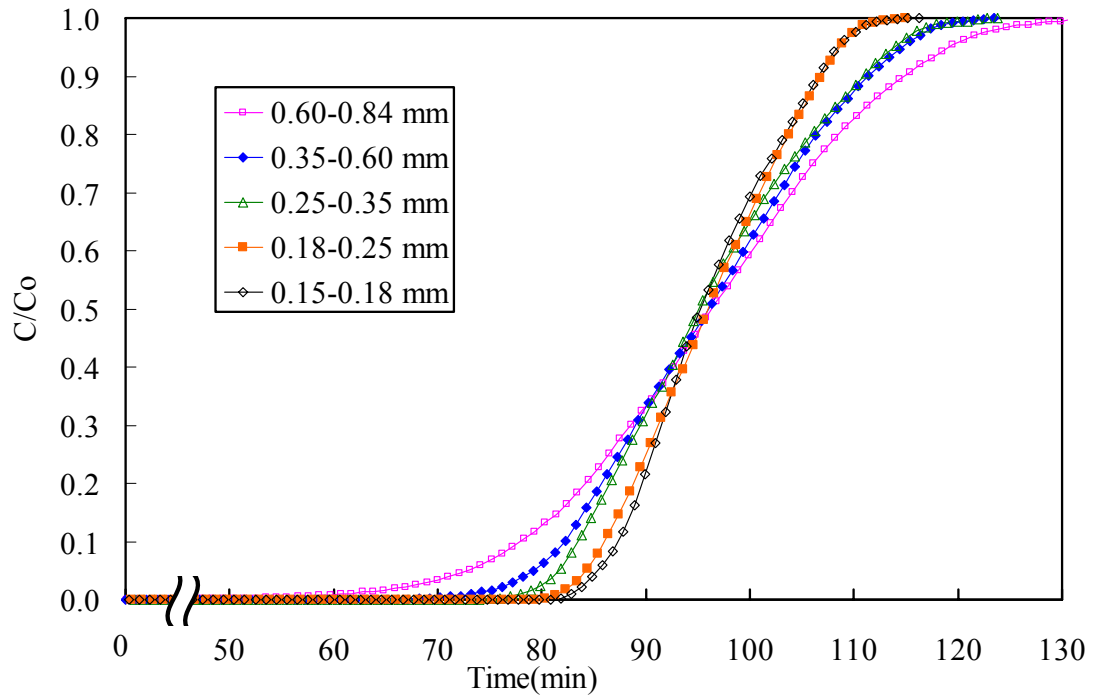
Experimental hexane breakthrough data was obtained for different bed configurations (packed bed particle size and bed dilution variations and MFES) as described before (section II.2.). The inlet challenge concentration and flow rate (Table

2.1) were relatively constant, with minor fluctuations ( $\pm 2$  ppmv), over the time range of any breakthrough test. But variations in inlet flow rate ( $\pm 0.5\%$ ) and concentrations ( $\pm 7$  ppmv) also existed from one breakthrough test to another due to replicability limitations of the mass flow controllers used. To compensate for these minor variations in inlet concentration and flow rates, the time scales of all the experimental breakthrough curves obtained have been corrected by multiplication of suitable correction factors to match the equilibrium capacity corresponding to a constant 320 ppmv hexane gas phase concentration. This adjustment in the total capacity of adsorbent beds also compensated for the minor differences in the weights of ACP used in the MFES tests.

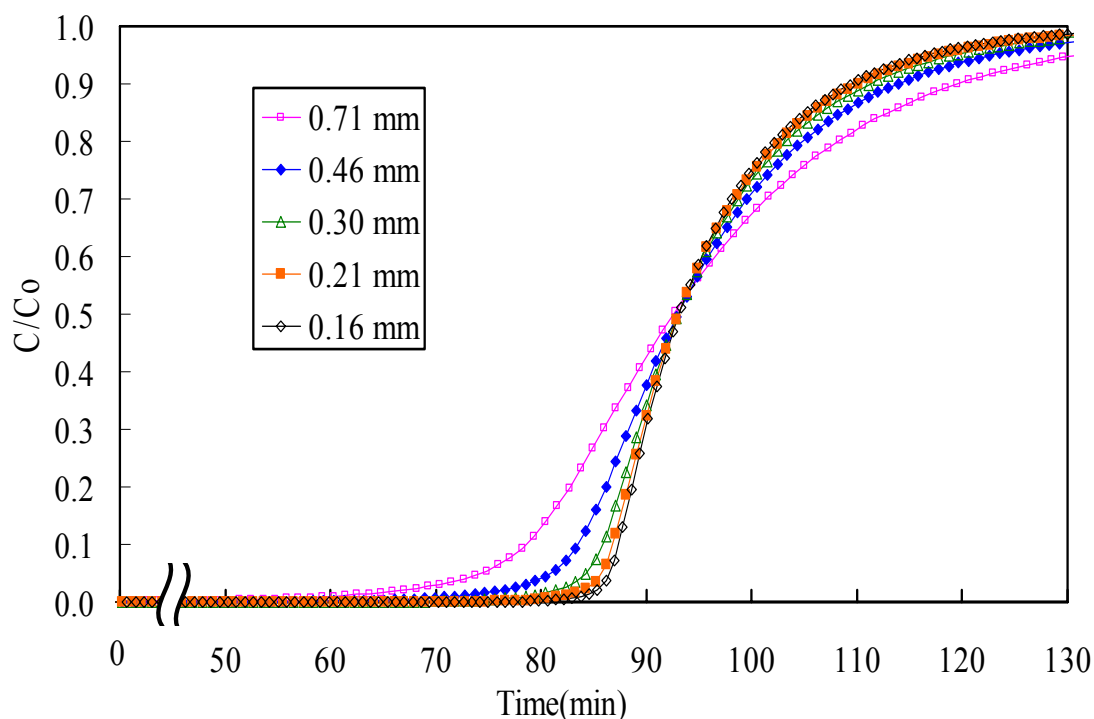
The outlet concentrations remained zero for the initial part of all the breakthrough tests. A part of this zero outlet concentration region is skipped or not shown in the breakthrough graphs presented in this section. For the purpose of this study breakthrough concentration was defined as 1% (3.2 ppmv) of inlet hexane concentration. And as expected based on the adiabatic temperature rise calculations (section II.3), no significant temperature rise was observed across the adsorbent bed during any of the experiments; this eliminates the possibility of any heat transfer effects on the adsorbent uptake rate.

Fig. 2.4 shows the experimental hexane breakthrough curves from undiluted packed beds of different ACP sizes. The sharpness of the breakthrough curves increased with decreasing particle size. This indicates an increase in the effective adsorption rate with decrease in particle size. Fig. 2.5 shows the breakthrough curves for the above experimental particle sizes as predicted by the mathematical model. The particle diameters mentioned in Fig. 2.5 correspond to the log mean values for the particle size fractions used in the experiments. The model predicts the exact trends shown by the

experimental breakthrough curves. Table 2.5 shows the comparisons of the experimental (from Fig.2.4) and model based (from Fig. 2.5) breakthrough times and percentage adsorbent utilization values for various particle sizes. The values found from the numerical simulations were in good agreement with the experimental values. This increase in adsorption rate was found to be a direct result of the increase in external surface area of the particles and intraparticle and interphase mass transport rates associated with decreasing particle size.



**Fig.2.4. Experimental breakthrough curves from undiluted packed beds of various particle sizes**



**Fig.2.5. Model predictions of the breakthrough curves of undiluted packed beds of various particle sizes**

**Table 2.5. Experimental and predicted breakthrough times and adsorbent utilization values for packed beds of different particle sizes**

ACP size (mm)	Breakthrough Time (min)		% Adsorbent Utilization	
	Experimental	Predicted	Experimental	Predicted
<b>0.60-0.84</b>	60.96	60.12	63.44	62.43
<b>0.35-0.60</b>	73.45	71.77	76.45	74.58
<b>0.25-0.35</b>	77.74	78.62	80.89	81.73
<b>0.18-0.25</b>	81.38	81.98	84.68	85.23
<b>0.15-0.18</b>	82.79	83.76	86.17	87.10

Fig. 2.6 shows the experimental breakthrough results from packed beds with various levels of bed dilution ( $D=1$  to 5) and MFES samples of various bed voidages. In all these breakthrough tests, the particle size fraction of ACP as well as the  $\gamma$ -alumina diluent (wherever used) was kept constant (0.18-0.25 mm). The breakthrough time and

slope of the breakthrough curves and hence, the effective adsorption rate in packed beds improved with increase in bed dilution. The breakthrough curves from MFES beds were significantly sharper than that of the packed beds and the breakthrough times of MFES improved with increasing voidage.

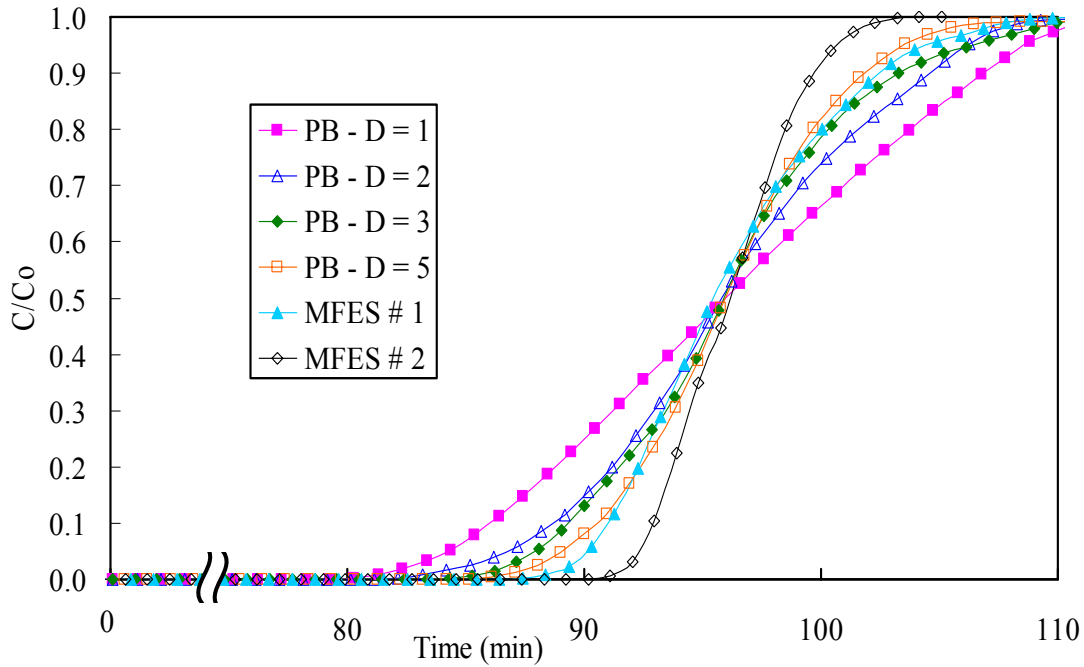


**Fig. 2.6. Experimental breakthrough curves of packed beds (PB) of various bed dilution levels and MFES beds of various bed voidages (0.18-0.25 mm particles).**

The intraparticle transport coefficients, which are dependent only on the particle diffusivity and diameter, remain the same for all these cases of packed beds and MFES shown in Fig. 2.6. Fluid-solid mass transfer coefficients in packed beds at high bed dilutions ( $D > 10$ ) can be lower than that of undiluted beds [2.14, 2.15], although they are relatively unaffected at low bed dilutions. Also, voidage increase in fixed beds tends to lower the interphase mass transfer coefficients as the interparticle spacing is increased. Although the fibers in MFES matrices can act as static mixers and thereby enhance the mass transfer coefficients, at low Re gas phase flows significant enhancement in mass

transfer rate due to this effect is not anticipated. Therefore, the mass transfer coefficients in the MFES beds can be expected to be slightly lower than that of the packed beds of same particle size. This decrease in mass transport coefficients with increasing dilution and voidage, even if significant, is contrary to the trends in the effective reaction rates seen here. Therefore, the trends observed in Fig. 2.6 can not be associated with interphase and intraparticle mass transport rates.

In absence of any heat transfer effects and in view of the above discussion, the results shown in Fig. 2.6 can only be attributed to axial dispersion due to molecular diffusion and/or intrabed channeling. The individual influence of each of these factors in the above experimental cases was further probed with the help of the mathematical model described before. Fig.2.7 shows the results of breakthrough curves obtained from numerical simulations for all the different cases of packed beds and MFES shown in Fig. 2.6. In these calculations a particle diameter of 0.21 mm was used, which is a log mean of 0.18-0.25 mm size fraction used in experiments. The effects of axial molecular diffusion and flow maldistributions were included in Fig.2.7 by using  $\beta$  and  $Pe_{\infty}$  values (in equation 2.9) calculated from Equation (2.12) and (2.13). Table 2.6 shows a comparison of breakthrough times and adsorbent utilizations values obtained from the experiments (Fig.2.6) and the model (Fig. 2.7). Except for a few deviations, the model appears to compare well with the experiments.

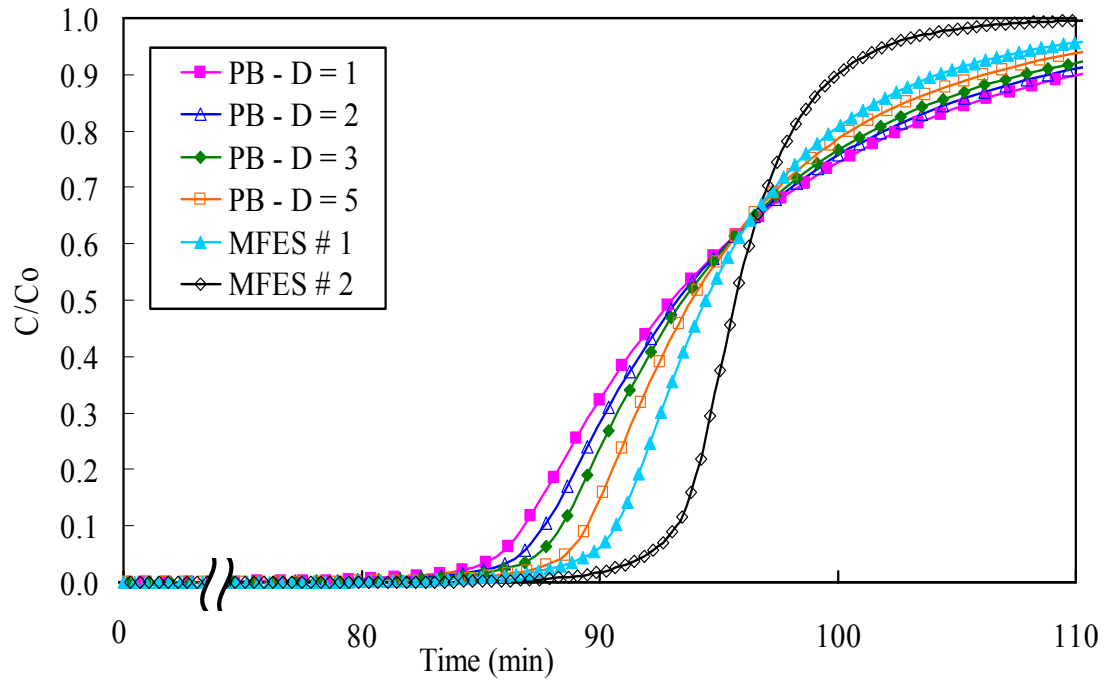


**Fig. 2.7. Model predictions of breakthrough curves of packed beds (PB) with various bed dilution levels and MFES beds of various voidages (effect of flow maldistributions included).**

**Table 2.6. Comparisons of experimental and predicted breakthrough times and adsorbent utilizations for various cases shown in Fig. 2.6 & 2.7**

Bed Type	Breakthrough Time (min)		% Adsorbent Utilization	
	Experimental	Predicted	Experimental	Predicted
<b>PB D=1</b>	81.38	81.98	84.68	85.23
<b>PB D=2</b>	83.55	83.02	86.96	86.31
<b>PB D=3</b>	84.76	83.87	88.19	87.18
<b>PB D=5</b>	86.86	85.22	90.37	88.61
<b>MFEC#1*</b>	88.53	85.71	92.12	89.09
<b>MFEC#2*</b>	91.29	88.81	94.97	92.33

Table 2.7 shows the ACP volume loadings, bed voidages, gas residence times and associated inverse Peclet number ( $1/Pe_L = D_z/u_{in}L$ ) values for all the cases shown in Fig.2.7. The percentage volume loadings of ACP mentioned for packed beds are based on an experimentally measured voidage of about 43% (particle volume loading of about



57%). The inverse Peclet number based on the bed length ( $1/Pe_L$ ) is representative of the magnitude of axial dispersion effects present in an adsorbent bed. The inverse  $Pe_L$  values for packed beds decreased with increasing dilution, representing a decrease in axial dispersion. The inverse Peclet numbers for MFES were found to be up to an order of magnitude smaller than that of the packed beds and these values for MFES decreased with increasing voidage.

**Table 2.7. Comparisons of bed properties, residence times and inverse Peclet number ( $1/Pe_L$ ) values for various for various cases shown in Fig. 2.7**

<b>Bed Type</b>	<b>ACP vol. loading</b>	<b>Bed Voidage</b>	<b>Residence Time (ms)</b>	<b><math>1/Pe_L</math></b>
<b>PB D=1</b>	<b>57.0%</b>	<b>43.0%</b>	<b>31.8</b>	<b>0.369</b>
<b>PB D=2</b>	<b>28.5%</b>	<b>43.0%</b>	<b>63.6</b>	<b>0.321</b>
<b>PB D=3</b>	<b>19.0%</b>	<b>43.0%</b>	<b>95.4</b>	<b>0.286</b>
<b>PB D=5</b>	<b>11.4%</b>	<b>43.0%</b>	<b>159.0</b>	<b>0.235</b>
<b>MFES#1</b>	<b>30.0%</b>	<b>62.5%</b>	<b>87.9</b>	<b>0.179</b>
<b>MFES#2</b>	<b>12.0%</b>	<b>85.0%</b>	<b>298.9</b>	<b>0.066</b>

Finally, the numerical runs for packed beds ( $D=1, 3$ ) as well as MFES#2 were repeated with the Peclet numbers calculated using  $\beta=13$  and  $Pe_\infty = 2.0$ . Essentially, this accounts only for the effect of axial molecular diffusion and interparticle velocity variations, with the effect of flow maldistributions being ignored. The results are shown in Fig. 2.8. The rest of the cases shown in Fig.2.7 were skipped as there was a lot of overlapping among the breakthrough curves. Although there is a performance improvement in packed bed with  $D=3$  and in MFES, compared to undiluted packed beds, the improvements found were very small and not comparable with those found in corresponding experimental results (Fig.2.6). This shows that the effects of axial

diffusion and interparticle velocity variations (due to formation of velocity profiles), are relatively insignificant for the conditions of these experiments. Although both these effects were insignificant for the conditions of the present study, the contribution of molecular diffusion (first term in equation 2.9) was found to be relatively more than that of the interparticle velocity variations.

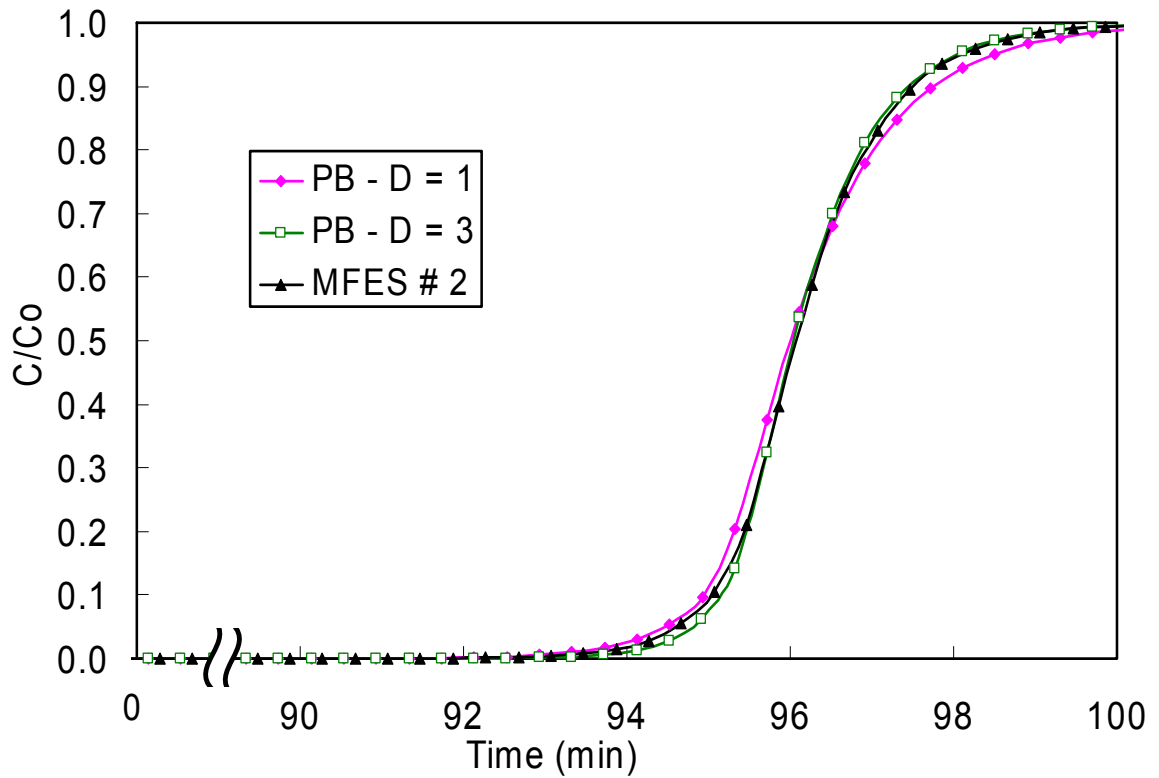


**Fig. 2.8. Model predictions of breakthrough curves of packed beds (PB) of various bed dilutions and MFES#2 bed (effect of flow maldistributions neglected)**

Having eliminated the possibility of all other contributions to axial dispersion, the results in Fig. 2.6 & 2.7 (and Table 2.6 & 2.7) clearly point to the significant presence of intrabed channeling or flow maldistributions arising from non-uniformities or particle clusters present in small particle packed beds. As discussed earlier, the increase in bed dilution does not directly affect intrabed channeling, but the resultant increase in

residence time helps increase radial diffusion. This increase in radial diffusion tends to create a more uniform concentration across bed cross-section and thereby the negative effect of flow maldistributions is decreased. While bed dilution results in a proportionate increase in pressure drop, it does not necessarily decrease axial dispersion effects significantly. The positive effects of the increasing residence time on radial dispersion and its impact on minimizing axial dispersion were also seen in the MFES samples. Both the MFES samples used were identical in all respects except for their bed voidage (and particle volume loadings). But, the higher voidage sample (MFES#2) performed better than the lower voidage sample (MFES#1). This signifies the benefit of higher voidages in achieving better radial dispersion. Further, although the packed beds with  $D > 2.8$  have higher residence times compared to MFES#1, performance of MFES#1 was found to be far better than packed beds with  $D = 3$  &  $5$ . This indicates that MFES structures are inherently more uniform compared to packed beds. This structural uniformity also aids in minimizing flow maldistributions in MFES. Hence, the benefits of MFES beds can be said to be derived from both the structural uniformity and the open flow paths (high voidages) present in them.

These results and explanation do not completely undermine the effect of the axial diffusion. Axial diffusion can also become an influential factor in reactions/adsorption processes involving higher molecular diffusivities and/or lower velocities. Hexane in air at 313K has relatively low molecular diffusivity compared to other applications that involve lower molecular weight compounds and/or higher temperatures and pressures. In processes involving higher molecular diffusivities compounds, the trend shown in Fig.2.8 becomes more prominent due to higher axial diffusion. Also, with higher molecular

diffusivities, the term containing  $\beta$  in equation (2.9) increases, i.e., radial dispersion increases and hence the effect of channeling is reduced. But even in this case, MFES are expected to perform better than undiluted packed beds.

The model used here, does not reproduce the exact shape of the experimental breakthrough curves, but it reproduces the exact trends. Also breakthrough times and adsorbent utilizations predicted for various particle diameters and bed dilutions are reasonably close to the experimental values. A more rigorous model for flow maldistributions in fixed beds would consist of two parallel zones inside the adsorbent bed with different voidages along an appropriate mass flux of adsorbate between the two zones (similar to the one developed by Martin [2.16]). But this would involve more variable parameters. Therefore, a simple model with a variable axial dispersion coefficient was used in this study. In view of these results, a more comprehensive analysis using commercial computational fluid dynamics software is being attempted. Also a detailed experimental study of axial dispersion coefficients in packed beds and MFES and its dependence on particle diameters,  $L/d_t$  and  $d_t/d_p$  ratios, diffusivities, etc, is being planned as a part of our future work.

Lastly, the results obtained here may be applicable only to small particle beds. But, as small particle sizes reduce interphase and intraparticle mass transport resistances, the results obtained here have a great significance for applications where higher reaction/adsorption rates are vital. The results also underline the advantages of using microfibrinous entrapped catalysts and sorbents for such demanding applications.

## II.5. Conclusions

The effects of transport (interphase and intraparticle) resistances and axial dispersion due to molecular diffusion and flow maldistributions on the performance of packed beds and MFES were analyzed. This analysis was further used to explain the enhancement in adsorption rates observed in MFES. The sharpness and breakthrough time of the breakthrough curves increased with decrease in particle size in packed beds. This indicates a considerable presence of transport limitations in larger particle beds. As MFES technology utilizes significantly smaller particle diameters compared to the commercial packed bed systems, it has some major benefits in the form of reduced intraparticle and interphase transport resistances.

Further, performance comparisons of diluted packed beds and MFES of various voidages illustrated the effects of axial diffusion and intrabed flow maldistributions. Diluting the bed reduced the axial concentration gradients and also improved the radial dispersion. But, this decreased the negative effect of flow maldistributions only to a small extent. On the other hand, the negative effect of flow maldistributions was found to be significantly lower in MFES beds. This was found to be a direct result of high voidages and structural uniformity inherently present in MFES. While the open structures of MFES promoted radial dispersion which in turn led to more uniform radial concentration profiles, the structural uniformity in MFES helped reduce flow maldistributions. These unique properties of MFES lead to the enhancement in adsorption rates compared to packed beds. With this improved perception of the adsorption rate enhancement in MFES, further optimization of their structural properties (voidages, particle and fiber diameters, etc) can be attempted in order to realize their full benefit.

## II.6. Nomenclature

$a_c = (6/\phi d_p)$  = external surf. area per unit vol. of adsorbent (1/m)

$C$  = gas phase adsorbate outlet conc.(mol/m<sup>3</sup>)

$C_0$  = gas phase adsorbate inlet conc.(mol/m<sup>3</sup>)

$C_b$  = gas phase adsorbate conc. in adsorbent bed (mol/m<sup>3</sup>)

$C_s$  = gas phase adsorbate conc. at particle surface (mol/m<sup>3</sup>)

$d_p$  = particle diameter (m)

$d_t$  = bed diameter (m)

$D$  = total solid vol. fraction/ active particle vol. fraction = Bed dilution level

$D_e$  = effective Particle diffusivity(m<sup>2</sup>/s)

$D_k$  = knudsen diffusivity (m<sup>2</sup>/s)

$D_m$  = molecular diffusivity (m<sup>2</sup>/s)

$D_s$  = surface diffusivity (m<sup>2</sup>/s)

$D_z$  = effective axial dispersion coefficient (m<sup>2</sup>/s)

$k_m$  = fluid-solid interphase mass transfer coeff. (m/s)

$k_p$  = intraparticle mass transfer coeff. (1/s)

$K_e$  = freundlich isotherm constant (mol/m<sup>3</sup>)<sup>(n-1)/n</sup>

$K_0 = q_0 / C_0$

$L$  = length of adsorbent bed (m)

$M$  = molecular weight of adsorbate (g/gmol)

$n$  = exponent in Freundlich isotherm

$Pe_{dp} = d_p u_{in}/D_z$  = particle Peclet number

$Pe_L = L u_{in}/D_z$  = Peclet number based on bed length

$Pe_{\infty}$  = limiting Peclet number

$\bar{q}$  = volume-averaged solid phase adsorbate conc. (mol/m<sup>3</sup>)

$q_e$  = equilibrium solid phase adsorbate conc. (mol/m<sup>3</sup>)

$q_s$  = solid phase adsorbate conc. at particle surface (mol/m<sup>3</sup>)

$q_0$  = solid phase adsorbate conc. in equilibrium with inlet gas conc. (mol/m<sup>3</sup>)

$Re = (\phi d_p u_0 / \nu)$  = particle Reynolds number

$Sc = (\nu / D_m)$  = Schmidt number

$Sh = (\phi d_p k_m / D_m)$  = particle Sherwood number

$t$  = time (s)

$t_b$  = breakthrough time(s)

$T$  = temperature (K)

$r_0$  = pore radius of adsorbent (cm)

$u_0$  = superficial gas velocity (m/s)

$u_{in} = (u_0 / \epsilon_b)$  interstitial gas velocity (m/s)

$X$  = dimensionless axial length

$Y$  = dimensionless gas phase adsorbate concentration

$W$  = dimensionless solid phase adsorbate concentration

$z$  = axial length (m)

$\beta$  = radial dispersion parameter

$\phi$  = sphericity of particle

$\gamma_1$  = bed tortuosity factor

$\epsilon_b$  = bed voidage

$\varepsilon_p$  = particle voidage

$\nu$  = kinematic viscosity

$\rho_p$  = particle density ( $\text{kg/m}^3$ )

$\tau = t u_{\text{in}}/L$  = dimensionless time

$\tau_p$  = adsorbent pore tortuosity

$\tau_s$  = adsorbent surface tortuosity

$\psi, \zeta$  = voidage dependent parameters in Pfeffer's equation



## **CHAPTER III**

### **COMPOSITE BED DESIGN**

#### **III.1. Background**

Composite bed architecture in which a thin layer of microfibrinous media (containing small particles) is placed in series with packed beds of larger particles has shown excellent benefits in many experimental studies [1.7, 1.10 & 3.1]. In this study this composite bed architecture was tested on the similar lines of the hexane breakthrough tests done in the previous chapter. The principle behind this design is to combine the high capacity of the packed beds (because of high volume loading of sorbents which is about 60%) with the high efficiency of MFES layer. As observed previously (chapter II) the large particle packed beds are limited by low mass transfer rates (intraparticle and interphase) and small particle packed beds are limited by high axial dispersion resulting from channeling and axial diffusion. Also as demonstrated in the last chapter MFES can benefit from high adsorption rates resulting from high intraparticle and interphase transport rates and reduced axial dispersion. The addition of MFES layer can improve the breakthrough capacity or in other words the percentage sorbents utilization of the whole bed. Fig. 3.1 shows a schematic of the composite bed architecture. Modeling the breakthrough curves from composite beds is not attempted here.

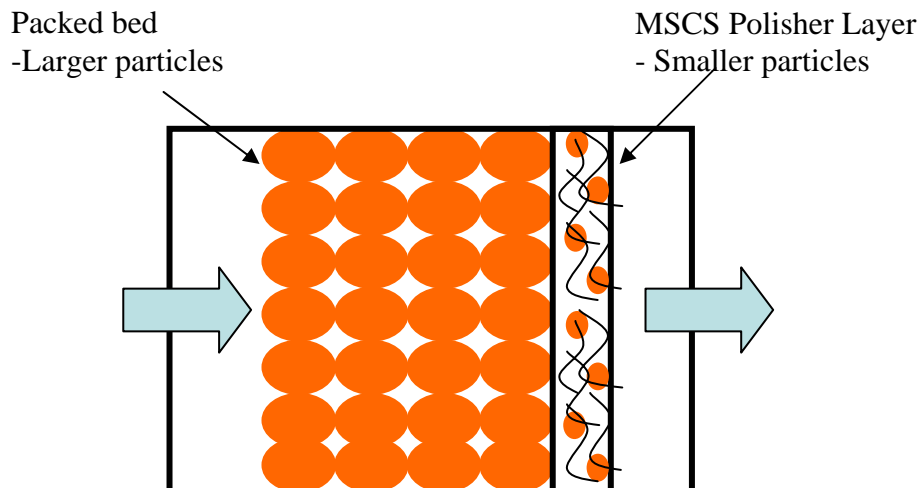


**Fig. 3.1 Schematic diagram of composite bed architecture**

### **III.2. Experimental Details**

The materials used, the experimental apparatus and the inlet flow and operating conditions used in this study are exactly the same as those used in chapter II. These aspects are described in detail in section II.2. In this study, breakthrough tests were made on three different activated carbon bed configurations – packed bed of large particles (A), MFES polisher layer of smaller particles (B) and a composite bed consisting of similar packed bed and polisher layer in series (A+B). First a hexane breakthrough curve was obtained from packed bed of 1.45g of 600-840 $\mu$ m particles. Then the breakthrough test results were obtained from a MFES polishing layer containing 0.12g of activated carbon. The composition and properties of packed beds and the polishing layer are described in table 3.1. Finally, a composite bed consisting of a similar polishing layer (as above) placed in series with the packed bed similar to that described above was constructed inside the glass adsorbent column and a breakthrough curve was obtained. The breakthrough times and sorbent utilizations in these three results were compared.

**Table 3.1 Properties of the packed beds and MFES samples used in hexane tests**

	Packed Bed (A)	MFES Polisher (B)
Carbon particle size ( $\mu\text{m}$ )	600-840	177-250
Fiber diameter ( $\mu\text{m}$ )	N/A	19
Carbon weight (g)	1.45	0.12
Approx. Bed height (mm)	6	2.0
Particle vol. loading (%)	57	12
Fiber vol. loading (%)	N/A	3
Void vol. (%)	43	85

### III.3. Results and Discussion

The breakthrough curves from the above mentioned bed configurations are shown in Fig. 3.2. Table 3.2 shows the corresponding breakthrough times and percentage adsorbent utilizations of these breakthrough curves. Breakthrough concentration was defined as 1% of inlet concentration. The breakthrough curve of the MFES polishing layer is very sharp. As the amount of carbon present in it is far less than that in the packed bed the capacity of the polishing layer is less. But as seen in the previous chapter packed bed is inefficient and the breakthrough curve from the packed bed in Fig.3.2 is not as sharp as MFES layer.

In the composite bed architecture, when combined with the high efficiency MFES layer the slope of the resultant breakthrough curve is higher than the packed bed. The combination of a thin layer MFES with packed bed improved the breakthrough time and adsorbent utilization of the resultant bed significantly compared to the packed bed. Although the slope of the composite bed breakthrough curve is in between the slopes of the individual bed breakthrough curves, the breakthrough time of the composite bed is higher than the sum of the breakthrough curves of the polisher and packed beds.

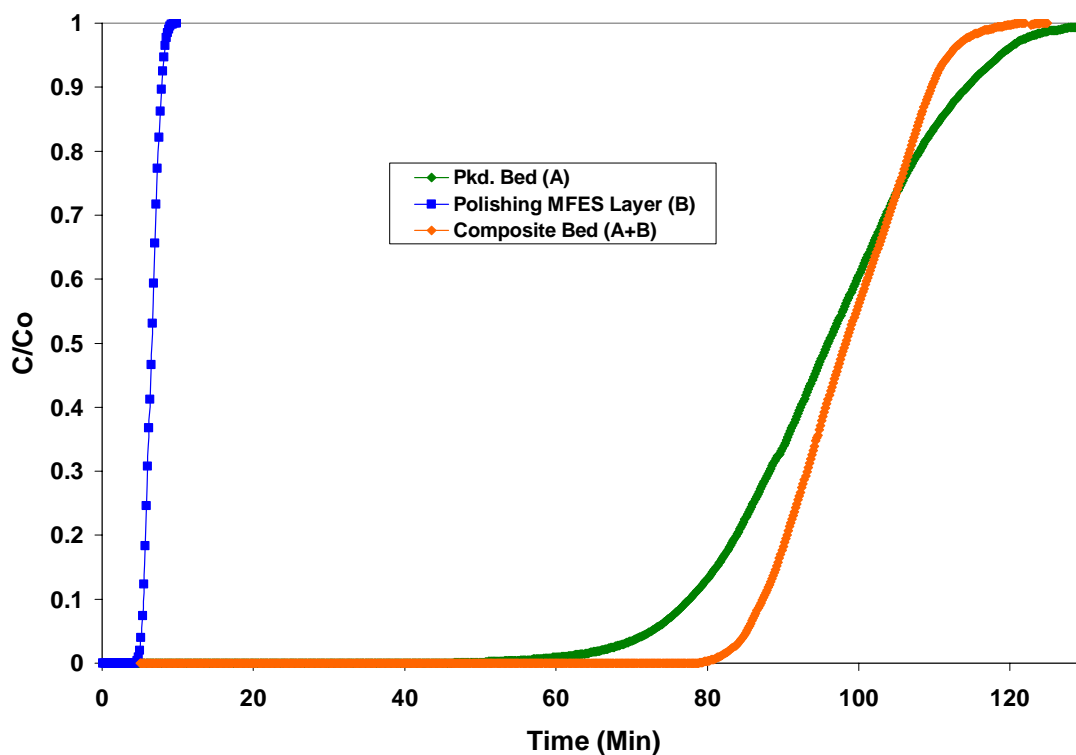


**Fig. 3.2. Breakthrough curves of composite bed and its corresponding components**

**Table 3.2. Experimental breakthrough times and adsorbent utilization values for various bed configurations**

Bed Configuration	Breakthrough Time (min)	% Adsorbent Utilization
Packed Bed (A)	60.96	63.44
MFES Polisher (B)	6.57	98.40
Composite Bed (C)	81.55	82.85

### III.4. Conclusions

Composite bed design was shown to have significant advantages in terms of % adsorbent utilizations and breakthrough times. This novel design has successfully combined the high capacity of packed beds and the high efficiency of MFES beds. This concept can be very useful for applications demanding high capacities and low pressure drops.

## **CHAPTER IV**

### **PRESSURE DROP TESTS**

#### **IV.1. Background**

Minimizing the pressure drop in the flow through any heterogeneous contacting system is an important design criterion. Pressure drop in reactors or adsorbent columns is a big contributor to their operating costs (power for blower or pump). Therefore, the ability to measure and/or predict the pressure drops in MFECS media is an important in optimizing these structures. There are many correlations in literature like Ergun's equation which can predict the pressure drops in packed beds of particles. The major limitation with these correlations is that they were derived for use in low bed voidage (<50%) conditions like a typical packed beds and fail when applied to high voidage fixed beds. Another disadvantage with these conventional pressure drop correlations is that they are not suitable for cases involving multi-particles (more than one kind of materials). But, MFECS consists of multiple particles (catalyst/adsorbent particles and fibers, etc). In a recent effort, Cahela et al. have derived a semi-empirical correlation called as porous media permeability (PMP) equation [1.11] to predict the pressure drop in MFECS media. Using this correlation they have successfully modeled the pressure drop in MFECS media. In this section, a set of microfibrinous media of different bed properties (fiber diameter, voidage, etc) were prepared and pressure drops in these media for various

velocities was measured. Applicability of PMP equation for pressure drops in these samples was verified.

#### IV.2. Experimental Details

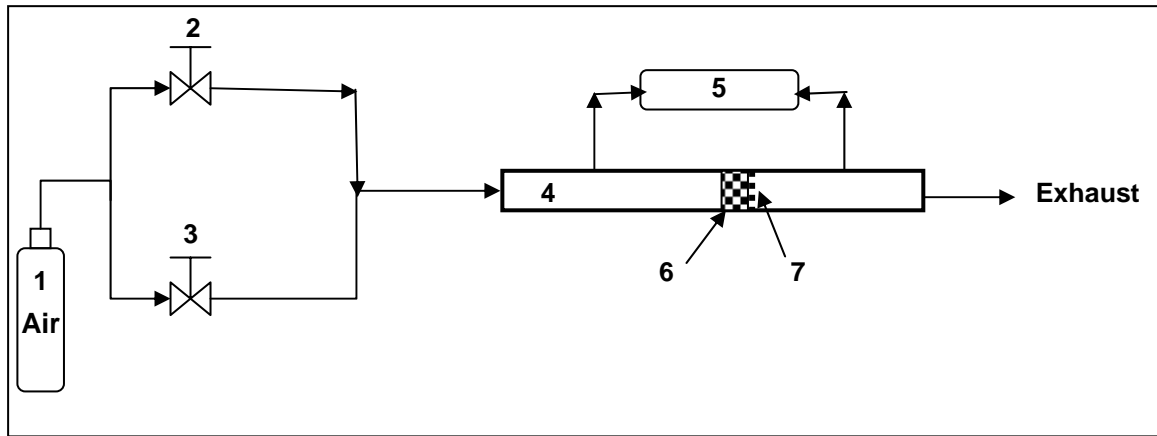
Five samples of microfibrinous media of different bed properties (1 square ft each) were prepared using stainless steel (SS 304) (Intramicron Inc.) fibers.  $\gamma$ -Alumina (Alfa Aesar) was also used in some of these samples. Details of preparation procedure are given in Section I.3.2. All these samples were pre-oxidized at 350 C for 30 minutes and sintered at 1050 C for 1 hour. Table 4.1 gives the details of properties of the microfibrinous samples used in this study. Circular discs of microfibrinous sheets of 1” were cut out of the larger sheets using circular punches for use in this study.

**Table 4.1. Details of sample properties used in pressure drop tests**

Sample		# 1	# 2	# 3	# 4	# 5
Vol. %	12 $\mu\text{m}$ Fiber	7.7	-	-	-	1.2
	8 $\mu\text{m}$ Fiber	-	8.6	3.9	1.8	1.2
	$\text{Al}_2\text{O}_3$	-	-	26.5	12.0	13.6
$\text{Al}_2\text{O}_3$ Size ( $\mu\text{m}$ )		-	-	180-300	180-300	150-180

A schematic diagram of the pressure drop measurement apparatus used in this study is shown in Fig. 4.1. Apparatus consisted of two mass flow controllers (Omega FMA-A24 series 0-50 slpm and 0-35 slpm), a glass sample holder and required tubing and connections. Compressed air was fed to both the controllers and the flow from both the flow controllers was combined at their outlet. The 50 slpm mass flow controller was

used as the primary source of air into the glass sample holder and the 35slpm flow controller was used as a supplementary source when higher flow rates (velocities) were needed. The flow rates of the flow controllers were adjusted to vary the inlet velocities to the samples. The combined flow from the flow controllers was sent in to a glass cell of of 1" ID, where a stack of microfibrinous media was placed for testing. This glass sample holder was made of two individual parts joined together using a metal clamp, with a Teflon gasket sealing the joint. The samples of microfibrinous media were placed on a metal screen held in place at the junction of the two glass tubes. Pressure drop was measured by a digital pressure sensor (Omega, PX154-010DI) and the readings were indicated using a digital display unit (Omega DP24E). Temperature of air flowing inside was measured using a K type thermocouple (Omega), not shown in the figure.



1. Compressed Air; 2. Mass flow controller (0-50slpm); 3. Mass flow controller (0-35slpm); 4. Glass cell; 5. Pressure sensor and display unit; 6. Microfibrinous Media; 7. Metal Screen;

**Figure 4.1 Pressure Drop Measurement Apparatus**

Empty cell pressure drops were measured for selected flow rates in the required range. Pressure drops were also measured with various microfibrinous samples placed in the cell, for exactly same flow rates as above. The actual pressure drop over the media was calculated by subtracting the empty cell pressure drops from the observed pressure drops with the media inside the cell.

#### **IV.3. Mathematical model**

The semi-empirical PMP equation used here to predict the pressure drops was derived by Cahela et al. The equation and the various parameters used in it are discussed in detail in Section VI.4. Using this equation pressure drops were predicted for all the different microfibrinous media shown in Table 4.1 over the range of velocities used in this experiment.

#### **IV.4. Results and Discussion**

The experimental results of the pressure drop tests and the pressure drops estimated from PMP equation for corresponding media are shown in Fig.4.2. The symbols represent the experimental values and the solid lines represent the corresponding PMP equation predictions. The results show a good agreement between the results of the PMP equation and the experimental results. The average (absolute) error in using PMP equation to predict pressure drops in microfibrinous media was found to be 3.44% and the maximum (absolute) error for these conditions and samples was 9.13%. As expected the pressure drop increased with decreasing particle and/or fiber diameter and decreasing voidage.



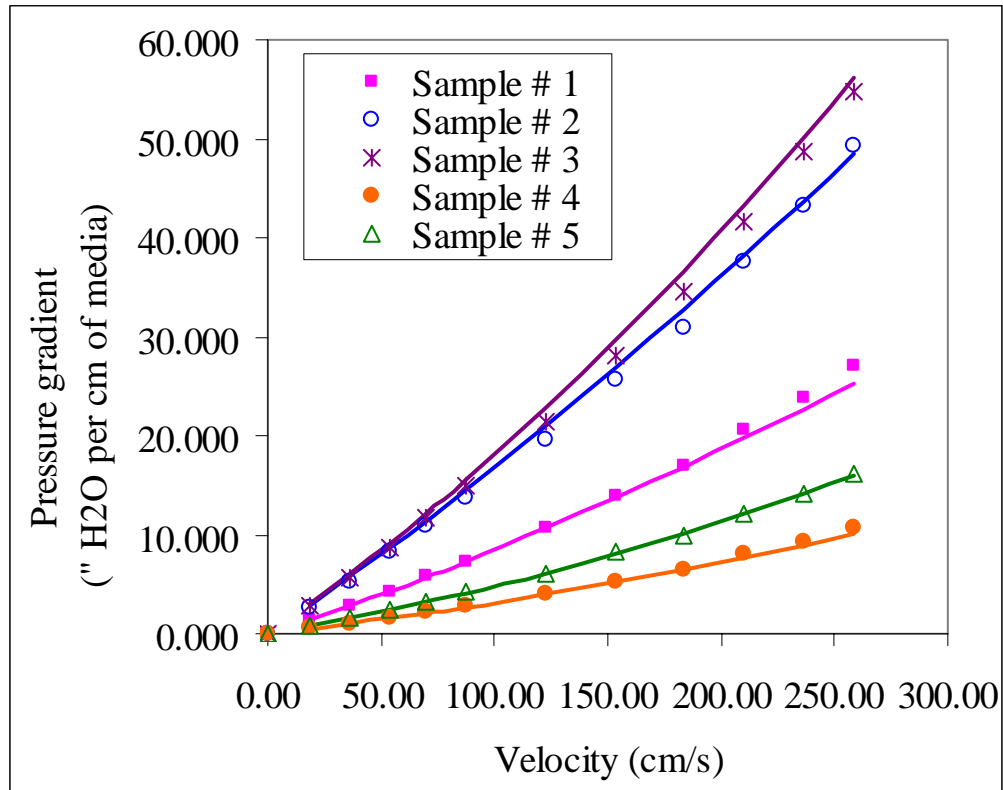


**Figure 4.2 Pressure drop results of microfibrous media samples. (The symbols represent the experimental values and the solid lines represent the corresponding PMP equation predictions.)**

#### IV.4. Conclusions

PMP equation was successfully used to predict the pressure drops in microfibrous media with in reasonable error limit. Hence, this can be a very useful tool in estimating the pressure drops in microfibrous materials.

## **CHAPTER V**

### **CATALYTIC OZONE DECOMPOSITION**

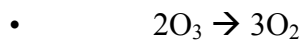
#### **V.1. Introduction**

In this study catalytic ozone decomposition for air craft cabin air purification was used as a model system to demonstrate and understand the anomalous heterogeneous contacting efficiency of Microfibrous Entrapped Catalysts (MFEC). A comparison of the contacting efficiency of MFEC was made with various conventional heterogeneous contacting systems – monoliths and packed beds. Monoliths are used in most of the commercial aircraft ozone converter systems [5.1] owing to their lower pressure drops. Pleated microfibrous systems were known to reduce the pressure drops dramatically and hence they were used in an attempt to create a more efficient system for air purification.

Theoretical comparisons of packed beds of various particle sizes, Monoliths of various cpsi and MFEC with various pleat factors were made to see the effect of various reactor geometries on the efficiency of the conversion process. A performance evaluation criterion was defined basing on the mass and flow efficiency of the system and it was used to judge the efficiency of the various systems. The effectiveness of each of the reactor systems in removing ozone is studied. This application involves rather high flow rates and is quite demanding in terms of pressure drop. The surface reaction rates involved were also high in order to achieve high throughput processing. As the surface reaction rates were high all the reaction systems considered were in transport controlled

regime – inter-phase and/or intra-particle. Also the upper bound of the performance of any reactor, basing on the performance evaluation criterion used in this study, lies in the inter-phase transport controlled regime. This is because for a given reactor dimensions and inlet conditions the external mass transfer controlled regime represents the highest achievable reaction rates in a reactor, and hence is the measure of true reactor performance. This has also been noted by other authors [5.15] and will be discussed further in the following sections.

Experimental comparisons were also made between monoliths and microfibrinous media. The results from the experiments agreed very well with the theoretically obtained results. The reaction involved is:



Ozone is identified as a key air pollutant at air craft cruising altitudes [5.1, 5.2]. At altitudes of 50000ft above sea level, the ozone concentrations as high as 6.0 ppmv and above can be found in the atmosphere [5.1]. The Environmental Protection Agency (EPA) standards for ozone exposure limits are a time weighted average of 0.08ppmv for an 8 hr period and 0.12 ppmv for a 1 hr period [5.3]. Exposure to higher concentrations of ozone can cause severe irritation of eyes, nose and throat and several other respiratory illnesses [5.5]. Torres et al. [5.5] give a detail account about the health hazards relating to ozone exposure. Apart from the natural occurring ozone at high altitudes, copiers, printers, plasma generators and also many other industrial equipment produce ozone in ppm levels. Some of these equipment have inbuilt ozone destruction units. Ozone is also used in most of the municipal water purification processes and also used in widely in the

food industry as a disinfectant [5.6]. The excess unreacted ozone can become a potential pollutant.

A detailed account of various catalysts used in the ozone decomposition reaction, their activities and rate mechanisms is given by B. Dhandapani and S.T. Oyama [5.7, 5.9]. The theoretical computational chemistry based calculations along with experimental results of the kinetics of metal oxide catalysis of ozone are presented in detail by elsewhere [5.8]. Development of better or improved catalysts for boosting the surface reaction rates was beyond the scope of this work and no effort was made in that direction. In this research a precious metal (PM) supported on  $\gamma$ -Alumina was used as the catalyst, in the comparisons sought among MFEC and commercial monolith converter.

#### **IV. 2. Mathematical Models for the Different Reactor Systems**

Theoretical comparisons of MFEC with packed beds and monoliths systems have been made for a first order irreversible kinetics. The mathematical models used to analyze the performance of various reactor systems are based on the steady state material balances, transport rates of reactant in the gas phase and inside the catalyst (support) particles and the surface reaction rates. The concentrations of ozone that needs to be treated are about a couple of ppm, this concentrations need to be brought down to values less than 0.08 ppmv. Although the ozone catalytic decomposition is an exothermic reaction, due to the extremely low concentrations present there is no appreciable adiabatic temperature rise involved. Hence isothermal conditions are used. The reactor  $Pe(=u_0.L/D_M)$  numbers are sufficiently high owing to the high velocities under consideration, hence plug flow conditions are assumed for all the reactors. The significance of flow maldistributions in

packed beds with small diameter particles has been shown in the earlier sections but they were not included in the calculations and instead ideal conditions were employed as the comparisons of MFEC was sought with best possible efficiencies of packed beds. Pressure variations along the reactor length are also neglected in the theoretical comparisons. The entrance and exit (pressure) losses can be quite significant in some cases depending on the velocities, bed voidages and the exact design of the reactors. In this theoretical part of the study, these losses in all the reactors were also neglected in view of keeping the results independent of the reactor length. If included they could affect some of the results obtained in this work, but in authors' view the trends shown would not be altered significantly. The operating conditions and various parameters used in these comparisons are shown in Table 5.1.

**Table 5.1. Conditions and parameters used in the model.**

Temperature (K)	393
Pressure (pa)	$1.013 \times 10^5$
Inlet Ozone Concentration (ppmv)	1.5
<i>Parameters</i>	
$D_m$ (m <sup>2</sup> s <sup>-1</sup> )	$2.91 \times 10^{-5}$
$D_e$ (m <sup>2</sup> s <sup>-1</sup> )	$8.27 \times 10^{-6}$
$\mu$ (kg/m.s)	$2.287 \times 10^{-5}$
$k_o$ (l/s)	$1.769 \times 10^8$
$E_A$ (kJ/mol)	21.05

### V.2.1. Packed Beds

The various particle diameters of packed beds compared in this study along with bed properties are used listed in Table.5.2. The range of particle sizes used will be justified in the results section as the performance optimum for packed beds for the conditions of the study lied with in this range.

**Table 5.2. Packed bed particle diameters and bed properties used in the theoretical comparisons**

Particle Diameters, $d_p$ (mm)	0.17, 0.3, 0.5, 0.75, 2.0
Sphericity( $\phi$ )	0.7
Void Vol. %	40
Catalyst Vol. %	60

For packed beds Ergun equation was used to predict the pressure drop.

$$\Delta P = \left( 150 \frac{(1 - \varepsilon_b)^2}{\varepsilon_b^3} + 1.75 \text{Re}_p \frac{(1 - \varepsilon_b)}{\varepsilon_b^3} \right) \times \rho v_0^2 \times \left( \frac{L}{\phi dp} \right) \quad (5.1)$$

The gas phase mass transfer coefficients for packed beds were obtained using Thoenes-Kramers correlation. It is a semi-empirical equation widely used for predicting the mass transfer coefficients in packed beds [2.6].

$$Sh = \text{Re}_p^{0.5} Sc^{0.33} \frac{(1 - \varepsilon_b)^{0.5}}{\varepsilon_b} \quad (5.2)$$

And the intra-particle transport rates in packed beds were modeled using [5.16] following effectiveness factor equations

$$\eta = \frac{1}{\Phi} (\coth(3\Phi) - 1/3\Phi) \quad (5.3)$$

$$\text{where } \Phi = \left(\frac{\varphi dp}{6}\right) \sqrt{k_r / D_e} \quad (5.5)$$

The effective diffusivity  $D_e$  of the reactants inside the catalyst support for all the reactor systems was obtained using equation (5.3)

$$D_e = D_m \frac{\varepsilon_p}{\tau_p} \quad (5.5)$$

### V.2.2 Monoliths

The various monolith cases compared in this study along with their structural properties used are listed in Table.5.3. These values of wall thicknesses and cell densities have been used as they are the commercially available ceramic monolith variations [5.11, 5.12]. The catalyst washcoat thickness in monoliths is generally kept to a minimum to avoid the pore diffusional resistances; this will be further justified by the effectiveness factor calculations. In typical commercial monoliths it is about 20 $\mu$ m and 60 $\mu$ m on the wall surfaces and the corners respectively [5.1]. Due to the accumulation of wash coat near the corners in the channels the effective catalyst wash coat thickness is greater than 20  $\mu$ m. So a more realistic value of 25 $\mu$ m was used in this study. A whole range of other variations of cpsi, wall thicknesses, and washcoat thicknesses could be considered (even though not all are practical combinations) but the study here was aimed at comparing MFEC with the commercially available monolith variations, assuming their dimensions are optimized from a practical stand point. Only square channel monoliths were considered here; any other channel shape is expected to more or less follow the trends obtained in this study.

**Table 5.3. Properties of various monoliths used in the theoretical comparisons**

Monolith Specs	100	200	500	500	900
Cells per square inch (cpsi)					
Wall Thickness, $t_w$ (0.001 in/ $\mu\text{m}$ )	15/381	10.5/267	6.5/152	5.5/102	2/51
Catalyst Washcoat Thickness ( $\mu\text{m}$ )	25	25	25	25	25
Hydraulic Channel Dia. (mm)	2.109	1.579	1.068	1.118	0.755
Void Vol. %	68.95	67.82	70.67	77.5	77.56
Catalyst Vol. %	3.31	5.66	6.77	7.09	10.75
Length (m)	25.5	25.5	25.5	25.5	25.5

For estimating pressure drops in monoliths Darcy-Weisbach equation for flow in straight channels was used along with the following friction factor correlations [5.1].

$$\Delta P = \frac{4f}{\varepsilon^2} \times \left( \frac{\rho v_0^2}{2} \right) \times \left( \frac{L}{d_{ch}} \right) \quad (5.6)$$

$$\begin{aligned} \text{Where} \quad f &= \frac{13}{\text{Re}_{ch}} \quad \text{if } \text{Re}_{ch} < 1000 \\ &= \frac{0.03}{\text{Re}_{ch}^{0.12}} \quad \text{if } \text{Re}_{ch} > 1000 \end{aligned} \quad (5.7)$$

For monoliths there are many empirical correlations and theoretical equations available in literature [5.13-5.15] for predicting the fluid-phase mass transfer coefficients. In this study the correlation proposed by Tronconi and Forzartti [5.13] for the mass transfer in square channel monoliths was employed.

$$Sh = 2.967 + 8.827 \times \left( \frac{1000}{G_z} \right)^{-0.545} \exp \left( \frac{-48.2}{G_z} \right) \quad (5.8)$$



The internal effectiveness factors for monoliths have been calculated using the following equation:

$$\eta = \frac{\tanh(\Phi)}{\Phi} \quad (5.9)$$

$$\text{where } \Phi = t_c \sqrt{k_r / D_e} \quad (5.10)$$

### V.2.3 MFEC

The MFEC structures with various pleat factors that are compared in this study along with bed properties are used listed in Table.5.4. These values of bed properties match those of the MFEC structure that was experimentally tested and will be described in the next section.

**Table 5.4 MFEC cases and bed properties used in the theoretical and experimental comparisons**

Pleat factors	1, 2, 3, 4, 5
Particle Diameters, $d_p$ ( $\mu\text{m}$ )	0.17
Fiber diameter ( $\mu\text{m}$ )	1:1 ratio of 8 and 12
Sphericity( $\phi$ )	0.7
Catalyst Vol. %	13.6
Metal Vol. %	1.2
Void Vol. %	85.2

Pleat factor (PF) a term which will be frequently used with regards to MFEC in this study is defined as follows:

$$\text{PF} = (\text{Total Face Area of MFEC media}) / (\text{Cross Section Area of package}) \quad (5.11)$$

For pressure drop in MFEC systems the porous-media permeability (PMP) equation proposed by Harris et al. [5.17] was used. This equation can be used to predict the pressure drops in multi-particulate beds with any voidage and its applicability for MFEC structures has been verified by the authors [5.18].

$$\Delta P = \left\{ 144 \frac{\tau^2}{\cos^2(\theta)} \frac{(1-\varepsilon_b)^2 \phi d_p}{\text{Re}_p \varepsilon_b^3} \left[ \left( \sum \frac{x_i}{\phi_i d_i} \right)^2 + x_{FD} \sum \frac{x_i}{(\phi_i d_i)^2} \right] + 6 \frac{\tau^3}{\cos^3(\theta)} \frac{(1-\varepsilon_b) \phi d_p}{\varepsilon_b^3} \left[ C_f + C_{FD} \frac{\varepsilon_b}{4} \right] \sum \frac{x_i}{\phi_i d_i} \right\} \times \left( \frac{\rho v_0^2}{2} \right) \times \left( \frac{L}{\phi d_p} \right) \quad (5.12)$$

To predict the gas-phase mass transfer coefficients in MFEC Pfeffer's theoretical model [5.19] was used.

$$Sh = \frac{1.25(1-\gamma)^{(1/5)} Pe^{(1/3)}}{W} \quad (5.13)$$

where,

$$W = 2 - 3\gamma + 3\gamma^5 - 2\gamma^6 \quad (5.15)$$

$$\gamma = (1 - \varepsilon)^{(1/3)} \quad (5.15)$$

Thoenes-Kramers semi-empirical correlation could not be used for MFEC as it has no voidage dependence to predict the mass transfer coefficients for higher voidage beds. Pfeffer's model on the other hand can account for the bed-voidage variation, which is critical for the MFEC calculations. This theoretical model has been specifically derived for low Re (<70) or laminar flow cases and its applicability in low Re range has been verified. The Re for the most of the MFEC cases in this study was less than 70, with a few exceptions in which it was only slightly higher. In this study, for simplicity of

calculations the presence of fibers was neglected in the mass transfer estimations for MFEC (except for the bed voidage calculations). And the particle effectiveness factors for MFEC have been calculated similar to that of the packed beds.

### **V.2.5 Surface reaction rate**

The parameters for the Arrhenius rate equation were estimated from the experimental results presented in the next section. And these values, listed in Table 5.1, were used to determine the surface reaction rates.

$$k_r = k_0 \exp\left(\frac{-E_A}{RT}\right) \quad (5.16)$$

### **V.2.5. Performance Evaluation Criteria**

Even for the simplified case of an isothermal first order irreversible kinetics with no side reactions considered in this study, performance evaluation of a reactor system for a given set of inlet conditions involves multiple aspects: pressure drop (operational cost), conversion, % catalyst utilization, cost of construction, catalyst life, feasibility, etc. A comprehensive term which can collectively judge all the above aspects is difficult to define. So in this study a select few (pressure drop, conversion and catalyst utilization) were used for comparing the reactors and an approach similar to the one employed by Kołodziej and Łojewska [5.20] for evaluating the performance of short channeled structured reactors was used.

Decreasing the characteristic dimensions of any reactor increases the mass and heat transport rates which is highly favorable. But on the similar lines it gives rise to higher momentum transport rates or in other words higher pressure drop which is

undesirable. So for a given system (kinetics and reactor type) and inlet conditions there should be an optimum characteristic dimension which gives the best performance. This analogy of the transport rates also holds good while comparing one reactor to another. Hence performance comparisons of reactors were made based on overall efficiency defined as a ratio of conversion achieved (logs of reduction) to (a dimension less form of) pressure drop and also on the basis of the effective reaction rates per unit catalyst (support) volume which is a measure of catalyst utilization.

First mass efficiency represented by  $\chi_M$ , was defined as the logs of reduction achieved in a given length:

$$\chi_M = \ln\left(\frac{C_{Ai}}{C_{Ao}}\right) = k_{eff} \times \tau_{eff} = \frac{k_{eff} \times PF \times L}{v_0} \quad (3.17)$$

For packed beds and monoliths the PF is effectively 1 and for MFEC it varies with the extent of pleating.

Then, flow efficiency, which is a dimensionless form of pressure drop occurring in the reactor, was defined as follows:

$$\chi_F = \frac{\Delta P}{\rho v_0^2 / 2} = function(\varepsilon, Re, d_c, PF, geometry) \times L \quad (3.18)$$

As shown in equation (5.18) for any kind of reactor geometry the  $\chi_F$  can be represented as a function of corresponding Re, characteristic dimension  $d_c$ , PF, and bed voidage multiplied by the length of reactor.

A direct comparison of reactor geometries basing on the above defined efficiencies ( $\chi_M$ ,  $\chi_F$ ) is not fair as they are dependent on the lengths of the reactors, and between one type of reactor to an another, as can be seen from Tables 5.2-5.4, the catalyst volume loadings

vary by as much as an order of magnitude and the reactor lengths required for required conversion can vary accordingly. So, an overall contacting efficiency  $\chi$  defined as the ratio of  $\chi_M$  to  $\chi_F$  which combines both these efficiencies and is independent of reactor length and extent of conversion was used in the comparisons.

$$\chi = \frac{\chi_M}{\chi_F} = \frac{k_{eff} \times PF}{v_0 \times function(\varepsilon, Re, d_c, PF, geometry)} \quad (3.19)$$

This ratio for some cases of monoliths can vary with their lengths where mass transfer coefficients are dependent on their lengths. While this variation could affect the values of  $\chi$  for monoliths, the trends obtained in this study would not be significantly altered.

### V.3. Experimental Details

#### V.3.1 Materials and Methods

Traditional high speed and low cost paper-making technique was used to prepare microfibrinous composite materials. In this process, an aqueous suspension consisting of 8 g each of 8 and 12  $\mu\text{m}$  diameter (1:1 weight ratio) metal (SS 304) fibers, 10 g of cellulose and 35 g of  $\gamma$ -Alumina (149-177 $\mu\text{m}$ ) particles was formed by rapid stirring. The resulting suspension was then transferred into the head box of a paper making equipment (MK sheet former) and the excess water was drained to form uniform (1sq.ft) square sheets of microfibrinous entrapped alumina. These sheets were dried at 373 K for 15 minutes and subsequently oxidized in air at 673 K for 1 hour to remove cellulose, before being sintered at 1323 K for 30 min in  $\text{H}_2$ . The properties of the resulting MFEC structure are as mentioned in Table 5.4. The  $\gamma$ -Alumina particles in MFEC were then impregnated using incipient wetness technique. Finally, the impregnated MFEC samples were dried

(373 K) and calcined (723K). MFEC sheets with 10% PM/ $\gamma$ -Al<sub>2</sub>O<sub>3</sub> were thus prepared. These sheets were then cut to required shapes and later used in constructing pleated structures as shown in Fig. 5.1. The cylindrical jig shown in Fig. 5.1 represents the final form of MFEC ozone converter. This unit was about 16 cm in diameter and 35 cm in length.

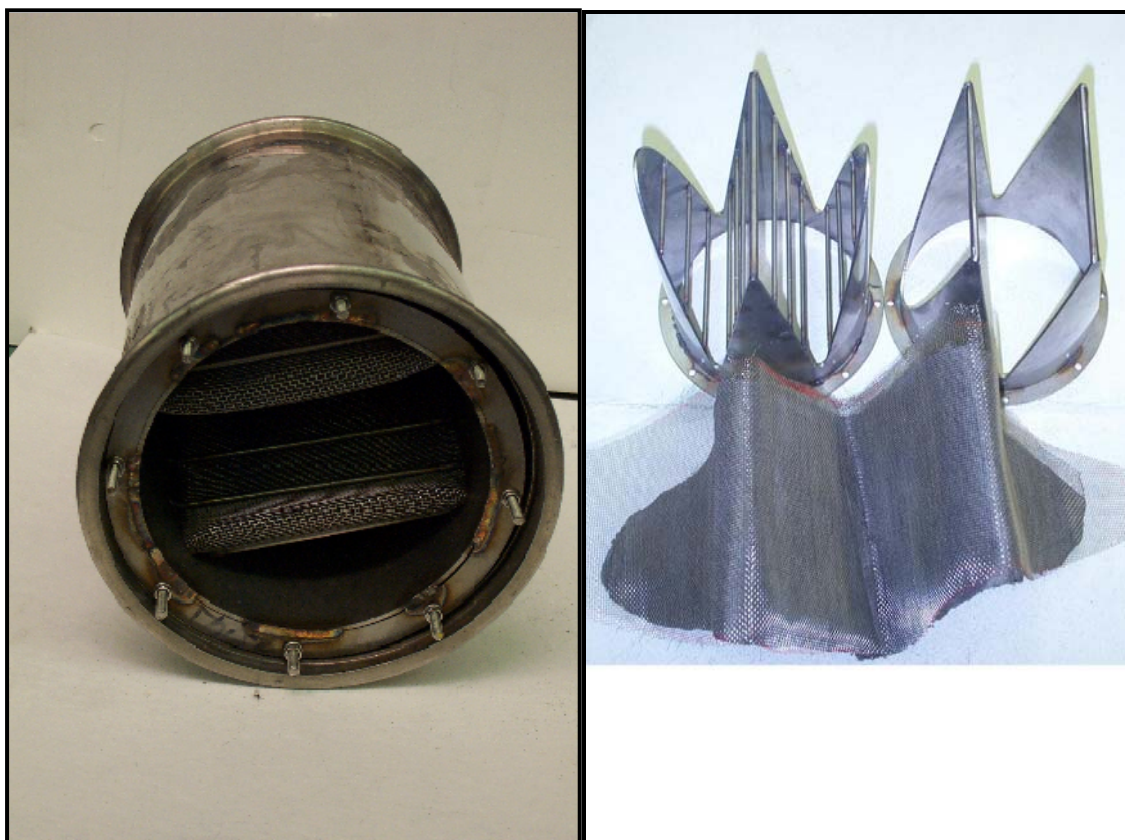




**Fig 5.1 MFEC ozone converter design with  $PF = 4.0$**

### **V.3.2 Commercial Monolith Based Catalytic Converter**

The commercial ozone catalytic converter with which the comparisons were sought in this study consisted of a 500 cpsi metal corrugated monolith. The dimensions of commercial catalytic converter are more or less the same as the MFEC structure used in this study. But the commercial  $O_3$  converter contained 120% more catalyst than the MFEC structure (with  $PF = 4$ ) used in this study.

### **V.3.3 Experimental Setup**

Experimental ozone conversion and pressure drops in the above MFEC structures of  $PF \sim 4.0$  were measured at temperatures of 394 K, 522 K and 572 K with the outlet of the reactor at atmospheric pressure. The range of mass flow rates and temperatures used in these tests include the conditions employed in commercial aircraft cabin air purification systems [5.21]. A closed loop setup was used in this process. A high pressure blower was used circulate air in the loop, with some constant purge. The power from the

blower heated the air in the closed loop, and the flow rate of the purge stream was adjusted to control the flow temperature in the loop. A variable speed drive connected to the blower was used to change the flow rates of inlet gas.

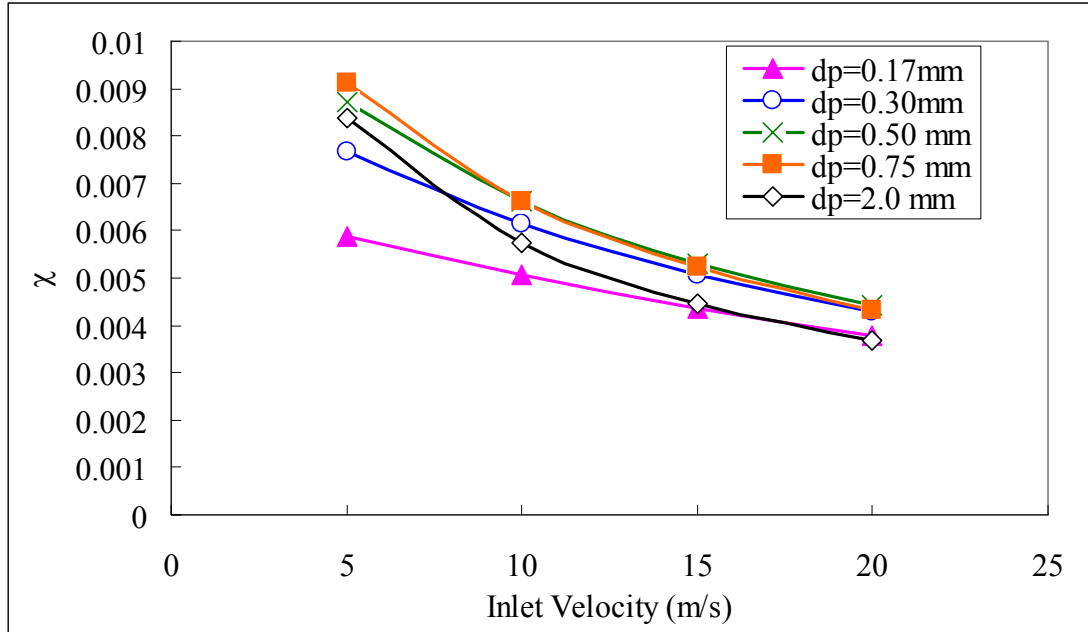
Ozone was generated from air (oxygen) using an ozone generator (PZ2-12, Prozone Corp). The generated ozone is then mixed with a bulk (fresh) air stream from a high pressure gas blower to obtain an inlet gas stream of 1.5 ppmv ozone concentration. The gas flow rates in the reactor were estimated with help of differential pressure sensors connected to a pitot tube. Ozone concentrations at inlet and outlet of the catalytic converter were measured using a UV-100 ozone analyzer (ECO SENSORS, INC). The pressure drop across the converter was also measured and recorded using differential pressure sensor. These readings were obtained for various inlet flow rates and temperatures. The data for the monoliths used in this study was obtained from the product information of commercial converters [5.21].

## **V.5. Theoretical Results and Discussion**

### **V.5.1. Comparisons among Packed Beds**

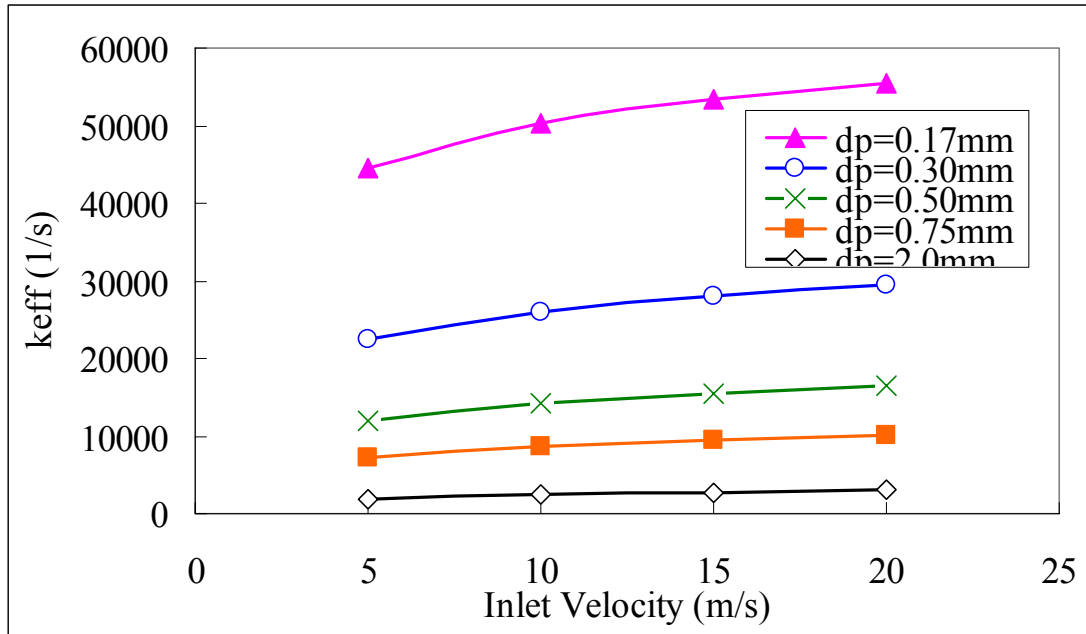
Fig 5.2 shows the overall efficiency comparisons of packed bed of various particle sizes for the conditions and kinetics mentioned in Table 5.1. The  $\chi$  values tend to increase with a decrease in particle size, reach a maxima between  $d_p = 0.5\text{mm}$  to  $0.75\text{mm}$  and then decrease with further decrease in the particle sizes.





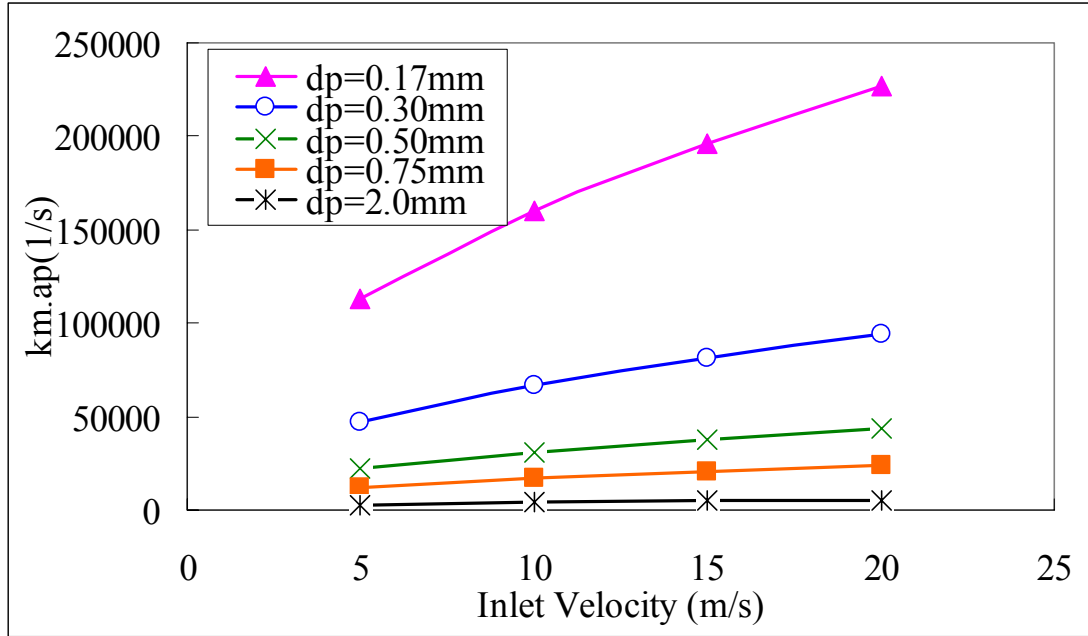
**Fig 5.2 Variation of  $\chi$  for packed beds with particle size and velocity**

Fig 5.3 shows the comparisons of the effective reaction rates per unit catalyst volume. The reaction rates continuously increase with the decrease in the particle sizes, which is a clear indication of the mass transport controlled regime. Although the variation of effective reaction rates with velocity are weak, suggests some effect of external mass transport limitations. The values of particle effectiveness factors varied from 0.26 to 0.025 for variation of  $d_p$  from 0.167mm to 2.0mm. These values suggest the severe intra-particle mass transport limitations existent in packed beds for the kinetics under consideration.



**Fig 5.3 Variation of effective reaction rate constants per unit catalyst particle volume for packed beds with particle size and velocity**

Fig.5.4 shows the variation of inter-phase mass transfer rate constants per unit particle volume for various particle diameters. These values increased with velocity and decreased with increase in particle size as expected. But comparison of these values for smaller particles with effective reaction rates in Fig 5.4 shows inter-phase mass transfer constants for smaller particle packed beds are considerably higher than the effective reaction rate constants. This further confirms that although external mass transfer rate is a controlling step in smaller particle packed beds, the internal mass transport resistances are even more significant. In larger particle packed beds intra-particle transport resistances appear to be more significant.



**Fig 5.4 Variation of inter-phase mass transport constants per unit catalyst particle volume for packed beds with particle size and velocity**

### V.5.2. Comparisons among Monoliths

Figure 5.5 shows the variation of  $\chi$  with velocity for various monolith cpsi. For the operating conditions used in this study and the length of monolith reactor considered the performance of monoliths based on  $\chi$  improved with increase in cpsi and voidages. Higher voidages were favorable as they reduce the pressure drops. The highest voidages of monoliths are constrained by other practical considerations. The internal effectiveness factor for monoliths with  $t_c=25\mu\text{m}$  was 0.22. This suggests internal mass transfer limitations. Figure 5.6 shows the variation of effective volumetric reaction rates of monoliths with velocity. The effective reaction rate constants did not vary a great deal with velocity, but there was a significant improvement in reaction rate with the increasing cpsi or decreasing channel diameters.

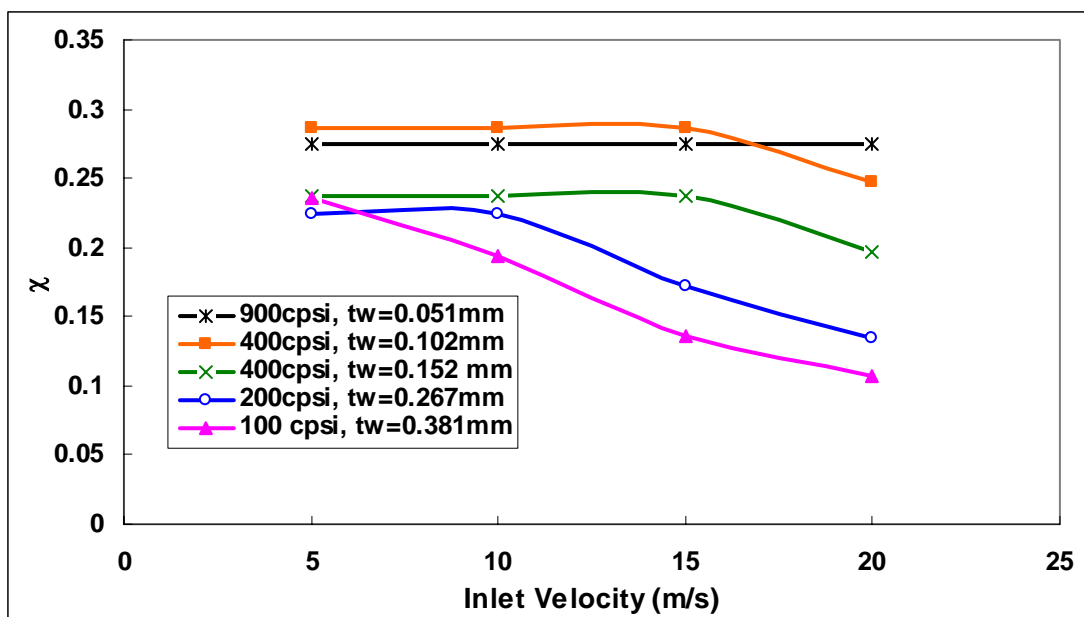


Fig 5.5 Variation of  $\chi$  for monoliths with cps and velocity

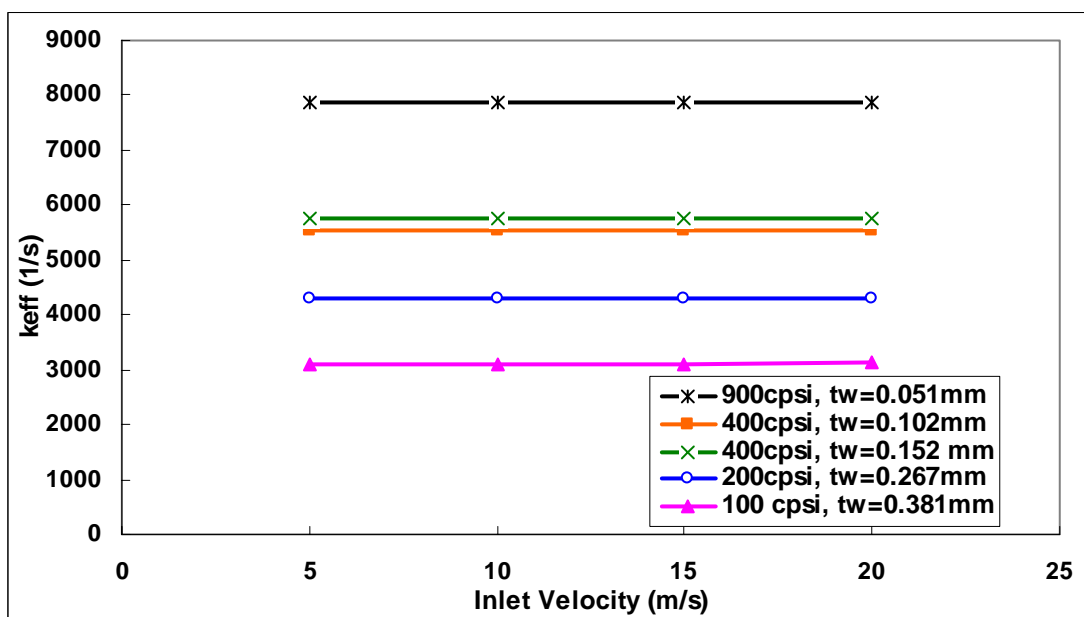
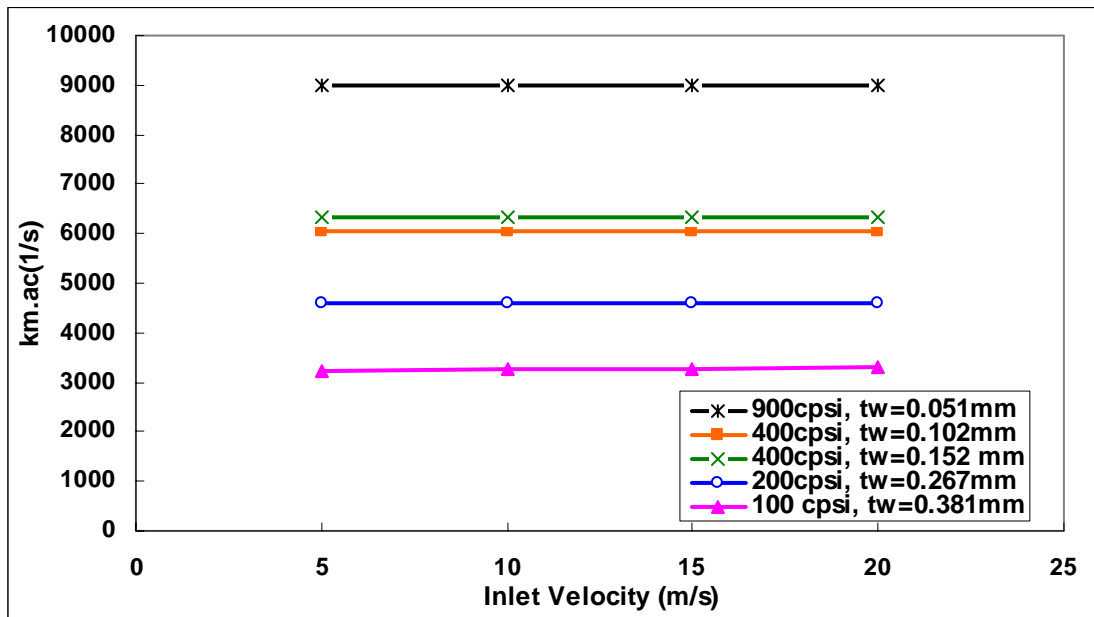


Fig 5.6 Variation of effective reaction rate constants per unit catalyst volume for monoliths with cps and velocity

Fig 5.7 shows the variation of external mass transfer rate constants with cpsi and velocity in monoliths. A closer look at the inter-phase mass transfer and the effective reaction rate constants suggests that the reaction rates in monoliths are excessively dominated by the gas-phase transport resistances. Also the gas-phase resistances in monoliths are nearly an order of magnitude smaller than the values in packed beds of smaller particle sizes. This is very much in agreement with the analogy of mass and momentum transport rates discussed earlier. The extremely low reaction rates in monoliths meant poor utilization of the catalyst.



**Fig 5.7 Variation of inter-phase transport constants per unit catalyst volume for monoliths with cpsi and velocity**

### V.5.3. Comparisons among MFEC Pleat Factors

Figure 5.8 shows the variation of  $\chi$  with velocity for MFEC systems with various pleat factors. The performance of MFEC improved dramatically with increase in PF. With increase in PF the effective velocities in MFEC was cut by factor equivalent to PF

and the hence the pressure drops were reduced drastically and also as the effective velocities reduced the residence times in the reactors increased and hence more conversion was possible. The internal effective factor for the MFEC systems was 0.256, which indicates presence of internal mass transfer limitations.

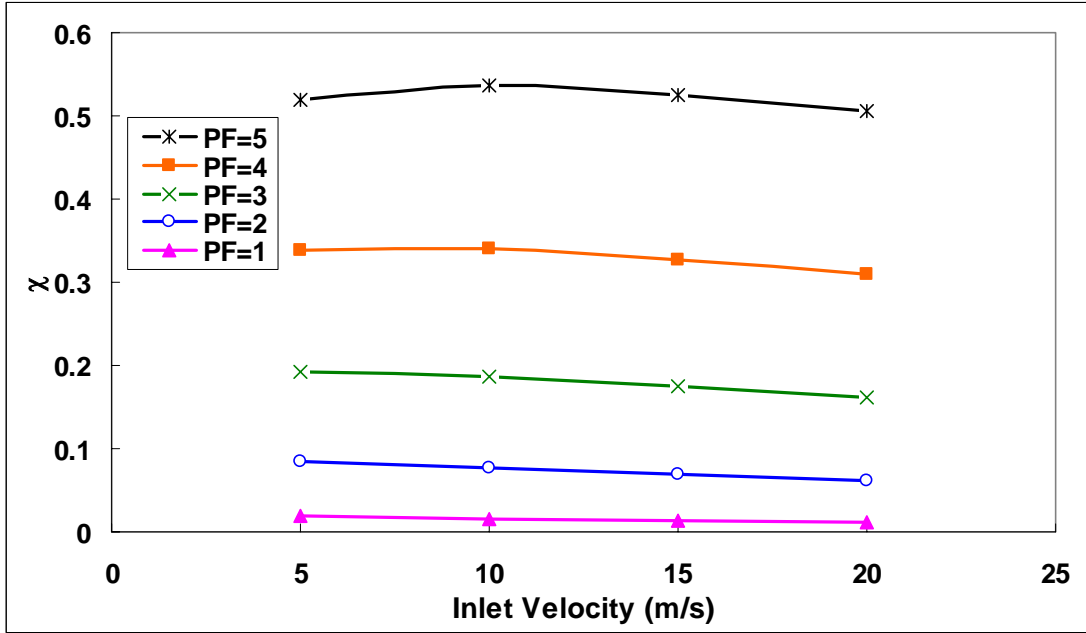


**Fig 5.8 Variation of  $\chi$  with velocity for MFEC of various PF**

Figures 5.9 and 5.10 show the variation of effective reaction rate and external mass transfer rate constants with velocity respectively, for MFEC systems of varying PF. Although all the cases of MFEC had same particle diameter and bed composition, as the effective velocity decreased with increase in pleat factors the inter-phase mass transfer coefficients decreased and hence there was decrease in effective rate constants as well. But for MFEC systems the inter-phase mass transfer constants per unit catalyst volume were far higher than that in monoliths even for the highest PF considered, which helped achieve effective rate constants. This in turn led to higher utilization of catalysts.

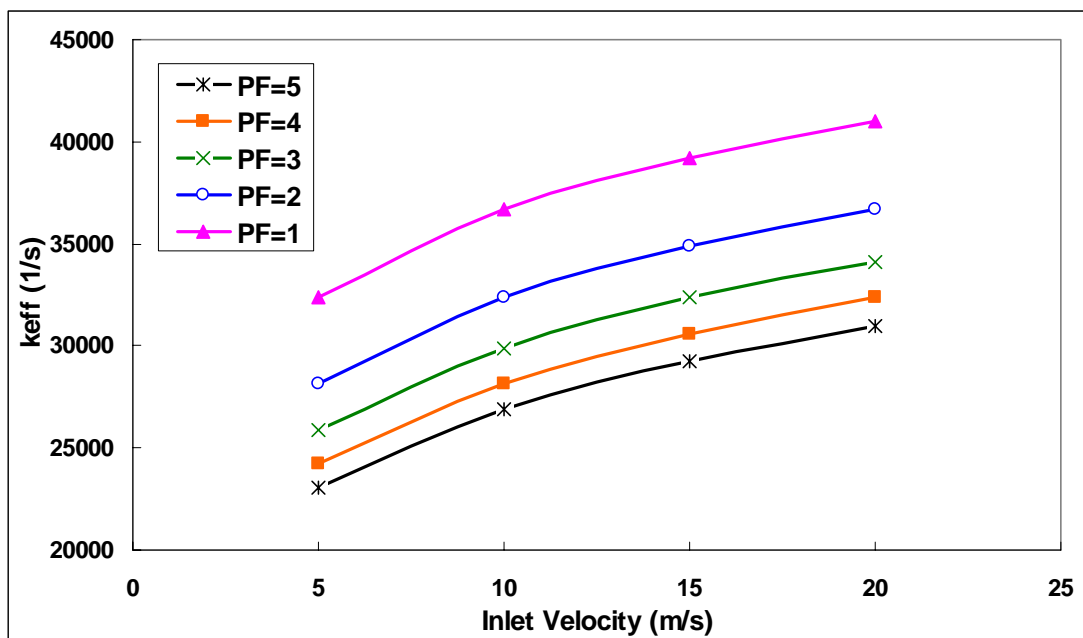


**Fig 5.9** Variation of effective reaction rate constants per unit catalyst volume with velocity, for MFEC of various PF.

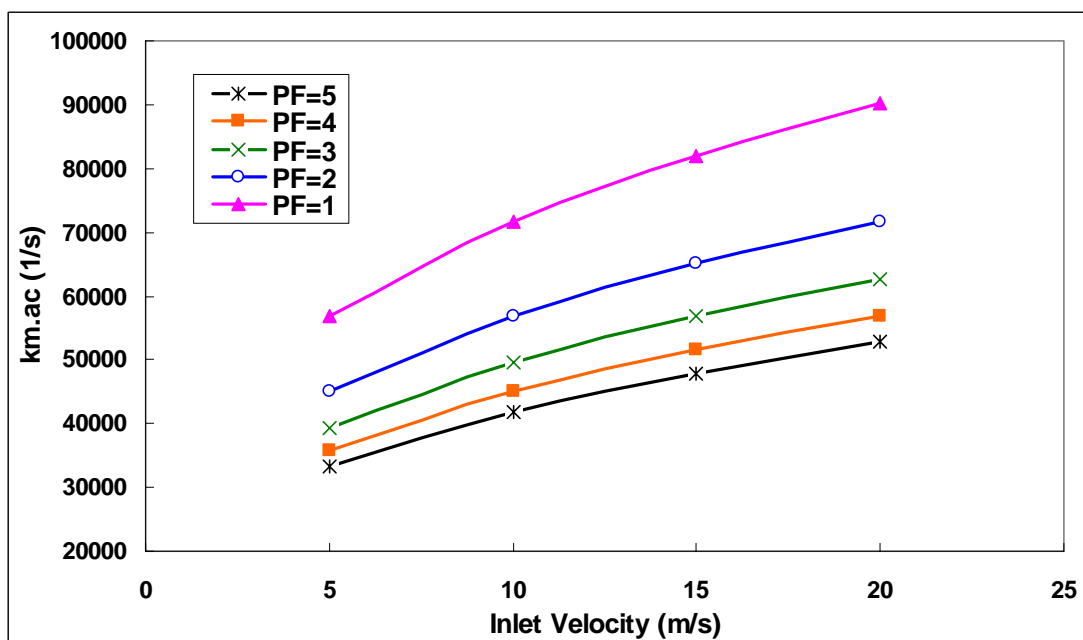


**Fig 5.10** Variation of effective reaction rate constants per unit catalyst volume for with velocity MFEC of various PF

### V.5.5. Comparisons among Different Reactor Types

Figure 5.11 compares the overall efficiencies of packed beds, monolith and MFEC systems. The cases with highest and lowest overall efficiencies of packed bed and monoliths obtained in the plots before are shown in this figure. Clearly the overall efficiency of packed beds and MFEC with PF=1 were lower than the packed beds. But the efficiency of MFEC systems which improved dramatically with increase in PF surpassed the performance of monoliths.

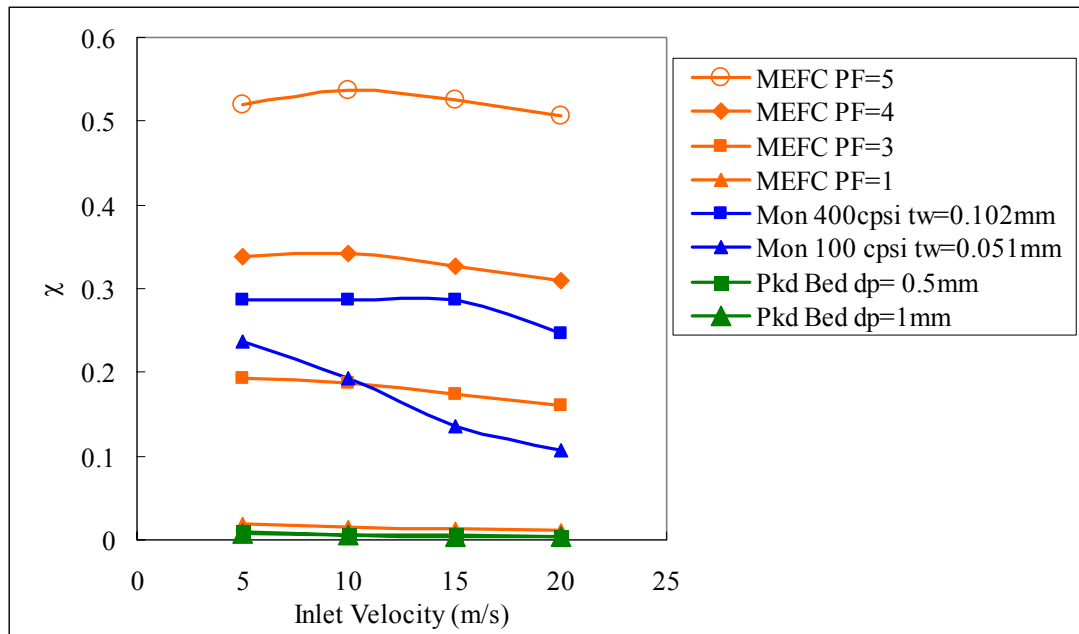


**Fig 5.11 Variation of  $\chi$  for various reactor geometries with velocity**

The construction and operation of some of the packed bed reactor cases considered in here like the beds with smaller particles, even if efficient, may not be feasible for practical applications with the kind of operating conditions (velocities used and mobile settings) and surface reaction rates and practical conversions targeted. As this would require construction of a packed bed of thickness less than 0.5cm which could achieve 99% conversion and but still fail as they produce unreasonably high pressure



drops. But those cases were also studied to make this theoretical study more comprehensive.

Although the results shown in the above plots change with the surface reaction rates, the trends in the comparisons of pleated MFEC structures with monoliths shown here were observed to be more or less the similar for any higher surface reaction rate and also for surface reaction rates up to two orders of magnitude lower. The optimum in the packed bed diameters shifts to a higher particle diameter at lower surface reaction rates. And for lower surface reaction rates slightly higher pleating in MFEC is needed to surpass the performance of monoliths, with the particle diameters and bed composition considered here. If the surface reaction rates were to be decreased the effective reaction rates and hence the overall efficiency decrease for all the reactors. As the effective reaction rates decrease with decreasing surface rate constants the effective utilization of the catalysts is decreased. Hence as mentioned earlier the upper bound of the performance of any reactor lies in the external mass transfer regime. So the overall efficiencies of monoliths used in these comparisons are closer to their upper limit for the operating conditions and reactant composition used. But the overall efficiencies of MFEC and packed beds shown are not the upper bounds for any of the pleat factors studied and could be further improved with higher surface reactivity.

MFEC with even higher pleating can be made but with the increase in pleating inertial losses in the entrance and exit of the structures can become significant. The extent of inertial losses also depends on the size constraints of the reactor. The bed composition of MFEC used in these comparisons is also not the optimum for this surface kinetics or any other conditions. As the bed properties (voidages, catalyst loading, particle and fiber

diameters) of microfibrinous materials can be easily tailored to the requirements of the applications, more focus is being laid on it. With use of bigger particles fiber diameters and more void fractions in MFEC the pressure drop can be further reduced.

## V.5. Experimental Comparisons of Monoliths and MFEC

The ozone conversion and pressure drop comparisons of MFEC at PF=4.0 and commercial monolith converter are shown in Figure 5.12 and 5.13 respectively. MFEC converter with MFEC PF=4 conversion surpassed the conversion of commercial converter with 2.2 times more catalyst. The experimental conversions and pressure drops were in line with the theoretical results. The conversions of MFEC with PF=4 was slightly above the conversion of monoliths. The pressure drop in the MFEC system was almost equivalent to that of the commercial monolith systems. This also shows that the MFEC has higher catalyst utilizations compared to the monoliths.

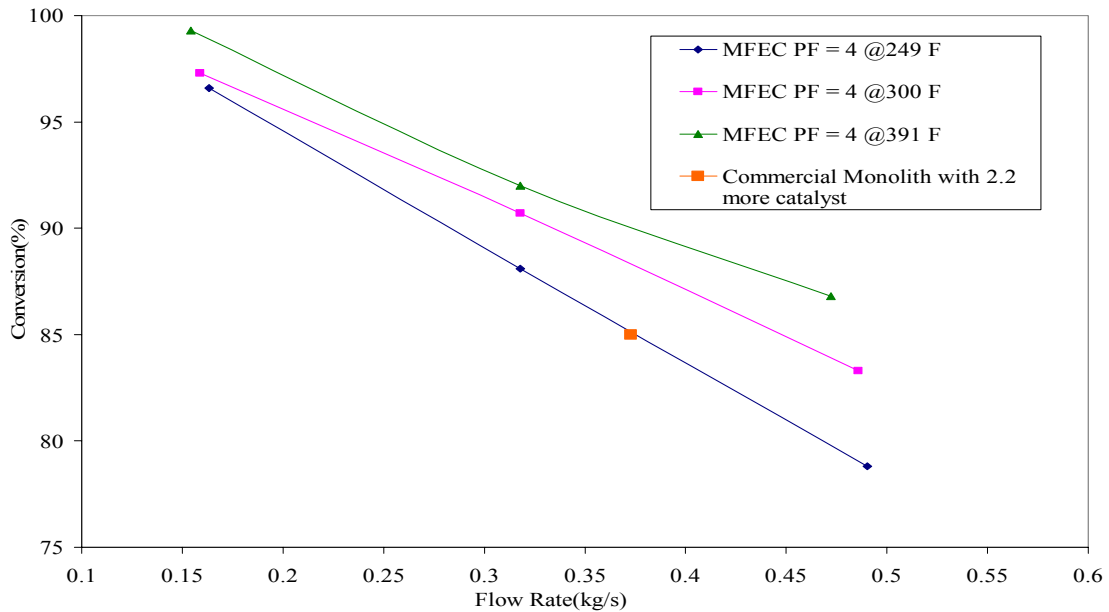


**Fig 5.12 Experimental conversion comparisons of commercial monoliths converters with MFEC of PF=4.0**

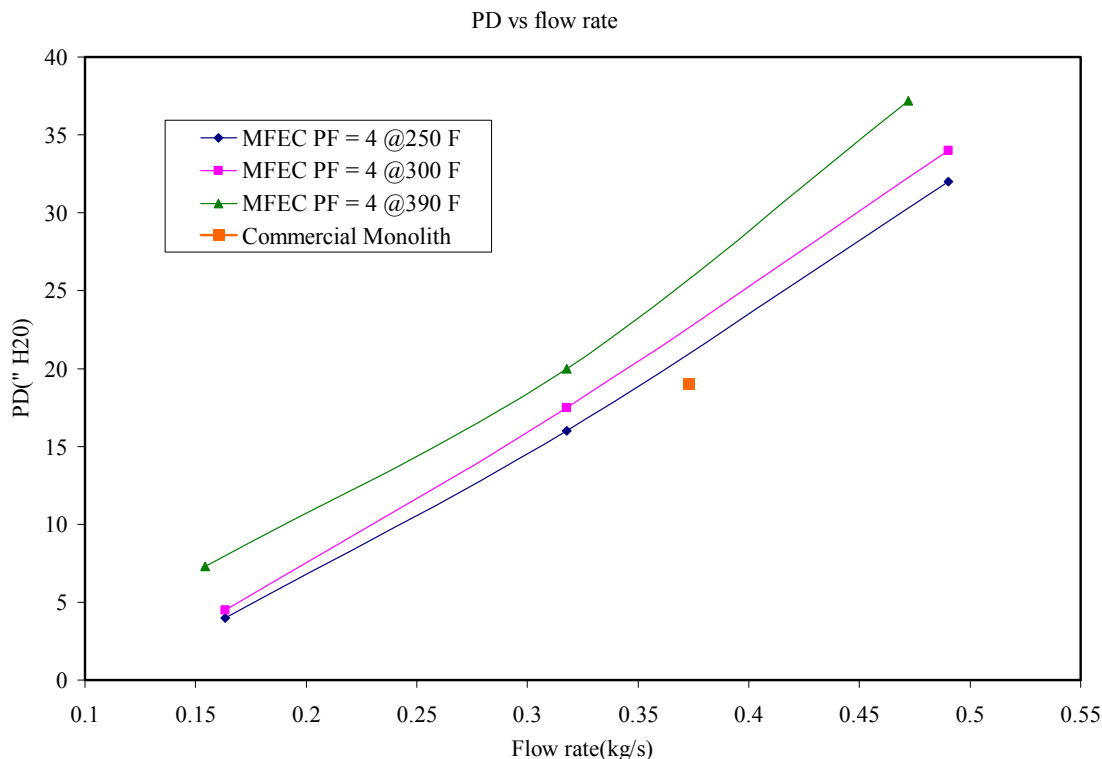


**Fig 5.13 Experimental pressure drop comparisons of commercial monoliths converters with MFEC of PF=4.0**

## V. 6. Conclusions

For the operating conditions and reaction kinetics used in this study the overall contacting efficiencies of packed beds, irrespective of the particle sizes used, were lower than that of the monoliths. While the bigger particle packed beds offered less resistance to flow they were mainly constrained by the (interphase and interparticle) mass transport resistances. The smaller particle beds, on the other hand, had high mass transfer rates but the associated pressure drops in the fluid flowing through them were also high. This made the packed beds a very inefficient form of contacting. Monoliths offer low resistance to flow (or low pressure drop) due to straight channels and also low

intraparticle transport resistances due to thin catalyst coatings. Hence they have higher overall efficiencies compared to packed beds and MFEC with low PF. The limitation in monoliths mainly comes in the form of lower interphase mass transfer coefficients compared to packed beds and MFEC.

Although the overall contacting efficiency of MFEC with lower PF was less than that of the monoliths, it improved drastically with increase in PF. This increase in  $\chi$  in MFEC is a direct result of a proportionate decrease in effective velocity associated with increase in PF. The decreased effective velocity results in lower pressure drops and also higher residence times or, in other words, higher conversion. This dual advantage achieved with pleating MFEC media leads to higher  $\chi$  values in MFEC compared to that of monoliths. Also as the effective reaction rates in MFEC were higher than that of the monoliths, MFEC structures are more optimized compared to monoliths in terms of catalyst utilization. While small particles used in MFEC lead to high interphase and intraparticle transport rates, high voidages and ease of pleating resulted in low pressure drops.

Experimental results of ozone conversion and pressure drop measurements further confirmed the above theoretical analysis. Experimental conversion and pressure drop measurements of a MFEC structure with PF=4.0 almost equal to that of a commercial monolithic converter. But the amount of catalyst used in monolith converter was 2.2 times more than that in the MFEC design. These results were in good agreement with theoretical calculations. While monoliths are widely believed to be the most efficient contacting systems, the theoretical and the experimental results in this study showed that the MFEC have greater contacting efficiencies and hence are ideal for high throughput

applications. MFEC have demonstrated higher catalyst utilizations and better overall efficiency – lower pressure drops and higher effective reaction rates compared to the conventional reactor systems. With this proven potential further optimization of MFEC structures can be undertaken.

## VI.7. Nomenclature

$$a_p = \frac{6}{(\phi d_p)} = \text{Ext. Surf. Area per Unit Vol. of Adsorbent (1/m)}$$

$$C_D = \text{Coefficient of Drag for Sphere in Turbulent Flow} = 0.6$$

$$C_f = \text{Coefficient of Friction for Sphere in Turbulent Flow}$$

$$C_{FD} = \text{Coefficient of Form Drag for Sphere in Turbulent Flow} = C_D - C_f$$

$$D_M = \text{Molecular Diffusivity (m}^2/\text{s)}$$

$$D_e = \text{Effective Diffusivity in Pores (m}^2/\text{s)}$$

$$d_{ch} = \text{Monolith Channel Dia. (m)}$$

$$d_i = \text{diameter of the component } i$$

$$d_p = \text{Catalyst Particle Dia. (m)}$$

$$E_A = \text{Activation Energy of Reaction (KJ/mol)}$$

$$f = \text{Friction Factor}$$

$$Gz = \text{Re} \cdot \text{Sc} \cdot d_{ch} / L = \text{Graetz Number}$$

$$k_{eff} = \text{effective Reaction Rate per Unit Catalyst Volume (1/s)}$$

$k_m = \text{Ext. Mass Transfer Coeff. (m / s)}$

$k_p = \text{Int. Mass Transfer Coeff. (1 / s)}$

$k_r = \text{Surface Reaction Rate per Unit Catalyst Volume (1 / s)}$

$k_0 = \text{Pre exponential factor in Arrhenius Equation (1 / s)}$

$L = \text{Height Of Bed (m)}$

$\Delta P = \text{Pressure Drop (Pa)}$

$PF = \text{Pleat Factor}$

$Pe = \frac{d_p u_{in}}{D_M} = \text{Peclet Number}$

$Re_{ch} = \frac{d_{ch} u_{in} \rho}{\mu} = \text{Monolith Channel Reynolds Number}$

$Re_p = \frac{\phi d_p u_{in} \rho}{\mu} = \text{Reynolds Number}$

$Sc = \frac{\mu}{\rho D} = \text{Schmidt Number}$

$Sh = \frac{k_m \phi d_p}{D_M} = \text{Sherwood Number}$

$t_c = \text{Catalyst Washcoat Thickness}$

$x_i = \text{Volume fraction of the component } i$

$x_{FD} = \varepsilon_b^2 / 12(1 - \varepsilon_b)$

$\chi$  = Overall Efficiency of Reactor

$\chi$  = Overall Efficiency of Reactor

$\chi_F$  = Flow Efficiency of Reactor

$\chi_M$  = Mass Efficiency of Reactor

$\varepsilon_b$  = Bed Voidage

$\varepsilon_p$  = Particle Voidage

$\Phi$  = Thiele Modulus

$\phi$  = Sphericity of Particle

$\eta$  = Particle Effectiveness Factor

$\theta$  = Flow Path Angle

$\mu$  = Gas Viscosity

$\rho$  = Gas Density

$\tau = 1 + \frac{1}{2}(1 - \varepsilon_b) = \text{Bed Tortuosity}$

$\tau_{eff}$  = Effective Residence Time

$\tau_p$  = Tortuosity of Particle Pores

$v_0$  = Superficial Velocity

## **CHAPTER VI**

### **CFD ANALYSIS OF THE EFFECT OF FIBERS ON MASS TRANSFER RATES IN 2D CHANNEL GEOMETRIES**

#### **VI.1. Introduction**

##### **VI.1.1. Background**

Fibers are an essential part of MFECS media and their high aspect ratios play a key role in the formation of these high voidage structures. Apart from holding the catalyst/adsorbent particles in the 3D space to create the frozen-fluidized-bed-like structure of MFECS, they could potentially play a significant role in enhancing the fluid-particle interphase mass transfer rates. The fibers (although inert or non-reactive) present in MFECS can contribute to the fluid-particle interphase mass transfer rates in two ways:

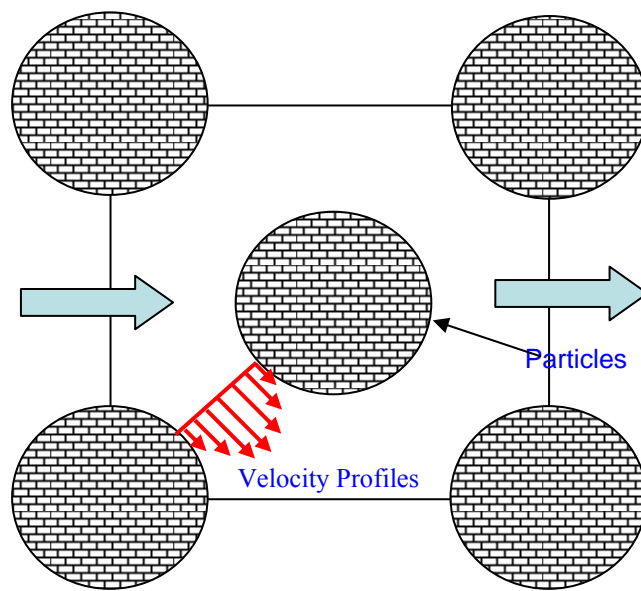
- (a) by decreasing the peaking velocities (parabolic velocity profiles) in the interstitial spaces between the particles and promoting plug flow conditions and
- (b) by acting as ‘static mixers’ and promoting radial dispersion of species.

These aspects are analyzed in this chapter by using simple 2D geometries. The commercial CFD software (Fluent) was employed to numerically solve the Navier-Stokes equations along with the species mass transport equations.

Fogler [6.1] and Levenspiel [6.2] have given a detailed account of axial dispersion effects due to parabolic velocity profiles in tubular reactors with laminar flow. In tubular



reactors with parabolic velocity profiles, the velocity at the core is about two times the average fluid velocity and the velocities near the wall are close to zero. This leads to a difference in residence times of fluid elements at various cross sections inside a reactor. These deviations from plug flow can have a significant negative effect on the reactant conversion. Similarly, the variation in local velocities in the interstitial spaces between the particles in a fixed bed can lead to significantly higher axial dispersion coefficients. This effect was included in the axial dispersion coefficient correlations developed by Edwards and Richardson [6.3]. Fibers in MFES materials are expected to reduce the velocity peaks and create a more uniform velocity profiles between the particles. A particle bed without fibers and typical velocity profile between the particles is shown in Fig 6.1(a). Fig 6.1(b) shows a particle bed with fibers (representing a MFECs bed) and along with a representative velocity profile inside the bed. The significance of this phenomenon on the mass transfer rates and/or conversions will be explored.



(a)

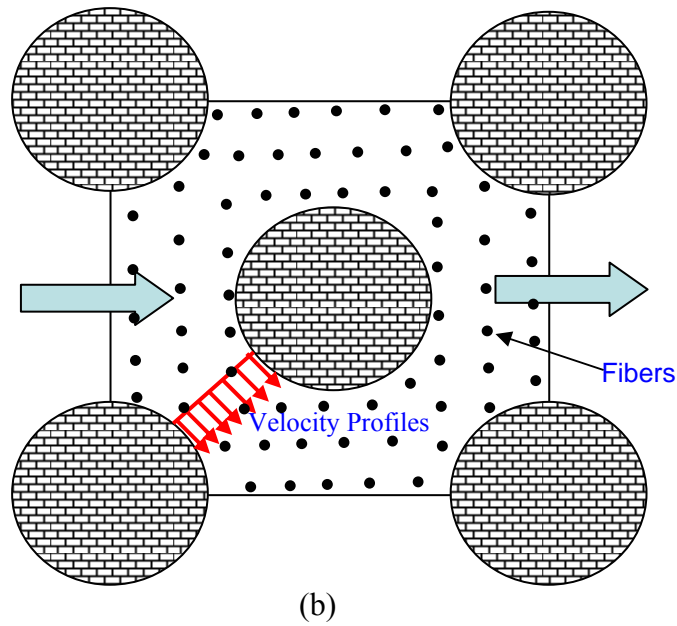


**Fig. 6.1. (a) Fixed bed of particles without fibers and (b) Fixed bed of particles with fibers**

For the fibers to produce any amount of ‘static mixing’ Re numbers based on the fiber diameters need to be sufficiently high to create vortices and/or turbulence. Fibers in MFECs media can best be approximated to cylinders. A detailed analysis of the effect of Re on the flow around a single cylinder in an infinite fluid medium is given elsewhere [6.4, 6.5]. To assist in understanding the lateral mixing effect of fibers, a brief review of the various Re regimes and the associated flow behavior around a cylinder is given here.

For a long cylinder in an infinite fluid medium, the flow is very orderly and symmetrical before and after the cylinder for  $Re \ll 1$ . Up to Re of 4 the flow remains attached to the surface, but with increase in Re the stream lines become more and more asymmetric (before and after the cylinder). At about  $Re=4$ , flow separates and a pair of vortices appear behind the cylinder. This phenomena persists up to  $Re=40$ , beyond which the vortices begin to “peel-off” from the surface and move down stream to form an

oscillatory wake known as Von-Karman vortex street. Turbulence sets in only at much higher Reynolds numbers ( $Re > 200$ ).

For the flow conditions typically used in MFECS and also for the range of flow conditions considered in this CFD study, the  $Re$  based on fiber diameter is not expected to larger than five. More over, the above analysis relates to a single isolated fiber (cylinder) in an infinite medium. For the case of flow through a matrix of fibers considered in this study, the critical  $Re$  at which the vortex formation and turbulence occur are expected to be higher than the above mentioned values. Hence there is no possibility of vortex formation or occurrence of turbulence in MFECS. This will be further confirmed with help of simple CFD simulations.

#### **VI.1.2. Overview of Approach of the Study**

Two different 2D studies were used to differentiate the possible effects of fibers:

1. Mass transfer study in straight channel geometry
2. Static mixing study in fiber matrices

In the mass transfer study the catalyst/adsorbent particle surfaces in MFECS were replaced by walls of straight channels and the effect of the inert fibers on the mass transfer rates from the bulk fluid to the channel walls was studied. Fluid-to-wall mass transfer rates with and without fibers in 2D channels were calculated for various flow conditions. The difference in the mass transfer rates between the two cases (with and without fibers) for similar flow conditions was used to analyze the effect of fibers. While the data from these simulations can be used to evaluate the effect of fibers on resulting

mass transfer rates, it can not be used to differentiate between the two possible fiber effects mentioned above.

Hence, a second (static mixing) study specifically aimed at understanding the role of fibers as static mixers was made. In this study the degree of lateral mixing (or radial dispersion) of two fluid streams was measured using the coefficient of variation (COV, defined in section VI.4). The enhancement in lateral mixing achieved when two fluid streams pass through a matrix of fibers as opposed to empty space was used to analyze the static mixing effect of fibers.

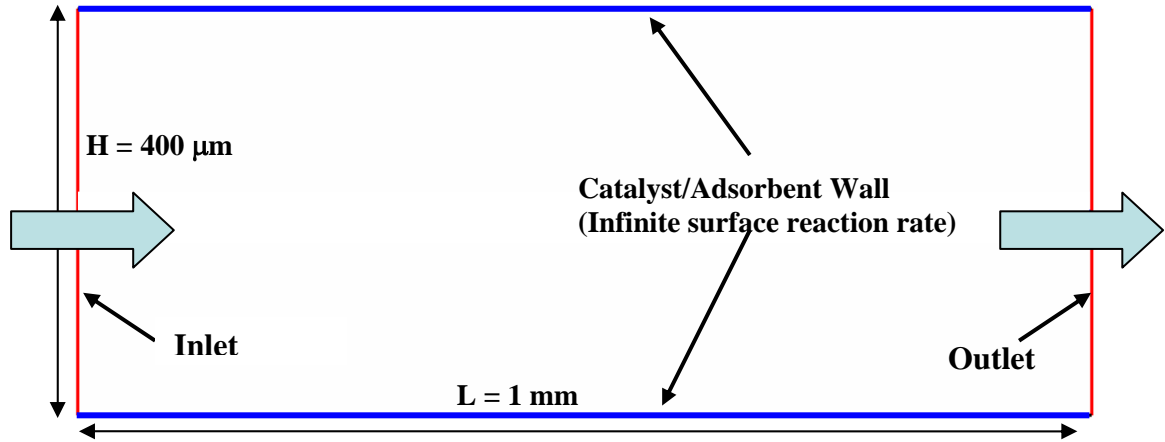
All the numerical simulations made in this work were assumed to be isothermal (because of the dilute concentrations of reactant/adsorbate) and heat transfer effects were purposefully excluded from the study. Hence, the energy equations were turned off in Fluent, i.e., the heat balance equations were not solved, in order to minimize the computation times.

## **VI.2. Geometries Used**

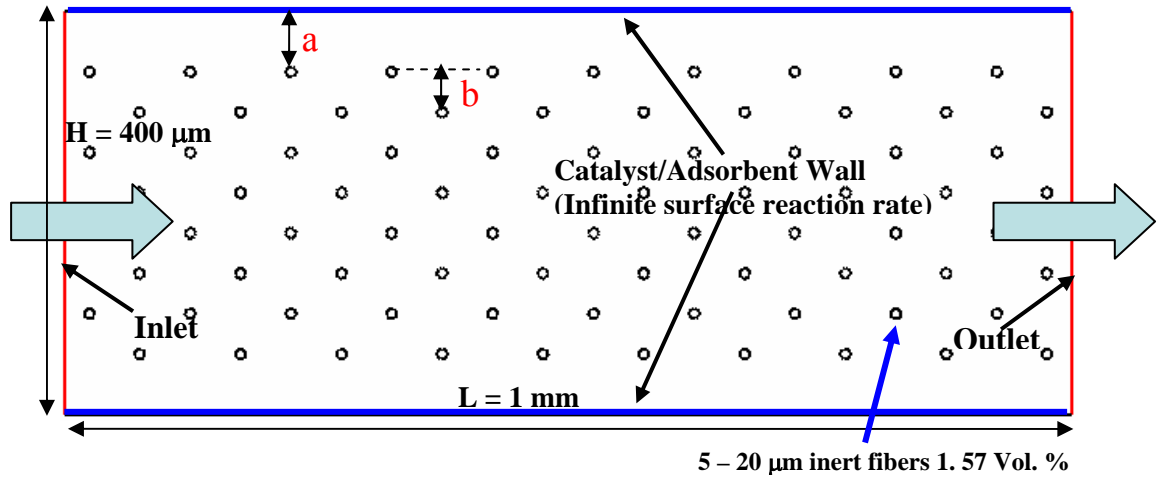
### **VI.2.1. Mass Transfer study**

In the mass transfer study, a bulk fluid stream (component B) containing a fixed concentration of a trace impurity (component A) was let into 2D channels with and without fibers. Fig 6.2 shows (a) an open channel without fibers and (b) a channel with fibers used in this study. The flow entered the channels at the left at a constant velocity and exited at the right end. The top and bottom surfaces were fixed walls with infinite reaction (or adsorption) rate. The length and the height of both the channels were fixed at 1 mm and 400  $\mu\text{m}$  respectively. Steady state outlet concentrations calculated from CFD

simulations were used to estimate conversions (log reductions) and mass transfer coefficients.



(a) Channel without fibers (Open channel)



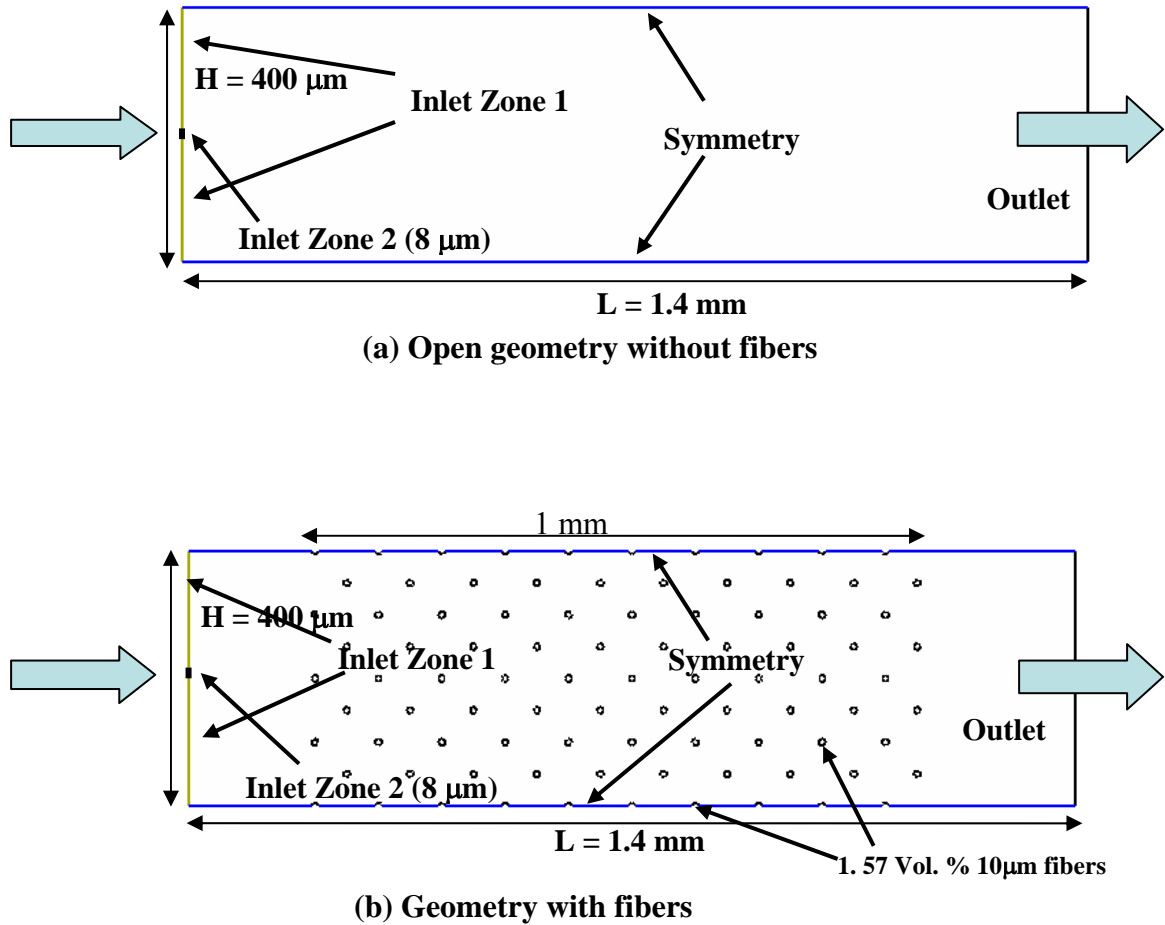
(b) Channel with fibers (Fiber channel)

Fig. 6.2. (a) and (b) Geometries used in the mass transfer study

### VI.2.2. Static Mixing Study

In this study the geometries used were somewhat similar to that used in the previous study, but the walls and the inlet faces were somewhat modified. Figs. 6.3 (a) and (b) show the geometries used in this study. The walls in the previous geometries were replaced by symmetry boundary conditions. With the walls removed the geometries represent small sections of an infinite (laterally periodic) flow field. The inlet faces in both the geometries used in this study consisted of two zones. The major part (Inlet zone 1) of the inlet had a bulk stream (pure component B, no A) flowing through it and a minor part, a small cross-section of 8  $\mu\text{m}$  height (Inlet zone 2) at the center inletting a certain concentration of component A in B. The entire inlet (both the zones) boundary was maintained at a constant velocity.

The dimensions of these geometries used were 400  $\mu\text{m}$  height and 1.4 mm in length. In the geometry with fibers, the fibers were present only in the central part of the geometry about 1mm in length. There was an inlet and exit zone of 0.2 mm length each (where there were no fibers) to allow for the velocities to stabilize. The volume loading of the fibers in the central length of 1 mm where the fibers were present was about 1.57%. The extent of mixing of the two inlet streams was measured at the exit using suitable parameters discussed in the next section to determine the static mixing effect of the fibers.



**Fig. 6.3. (a) and (b) Geometries used in the static mixing study**

### **VI.3. Design of the Study (Range of Flow Conditions and Geometry Variations)**

#### **VI.3.1. Mass Transfer Study**

To start with, the effect of fibers on mass transfer coefficients was studied for various inlet gas-phase velocities (1-100 cm/s) in relation to two specific applications - hexane removal from air @ 313 K and H<sub>2</sub>S removal from H<sub>2</sub> reformat stream @ 673 K. Table 6.1 shows the set of physical properties and flow conditions for these two processes that were used for this preliminary analysis. These two systems were chosen as they represent the extreme values for the gas phase diffusivities. The relatively high

molecular weights of hexane and air along with relatively low operating temperature result in a low mass diffusivity of hexane/air system. On the other hand, the low molecular weight of hydrogen and the high process temperature give rise to a high mass diffusivity in the  $H_2S/H_2$  system. A 1.57 % fiber volume loading, 10  $\mu m$  diameter fibers, and (a/b) ratio (Fig. 6.2 (b)) of 1.5 were used in this preliminary study.

**Table 6.1 Physical properties and operating conditions used in the preliminary mass transfer study**

Physical Property	Hexane/Air	$H_2S/H_2$
Temperature (K)	313	673
Operating Pressure (atm)	1	1
Viscosity (kg/m/s)	$1.90 \times 10^{-5}$	$1.54 \times 10^{-5}$
Diffusivity ( $m^2/s$ )	$8.41 \times 10^{-6}$	$2.95 \times 10^{-4}$
Velocity (m/s)	0.01-1	0.01-1

As the results from these preliminary studies (Section VI.5) showed some remarkable trends, a detailed dimensionless number study of the effect of fibers for a wide range of gas flow conditions and geometry variations was made. This dimensionless study was aimed at gaining a broader understanding of the individual effect of various parameters on the resulting flow patterns and the associated mass transfer rates. A comprehensive list of physical quantities influencing the fluid-wall mass transfer rate in 2D channel geometries (in Fig. 6.2) is as follows:

- Velocity ( $u_0$ )
- Viscosity ( $\mu$ )
- Density ( $\rho$ )



- Diffusivity ( $D_{AB}$ )
- Channel height ( $d_{ch}$ )
- Fiber diameter ( $d_f$ )
- Fiber volume (FV) loading percentage and
- Fiber distribution (FD) or a/b (the arrangement of fibers inside the channel)

i.e., mass transfer coefficient ( $k_m$ ) = function ( $u_0, \mu, \rho, D_{AB}, d_{ch}, d_f, FV, FD$ ) (6.1)

In this study, the analysis of the effect of fiber distribution on mass transfer rates is only restricted to the variation of a/b ratio (Fig. 6.2 (b)).

The Buckingham  $\pi$  theorem [6.6] for dimensionless analysis states that if there are  $n$  variables in a physically meaningful equation, then these variables can be reduced to a set of  $q = n - k$  dimensionless variables, where  $k$  is the number of fundamental physical quantities needed to express the  $n$  original variables. Equation 6.1 has nine dimensional variables (including  $k_m$  the dependent variable, on the left hand side), hence  $n = 9$ . All these can be expressed in terms of three (mass, length and time) fundamental physical quantities, i.e.,  $k = 3$ . Hence, the total number of dimensionless quantities needed to express the above relationship (equation 6.1) is six ( $= 9-3$ ), of which the number of independent variables will be five (one dependent variable).

The variables in equation (6.1) can be conveniently reduced into the following dimensionless quantities:

- $Re (u_0 d_{ch} \rho / \mu)$  = Inertial Forces / Viscous forces
- $Sc (\mu / \rho D_{AB})$  = Momentum diffusivity / Mass diffusivity
- $d_{ch} / d_f$  = Channel to fiber diameter ratio
- FV (Fiber volume loading )

- FD (fiber distribution inside the channel - represented by 'a/b' ratio)
- $Sh(k_m d_{ch}/D_{AB}) = \text{Convective mass transfer} / \text{Diffusive mass transfer}$

Further, equation (6.1) can be rewritten as:

$$Sh(k_m d_{ch}/D_{AB}) = \text{function}(Re, Sc, (d_{ch}/d_f), FV, (a/b)) \quad (6.2)$$

Equation (6.2) effectively reduces the total number of independent variables that needs to be studied to five from eight in equation (6.1). The choice of the range for each variable used in this study was made based on practical considerations. Fig. 6.4 represents the Re and Sc ranges for various gas and liquid phase applications based on literature [6.7] (shaded areas). Also, marked using solid lines are some typical Re-Sc ranges for applications in which MFECS were successfully tried in the past [6.8, 6.9, chapter II and V].

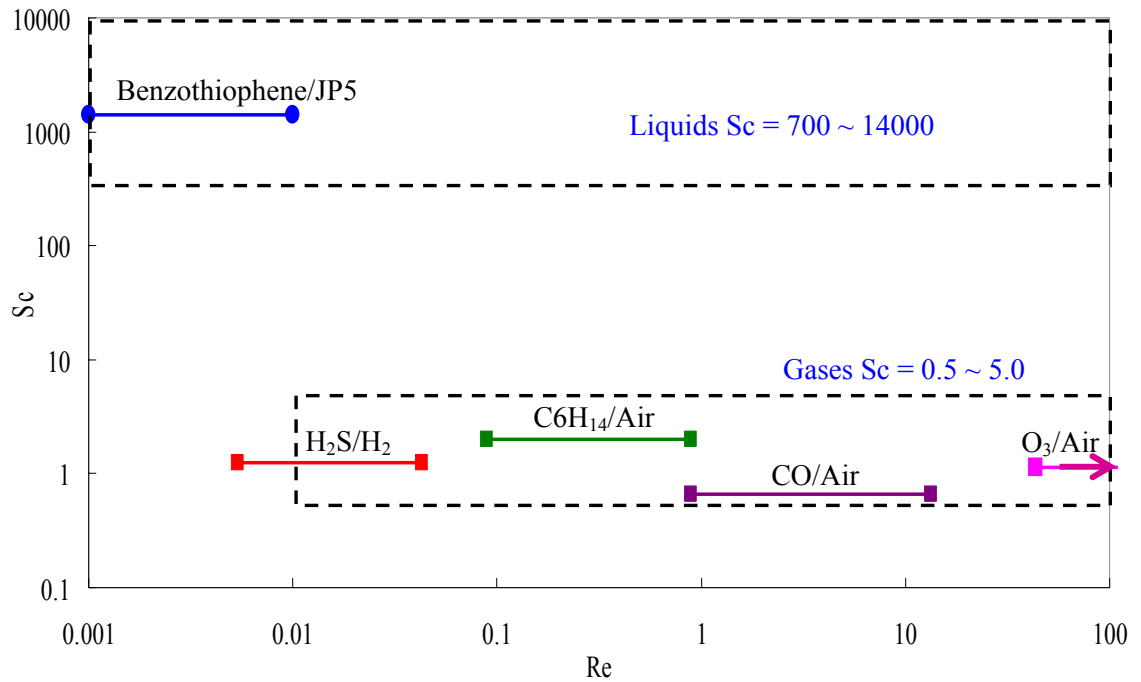


**Fig. 6.4 Re and Sc ranges for various gas and liquid phase applications**

As the focus of this study was on gas phase applications, the Re and the Sc ranges were restricted to gas phase ranges shown above. Flow and species mass conversion in each geometry were simulated at five different Re (0.01, 0.1, 1.0, 10 and 100) and three different Sc (0.5, 2.0 and 5.0), i.e., a total of 15 ( $Re \times Sc = 5 \times 3$ ) cases (flow conditions) for each geometry. Variations in Re and Sc were achieved by changing  $u_0$  ( $4.2 \times 10^{-5}$ ,  $4.2 \times 10^{-4}$ ,  $4.2 \times 10^{-3}$ ,  $4.2 \times 10^{-2}$ ,  $4.2 \times 10^{-1}$  and 4.2 m/s) and  $D_{AB}$  ( $3.37 \times 10^{-5}$ ,  $8.43 \times 10^{-6}$  and  $3.37 \times 10^{-6} \text{ m}^2/\text{s}$ ) respectively, without altering other parameters. The operating conditions used were 313 K and 1 atm (at the center of the geometry) for all the simulations. Similarly, viscosity and density values were fixed at  $1.90 \times 10^{-5} \text{ Pa.s}$  and  $1.128 \text{ kg/m}^3$ , respectively. These values correspond to that of air at the operating conditions mentioned above. The properties (molecular weight, etc.) of the hypothetical molecules A and B both were the same as that of the air.

Table 6.2 shows the matrix of various geometries for which the mass transfer analysis was made. The ratio ( $d_{ch}/d_f$ ) was varied by changing  $d_f$ , while  $d_{ch}$  was kept constant at 400  $\mu\text{m}$  for all the simulations. The effect of fiber volume loading was studied only for a specific case of  $d_{ch}/d_f = 40$  (10  $\mu\text{m}$  fiber) with fibers volume variations as shown in the table. Further, the fiber distribution effect was studied by varying the ‘a/b’ ratio (distance between the wall and the nearest row of fibers to the distance between two consecutive fiber rows) shown in Fig 6.2(b).

**Table 6.2 Matrix of various geometries used in the mass transfer study**

Geometry Type	Parameter Studied (Range of Values)	Fiber dia. ( $\mu\text{m}$ )	Fiber Vol. %	a/b ratio
With Fiber	$d_{\text{ch}}/d_{\text{f}}$ (20~80)	5, 10 & 20	1.57	1.5
	Fiber Vol. %	10	1.57 & 3.14	1.5
	a/b (1~1.5)	10	1.57	1 & 1.5
Without Fiber	Parabolic and Flat Velocity Profiles	N/A	0	N/A

Mass transfer simulations were also done in the open channel geometry (without fibers) of Fig 6.2 (a) for parabolic velocity profiles (which occur in laminar flows in open channels) to compare with the conversions in channels with fibers. Lastly, a hypothetical case of a perfectly flat velocity profile (ideal plug flow conditions) in the Fig 6.2 (a) geometry (not influenced by the wall momentum transfer) was also simulated to estimate the mass transfer rate under ideal plug flow conditions. This was done by initializing the velocity profile in the entire domain with the inlet velocity and turning off the momentum equations in Fluent settings and solving only the species mass balance equations. The total number of geometries thus studied was 7 and the total number of cases run were 75 ( $= 15 \times 7$ ).

At the end, the ability of the dimensionless study in predicting the results for the any specific application and flow conditions was also verified using the results of the two preliminary studies (Hexane and  $\text{H}_2\text{S}$ ) mentioned above.

### VI.3.2. Static Mixing Study

In the static mixing study only one set of flow conditions, which represent the highest flow rates used in the mass transfer study, were employed. The rationale here is that the static mixing effect of fibers, if significant, would be evident at the highest velocities as has been discussed before (Section VI.1.1). This is further justified in the results section (VI.5). Table 6.3 lists these conditions. The geometries used in this study are shown in Fig. 6.3. A 1.57% volume loading of 10  $\mu\text{m}$  fibers was used in the fiber geometry. There are no walls and the fibers were distributed uniformly throughout the central part (excluding inlet and outlet regions) of the geometry (Fig. 6.3(b)).

**Table 6.3 Operating and flow conditions used in static mixing study**

Physical Property	Value
Temperature (K)	313
Operating Pressure (atm)	1
Viscosity (kg/m/s)	$1.90 \times 10^{-5}$
Diffusivity ( $\text{m}^2/\text{s}$ )	$8.41 \times 10^{-6}$
Velocity (m/s)	4.2
Molecular weights A and B (g/gmol)	28.966

## VI.4. Numerical Simulations

### VI.4.1. Governing Equations

The equations that were solved to simulate the incompressible, laminar, steady state flows in the 2D geometries discussed in this chapter include mass (equation 6.3), momentum (equations 6.4 and 6.5) and species (equation 6.6) conservation equations:

$$(\vec{\nabla} \bullet \vec{V}) = 0 \quad (6.3)$$

$$\rho [\vec{\nabla} \bullet (u \vec{V})] = -\frac{\partial p}{\partial x} + \frac{\partial \tau_{xx}}{\partial x} + \frac{\partial \tau_{yx}}{\partial y} \quad (6.4)$$

$$\rho [\vec{\nabla} \bullet (v \vec{V})] = -\frac{\partial p}{\partial y} + \frac{\partial \tau_{xy}}{\partial x} + \frac{\partial \tau_{yy}}{\partial y} \quad (6.5)$$

$$\rho \vec{V} \bullet \vec{\nabla} (x_A) = \rho D_{AB} \vec{\nabla}^2 (x_A) \quad (6.6)$$

where the viscous stresses are given by

$$\text{Normal stresses: } \tau_{xx} = 2\mu \frac{\partial u}{\partial x} - \frac{2}{3}\mu \vec{\nabla} \bullet \vec{V}; \quad \tau_{yy} = 2\mu \frac{\partial v}{\partial y} - \frac{2}{3}\mu \vec{\nabla} \bullet \vec{V}; \quad (6.7)$$

$$\text{Shear stresses: } \tau_{xy} = \tau_{yx} = \mu \left( \frac{\partial v}{\partial x} + \frac{\partial u}{\partial y} \right); \quad (6.8)$$

For the flow conditions used in this study the fluid phase was assumed to be an isothermal incompressible ideal gas and the fluid properties of viscosity and diffusivity were assumed to be constant. As mentioned before the energy (heat transfer) equations were turned off (not included) in the solutions. The ideal gas law (equation 6.9) was used to estimate the density of the incompressible gas. The operating conditions (temperature and pressure) specified in Section VI.3 were used in this density calculation:

$$\rho = \frac{P}{RT} M \quad (6.9)$$

## VI.4.2. Boundary Conditions

### VI.4.2.1. Mass Transfer Study

To achieve a well developed flow in the channels the simplest method is to use a periodic boundary condition (for momentum equations only) which connects the inlet and the outlet. But, Fluent does not allow for the use of periodic boundary conditions with species mass transport problems. Therefore, in order to eliminate the effect of an underdeveloped flow in the entrance region, pseudo-periodic boundary conditions were employed at the inlet face (for both open and fiber cases shown in Figs. 6.2 (a) and 6.2 (b), respectively). In order to do this, well developed flow patterns for similar geometries and flow conditions were obtained using periodic boundary conditions (equation 6.10) in a separate set of simulations (with species transport equations turned off). It has to be noted here that the ‘periodic’ boundary condition in Fluent does allow for a pressure gradient while imposing periodicity on velocity components. The inlet velocity profiles from these additional cases were then imported to the corresponding main cases involving species mass transport rates.

$$u|_{(x=0,y)} = u|_{(x=L,y)} , \quad v|_{(x=0,y)} = v|_{(x=L,y)} \quad (6.10)$$

A constant inlet challenge concentration (with no inlet diffusion) (equation 6.11) of  $C_{A0} = 100$  ppmv and temperature of  $T_0 = 313$ K were used at the entrance face for all the cases.

$$C_A|_{(x=0,y)} = C_{A0}, \quad T|_{(x=0,y)} = T_0 \quad (6.11)$$

An ‘outflow’ boundary condition in Fluent was employed at the all the outlets. This condition effectively sets the axial gradients of velocity components and concentration (not pressure) equal to zero at the outlet plane (equation 6.12).

$$\left. \frac{\partial u}{\partial x} \right|_{(x=L,y)} = 0, \quad \left. \frac{\partial v}{\partial x} \right|_{(x=L,y)} = 0 \quad \text{and} \quad \left. \frac{\partial C_A}{\partial x} \right|_{(x=L,y)} = 0 \quad (6.12)$$

For the micro-scale geometries used in this study the no-slip wall boundary condition may not be applicable [6.10]. Hence the Surfaces of the fibers and particles were defined as high Knudsen number slip walls by enabling the low-pressure slip boundary formulation in Fluent. This boundary condition essentially uses the first-order Maxwell velocity-slip boundary condition (equation 6.13). More details of this can be found in the Fluent User’s Guide [6.11].

$$U_s - U_w = \frac{2 - \sigma_v}{\sigma_v} \lambda \frac{\partial U}{\partial r} \quad (6.13)$$

The concentration of the challenge gas (component A) at the channel wall surface was fixed at zero (equation 6.14). This boundary condition is essentially equivalent to an infinitely fast wall surface reaction (or adsorption), which implies a complete fluid phase mass transfer controlled condition.

$$C_A|_{(x, y = \pm d_{ch} / 2)} = 0 \quad (6.14)$$



The normal concentration gradient at the fiber surface was set to zero (equation 6.15), which makes the fibers inert (or chemically inactive).

$$\left. \frac{\partial C_A}{\partial r} \right|_{Fiber\ Surface} = 0 \quad (6.15)$$

The heat fluxes at the fiber and the channel walls were customarily set to zero (adiabatic conditions), but these boundary conditions did not have any effect on the simulations as the energy equations in all the simulations was deactivated.

#### VI.4.2.2. Static Mixing Study

Unlike the previous study where imported velocity profiles were used at the inlets, in this study a constant velocity (equation 6.16) was employed at both the inlet zones. Imported velocity profiles could not be used as the velocities (flow rates) in both the geometries and in both the inlet zones, were to remain the same.

$$u|_{(x=0,y)} = const. , \quad v|_{(x=0,y)} = 0 \quad (6.16)$$

The concentration of component A in zone 2 was set at 100 ppmv ( $C_{A0}$ ) and in zone 1 was set to zero (Fig 6.3 (a) and (b)) and the temperature was set at 313 K in both the zones

$$C_A|_{(x=0, zone\ 2)} = C_{A0} , \quad C_A|_{(x=0, zone\ 1)} = 0 \quad \text{and} \quad T|_{(x=0,y)} = T_0 \quad (6.17)$$

The top and bottom faces of the geometries were symmetry boundary conditions which imply zero vertical gradients of velocity, pressure, concentration.

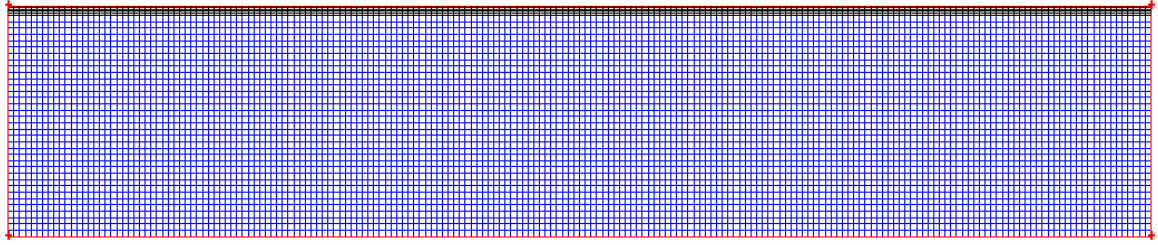
$$\left. \frac{\partial u}{\partial y} \right|_{(x, y = \pm d_{ch})} = 0, \quad \left. \frac{\partial v}{\partial y} \right|_{(x, y = \pm d_{ch})} = 0,$$

$$\left. \frac{\partial p}{\partial y} \right|_{(x, y = \pm d_{ch})} = 0 \quad \text{and} \quad \left. \frac{\partial C_A}{\partial y} \right|_{(x, y = \pm d_{ch})} = 0 \quad (6.18)$$

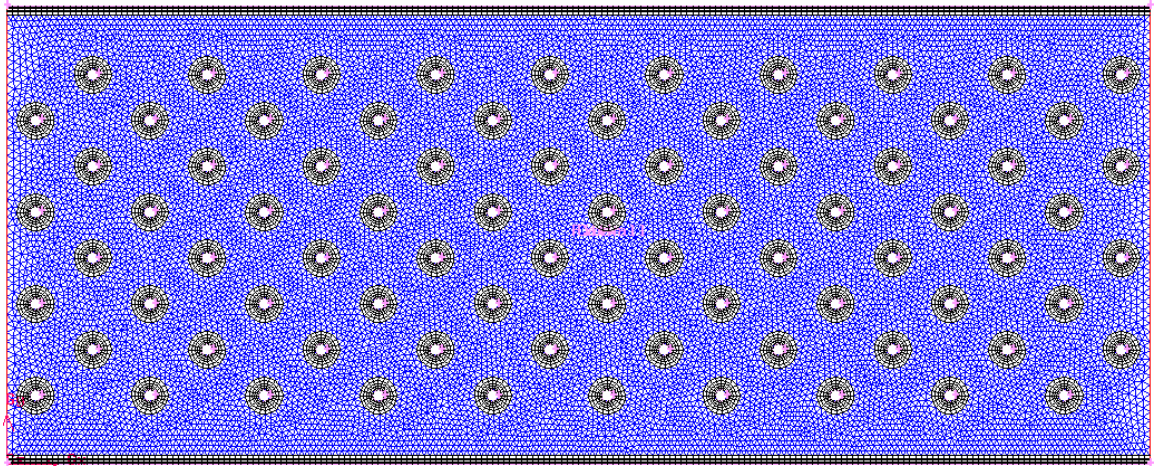
The surfaces of fibers and the outlet had similar velocity and concentration gradients as the corresponding conditions in the mass transfer study.

#### VI.4.3. Grid Generation

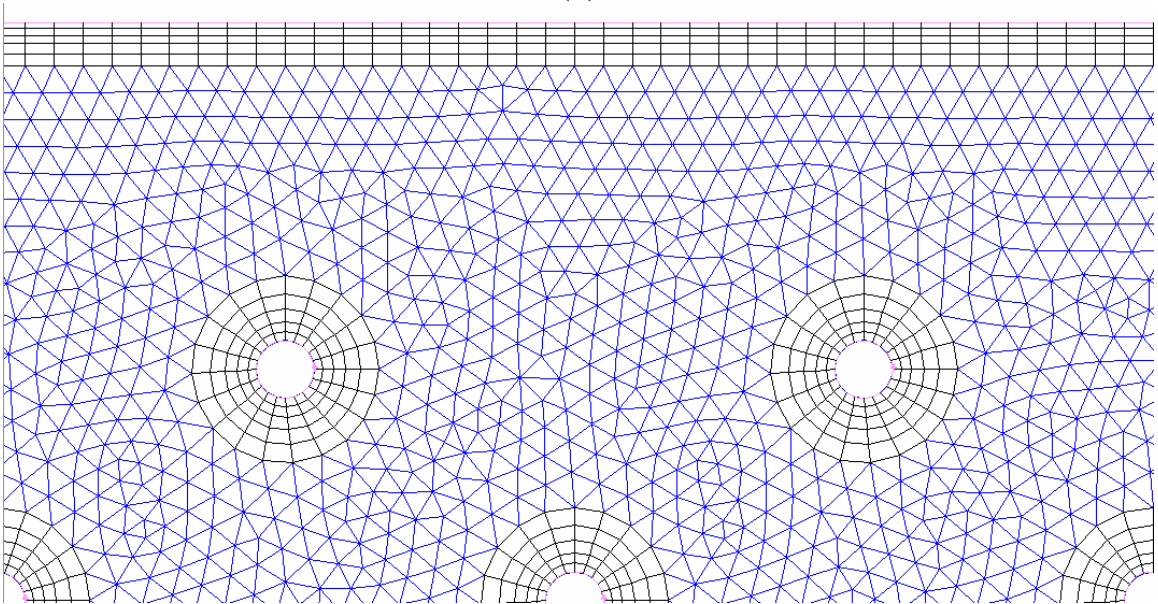
The grids/flow-field meshes for all the geometries were generated using GAMBIT 2.3, a Fluent preprocessor (or grid generation software). While the interiors of all the open channel geometries (without fibers) were meshed using structured grids with quadrilateral elements, the interiors of all the fiber geometries were meshed using unstructured grids with triangular elements. In both the cases structured boundary layers with quadrilateral elements were used on the all wall surfaces (fibers and channel walls). For open geometries only the upper half of the domain was solved, making use of the inherent symmetry (about the horizontal center line) present in it. But for the fiber channels this was not possible and hence the entire geometries were used in simulations. Fig 6.5 shows sample meshes of fiber and open channel geometries used in these studies.



(a)



(b)



(c)

**Fig. 6.5. (a) Quadrilateral structured mesh (interior and boundary layer) in open geometry without fibers; (b) and (c) Triangular unstructured mesh in the interior with quadrilateral structured boundary layer on fibers and walls in fiber geometries**

#### **VI.4.4. Discretization and Solution**

As mentioned before, the solution for these numerical problems was obtained using Fluent 6.3. This software uses a finite volume based method of discretization to solve the partial differential equations discussed in section VI.4.1. An iterative solution approach is employed where the solution is advanced in pseudo-time until the residuals converged. The governing equations are solved sequentially at each iteration using a segregated solver which employed a second-order upwind scheme.

#### **VI.4.5. Iterative Convergence**

The residuals for each equation were normalized by their initial values and monitored at the end of each iteration. Iterative convergence was judged by using these normalized residuals of continuity, x and y velocity components and concentration. The definitions of the residuals are given in Fluent user guide [6.11]. Each of these cases was iterated until all the above residuals became more or less constant (with some fluctuations), at this stage the solutions can be said to be converged. A sample iterative residual convergence plots for a of fiber channel case ( $Re = 100$ ,  $Sc = 0.5$ ,  $(d_{ch}/d_f) = 40$ ,  $FV = 1.57\%$  and  $(a/b) = 1.5$ ) and an open channel case ( $Re = 100$  and  $Sc = 0.5$ ) are shown in 6.6 and 6.7, respectively. The residuals decreased gradually with successive iterations and eventually became constant. The graphs shown demonstrate that the results are iteratively converged. Similar convergence plots have been obtained for all the other cases considered in this study.

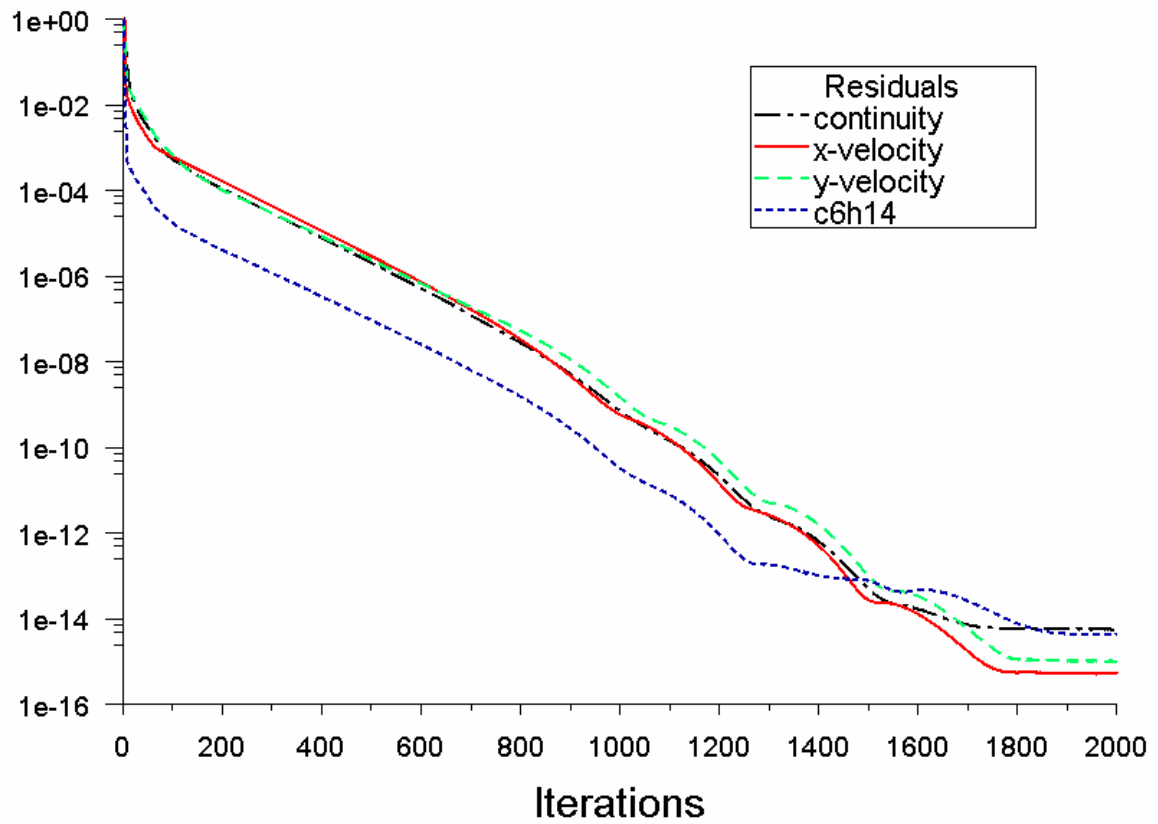


**Fig. 6.6. Normalized residual convergence plot in open channel geometry (Re = 100 and Sc = 0.5)**

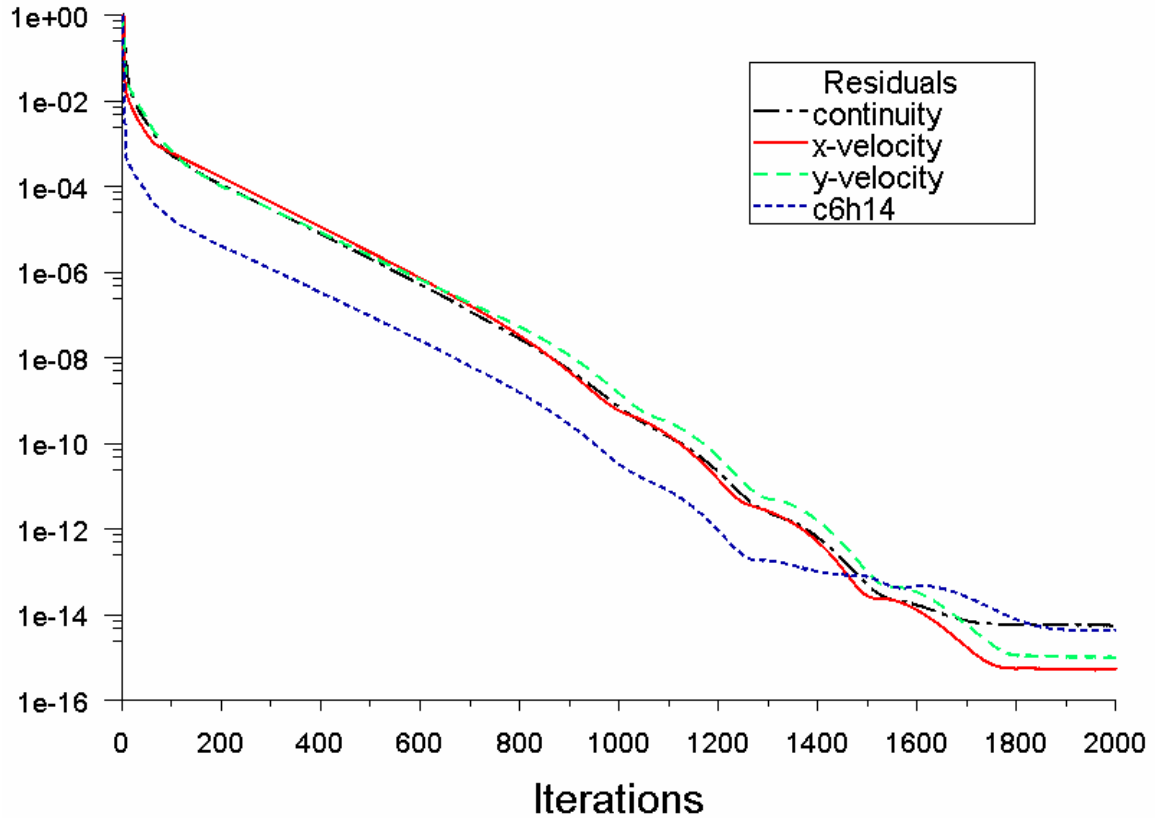


**Fig. 6.7. Normalized residual convergence plot in fiber channel geometry**  
**( $Re = 100$ ,  $Sc = 0.5$ ,  $(d_{ch}/d_f) = 40$ ,  $FV = 1.57\%$  and  $(a/b) = 1.5$ )**

#### VI.4.6. Grid Convergence

As the numerical solution involves discretization of differential equations, the solution obtained does not precisely match the corresponding exact solution. The difference in these two solutions, arising due to discretization is called discretization error. Quantification of discretization error is essential, as it is the primary source of numerical errors in CFD simulations. The exact solution of the physical quantities (outlet concentration, pressure gradient, etc) has been estimated using generalized Richardson extrapolation [6.12].

$$f_{exact} = f_1 + \frac{f_1 - f_2}{r^{p'} - 1} \quad (6.19)$$

$$\text{where, } f = C_{out}, (\Delta P / L) \quad (6.20)$$

and  $f_1, f_2$  and  $f_3$  are solutions at fine, medium and coarse grids, respectively. The quantity  $p'$  in the above equation was set to the formal order of accuracy, which is 2.0 for these simulations (second order accuracy, Section VI.4.4). Further, the relative discretization errors (RDE) for various grids ( $i=1, 2, \text{ and } 3$ ) have been estimated as follows [6.12]:

$$RDE = \frac{f_i - f_{exact}}{f_{exact}} \times 100\% \quad (6.21)$$

Estimates of discretization error in outlet concentration and pressure gradients for various grids in the open channel geometry, for the case of  $Re=100$  and  $Sc=0.5$  are shown in Table 6.4. Similar results for a fiber channel for  $Re = 100$ ,  $Sc = 0.5$ ,  $(d_{ch}/d_f) = 40$ ,  $FV = 1.57\%$  and  $(a/b) = 1.5$  are shown in Table 6.5. Further, the observed order of accuracy and the formal order of accuracy (2.0) of the numerical solution were also compared. The observed order of accuracy  $p''$  of the numerical solution was calculated using solutions on three grids using the following equation [6.13]:

$$\left( \frac{f_3 - f_2}{r_{23}^{p''} - 1} \right) = r_{12}^{p''} \left( \frac{f_2 - f_1}{r_{12}^{p''} - 1} \right); \quad r_{ij} = \sqrt[n]{\frac{N_i}{N_j}} \quad (6.22)$$

Three flow-field grids were created by uniformly refining the grid throughout the domain in both the directions (x and y). The grid refinement factors used are shown in tables below. The tables also show the observed order of accuracy found from the pressure gradients and outlet concentrations on the three meshes. The observed orders of accuracy for open channel geometry with structured quadrilateral grids, were found to be

between 2.0 and 2.16. For the fiber channels with unstructured grids, the observed orders of accuracy were found to be between 1.4-1.6. These values are close to the formal order of accuracy 2.0, which confirms the grid convergence criteria. Medium grids were used in the entire study to optimize the computational time and still keep the errors within reasonable limits.

**Table. 6.4. Grid convergence and discretization error analysis for open channel (Re = 100 and Sc = 0.5)**

Open Channel	Grid Type	No. of Elements	Grid Refinement Factor	Value	Estimated Exact Solution	Estimated Error %	Observed Order of Accuracy
$\Delta P/L(\text{Pa/m})$	Fine	30720	1.600	5974.62	5975.27	0.011	2.04
	Medium	12000	1.667	5973.61		0.028	
	Coarse	4320	-	5970.60		0.078	
$C_{Aout}$ (Mole Frac.)	Fine	30720	1.600	6.294E-05	6.295E-05	0.008	2.16
	Medium	12000	1.667	6.293E-05		0.020	
	Coarse	4320	-	6.291E-05		0.057	

**Table. 6.5. Grid convergence and discretization error analysis for fiber channel (Re = 100, Sc = 0.5,  $(d_{ch}/d_f) = 40$ , FV = 1.57% and  $(a/b) = 1.5$ )**

Fiber Channel	Grid Type	No. of Elements	Grid Refinement Factor	Value	Estimated Exact solution	Estimated Error	Observed Order of Accuracy
$\Delta P/L(\text{Pa/m})$	Fine	94896	1.600	239791.43	241421.92	0.675	1.55
	Medium	38654	1.667	237247.87		1.729	
	Coarse	14314	-	231315.03		4.186	
$C_{Aout}$ (Mole Frac.)	Fine	94896	1.600	4.812E-05	4.809E-05	0.073	1.40
	Medium	38654	1.667	4.818E-05		0.186	
	Coarse	14314	-	4.829E-05		0.432	

#### VI.4.7. Post-processing Calculations

The log reduction of component A across the length of any channel in the mass transfer study was calculated as follows:



$$\text{Log reduction} = \text{Log}_{10} \left( \frac{C_A|_{x=0}}{C_A|_{x=L}} \right) \quad (6.21)$$

Mass transfer coefficients were estimated using the following formula:

$$k_m = \text{Log}_e \left( \frac{C_A|_{x=0}}{C_A|_{x=L}} \right) \frac{u_0 \cdot d_{ch}}{2L} \quad (6.24)$$

The difference between the mass transfer (MT) rates of a given fiber channel geometry and the open channel geometry with parabolic velocity profiles gives the change in mass transfer rates due to the inclusion of fibers. Therefore, the percentage increase in mass transfer rates due to the inclusion of fibers for any fiber geometry can be calculated as:

$$\% \text{ increase in MT rate in due to fibers} = \left( \frac{MT_{FC} - MT_{OCPV}}{MT_{OCPV}} \right) \times 100 \% \quad (6.25)$$

Basing on the definition of Sh, the above equation can also be written as:

$$\% \% \text{ increase in MT rate in due to fibers} = \left( \frac{Sh_{FC} - Sh_{OCPV}}{Sh_{OCPV}} \right) \times 100 \% \quad (6.26)$$

Similarly, the percentage increase in mass transfer rates in the open channel with flat velocity as opposed to the case with the parabolic velocity profile in the same geometry can be calculated as follows:

$$\% \text{ increase in MT rate with flat velocity profile} = \left( \frac{MT_{OCFV} - MT_{OCPV}}{MT_{OCPV}} \right) \times 100 \% \quad (6.27)$$

This equation can also be modified to the following form:

$$\% \text{ increase in MT rate with flat velocity profile} = \left( \frac{Sh_{OCFV} - Sh_{OCPV}}{Sh_{OCPV}} \right) \times 100 \% \quad (6.28)$$

where the subscripts stand for the following:

FC = Fiber channel geometry

OCPV = Open channel with parabolic velocity profile

OCFV = Open channel with flat velocity profile (ideal plug flow conditions)

The quality of mixing in the static mixing study was quantified using the Coefficient of Variation (COV), defined as follows:

$$COV = 1 - \sqrt{\frac{\sigma^2}{\sigma_{\max}^2}} \quad (6.29)$$

$$\text{where } \sigma^2 = \frac{\sum_{i=1}^m u_i (C_{Ai} - \bar{C}_A)^2}{m u_0} \quad (6.30)$$

with  $n$  being the number of grid points in the outlet,  $C_{Ai}$  and  $u_i$  the concentration of component A and gas velocity in x direction at  $i^{\text{th}}$  grid point, respectively,  $\bar{C}_A$  the mixed cup concentration of component A and  $\sigma_{\max}$  the maximum value of  $\sigma$  which occurs at the inlet of the channel where the two streams are completely unmixed (separate).

## VI.5. Results

### VI.5.1. Mass Transfer Study

Plots of log reductions and mass transfer coefficients for  $\text{H}_2\text{S}/\text{H}_2$  and Hexane/Air systems for the open channel and a fiber channel geometry ( $(d_{\text{ch}}/d_f) = 40$ ,  $\text{FV} = 1.57\%$  and  $(a/b) = 1.5$ ) are shown in Figs. 6.8 and 6.9, respectively. As described before, in all these simulations both open and fiber channel widths were fixed at  $400 \mu\text{m}$ . Log reductions decreased with velocity due to decreased residence times, but mass transfer coefficients (and mass transfer rates) increased with increasing velocity. Mass transfer

rates and conversion (or log reduction) were higher for the  $\text{H}_2\text{S}/\text{H}_2$  case compared to the hexane/air case because of the higher diffusivity of  $\text{H}_2\text{S}$  in  $\text{H}_2$ . These graphs show that the fiber channels have higher conversions and mass transfer rates compared to open channels for similar operating conditions.

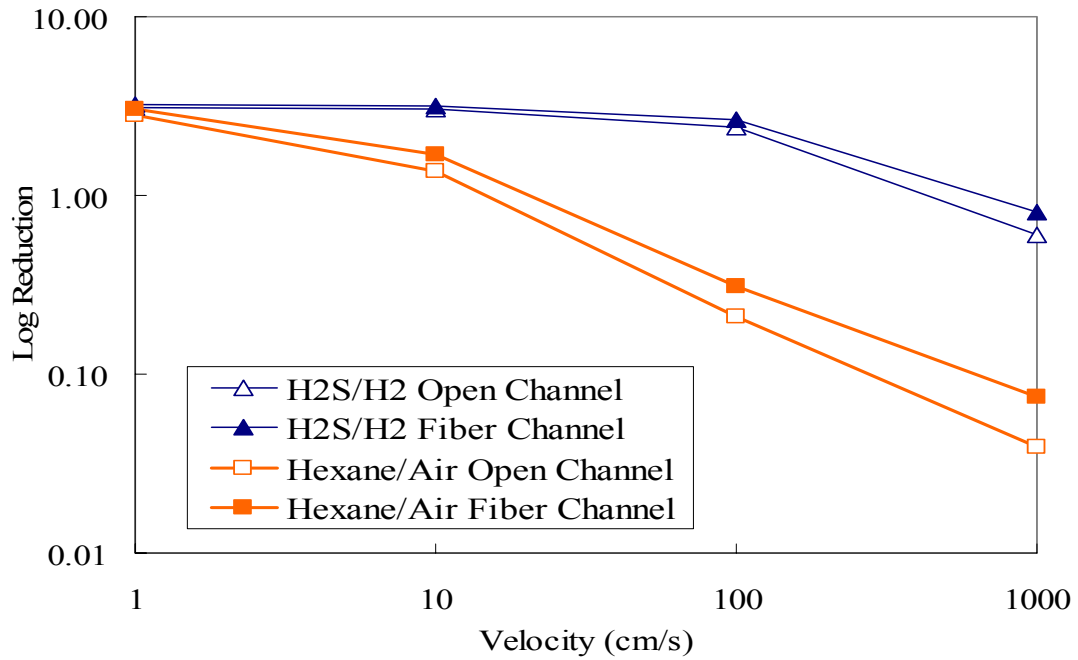


**Fig. 6.8. Log reductions for  $\text{H}_2\text{S}/\text{H}_2$  and Hexane/Air systems for various velocities ( $d_{\text{ch}} = 400 \mu\text{m}$ ,  $d_f = 10 \mu\text{m}$ ,  $\text{FV} = 1.57\%$  and  $(a/b) = 1.5$ )**

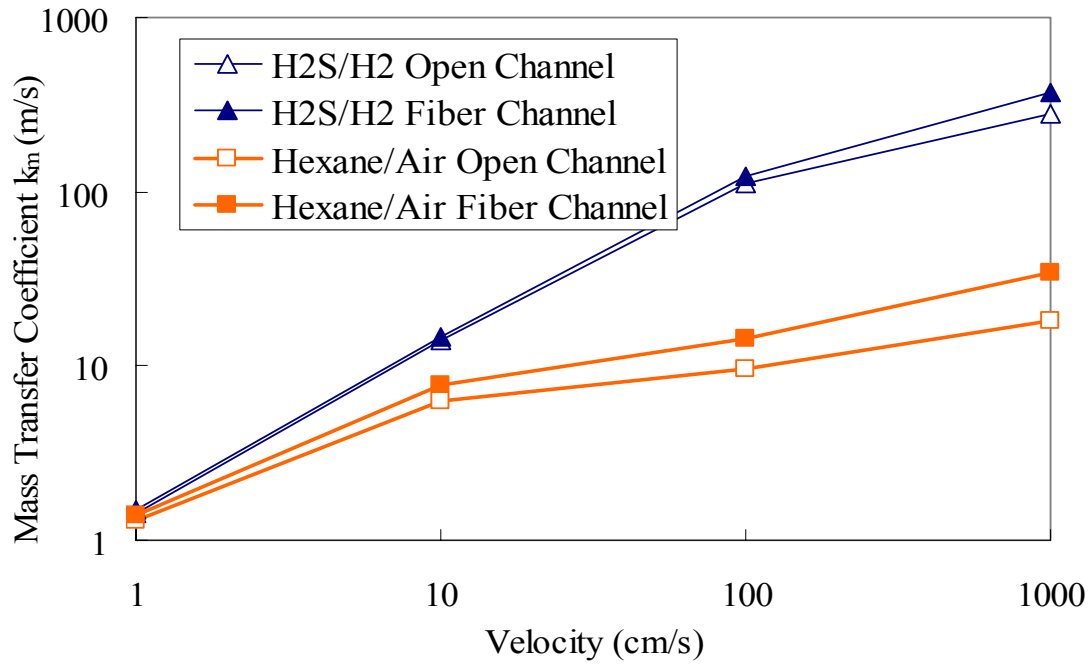


**Fig. 6.9. Mass transfer coefficients for H<sub>2</sub>S/H<sub>2</sub> and Hexane/Air systems for various velocities ( $d_{ch} = 400 \mu\text{m}$ ,  $d_f = 10 \mu\text{m}$ ,  $FV = 1.57\%$  and  $(a/b) = 1.5$ )**

From these data the percentage increases in mass transfer rates with inclusion of fibers in channel geometries were calculated (equation (6.25)) and are shown in Fig. 6.10. This plot clearly depicts the benefits of inclusion of fibers in the channels, which is not very apparent from the Figs. 6.8 and 6.9. The percentage increase in mass transfer (MT) rate due to the fibers rises with increase in velocity. Also the improvement is higher in the case of the Hexane/Air system as compared to H<sub>2</sub>S/H<sub>2</sub>. This is because of the high diffusivity of the H<sub>2</sub>S in H<sub>2</sub>, which creates high radial diffusion and hence minimizes the effect of the non-idealities caused by parabolic velocity profiles.

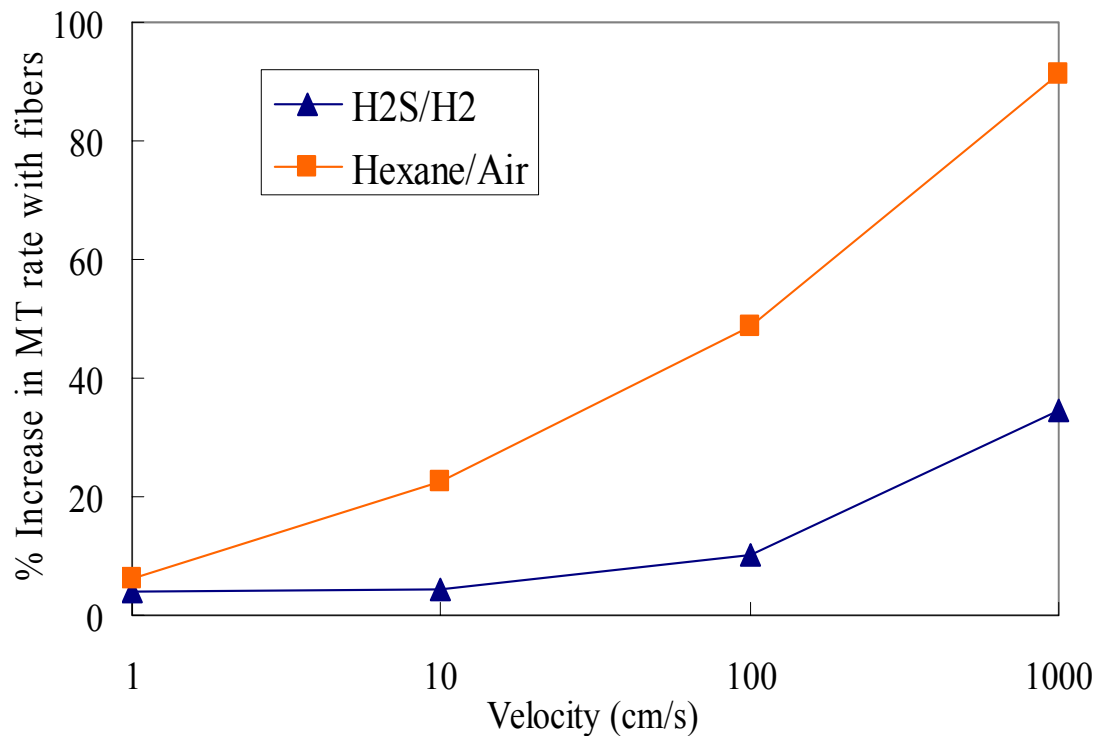


**Fig. 6.10. Percentage increase in MT rate for H<sub>2</sub>S/H<sub>2</sub> and Hexane/Air systems for various velocities ( $d_{ch} = 400 \mu\text{m}$ ,  $(d_{ch}/d_f) = 40$ ,  $FV = 1.57\%$  and  $(a/b) = 1.5$ )**

Further, this improvement in mass transfer rates with inclusion of fibers in channel geometries observed in H<sub>2</sub>S and hexane studies and the various factors influencing this phenomenon were examined in detail using the dimensionless variable study (as described in Section VI.3.1). Fig. 6.11 shows the x-component velocity profiles for  $Re=100$  in open and fiber channels. Similar profiles were obtained for other  $Re$  also. For the  $Re$  range used in this study the default velocity profiles in the open channel are parabolic as shown in Fig. 6.11 (a). This deviation from plug flow condition in the open channel leads to preferred convection of high concentration reactants downstream i.e., axial dispersion of reactants/adsorbates and hence results in lower fluid-wall mass transfer rates. Fig. 6.11 (b) shows the velocity profile for a hypothetical case of open

channel with flat velocity profile or plug flow conditions as simulated in this study. Finally, Fig. 6.11 (c) shows the x-component velocity profiles for a specific case of fiber channel ( $(d_{ch}/d_f) = 40$ ,  $FV = 1.57\%$  and  $(a/b) = 1.5$ ) geometry. The velocity profiles in fiber channels are closer to flat velocity profiles or plug flow conditions and hence result in better mass transfer rates compared to open channels with parabolic velocity profiles. The fibers in the channel redistribute the flow and hence make it more uniform. Figs. 6.12 and 6.13 show direct comparisons of (x component) velocity contours and component A concentration contours ( $Sc=0.5$ ) for the above cases.

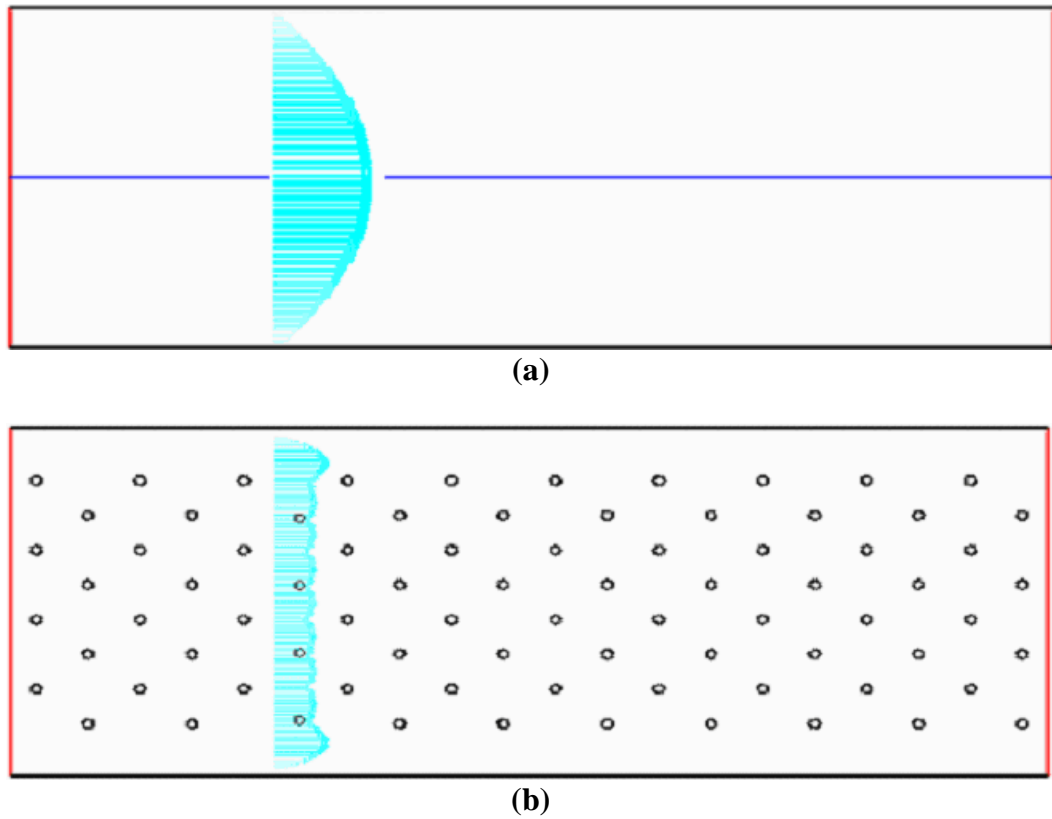


**Fig. 6.11. Velocity profiles for  $Re=100$  in (a) open channel geometry (b) fiber channel geometry ( $(d_{ch}/d_f) = 40$ ,  $FV = 1.57\%$  and  $(a/b) = 1.5$ )**

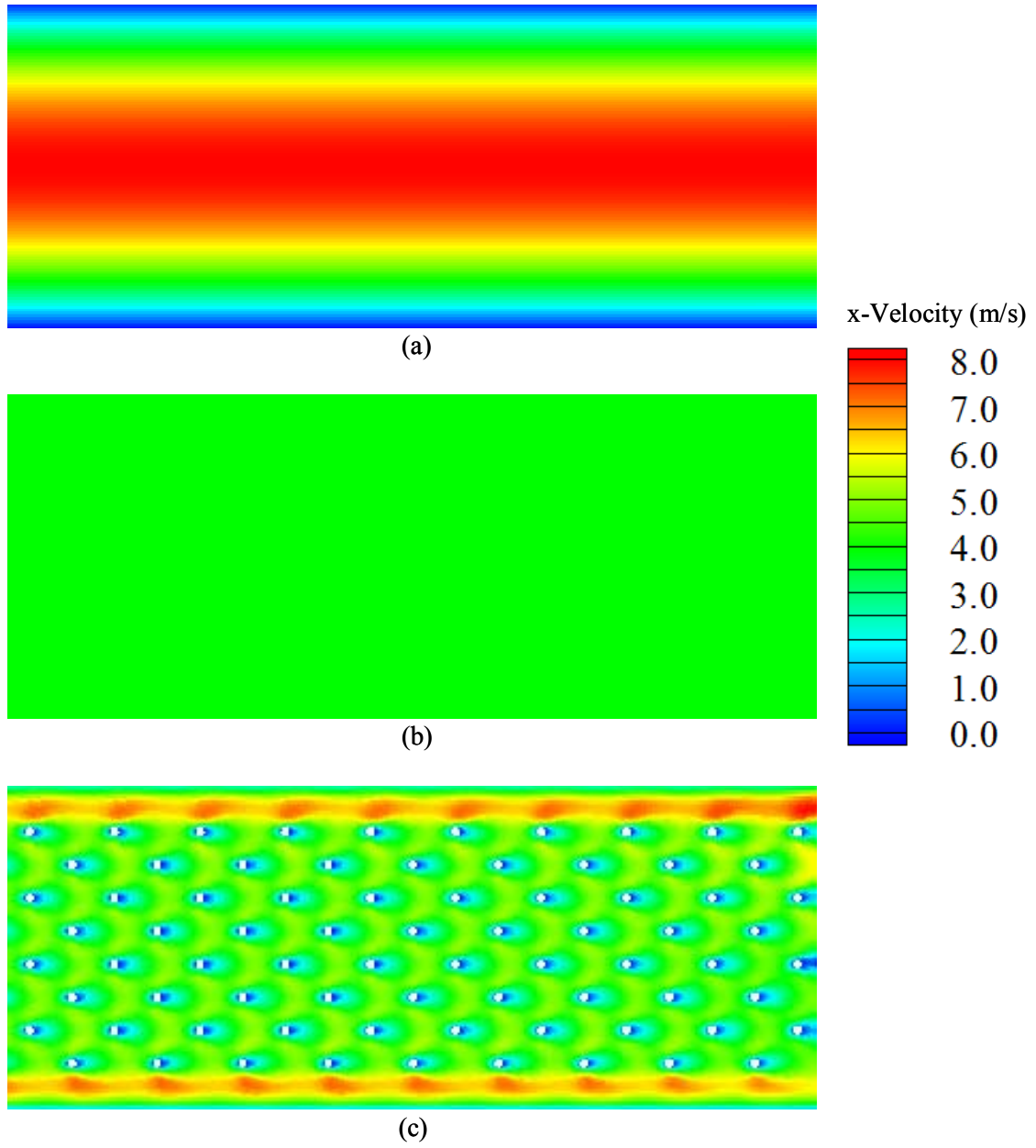


**Fig. 6.12. Velocity contours for  $Re=100$  in (a) open channel with parabolic velocity profile (b) open channel with flat velocity profile (c) fiber channel geometry ( $(d_{ch}/d_f) = 40$ ,  $FV = 1.57\%$  and  $(a/b) = 1.5$ )**

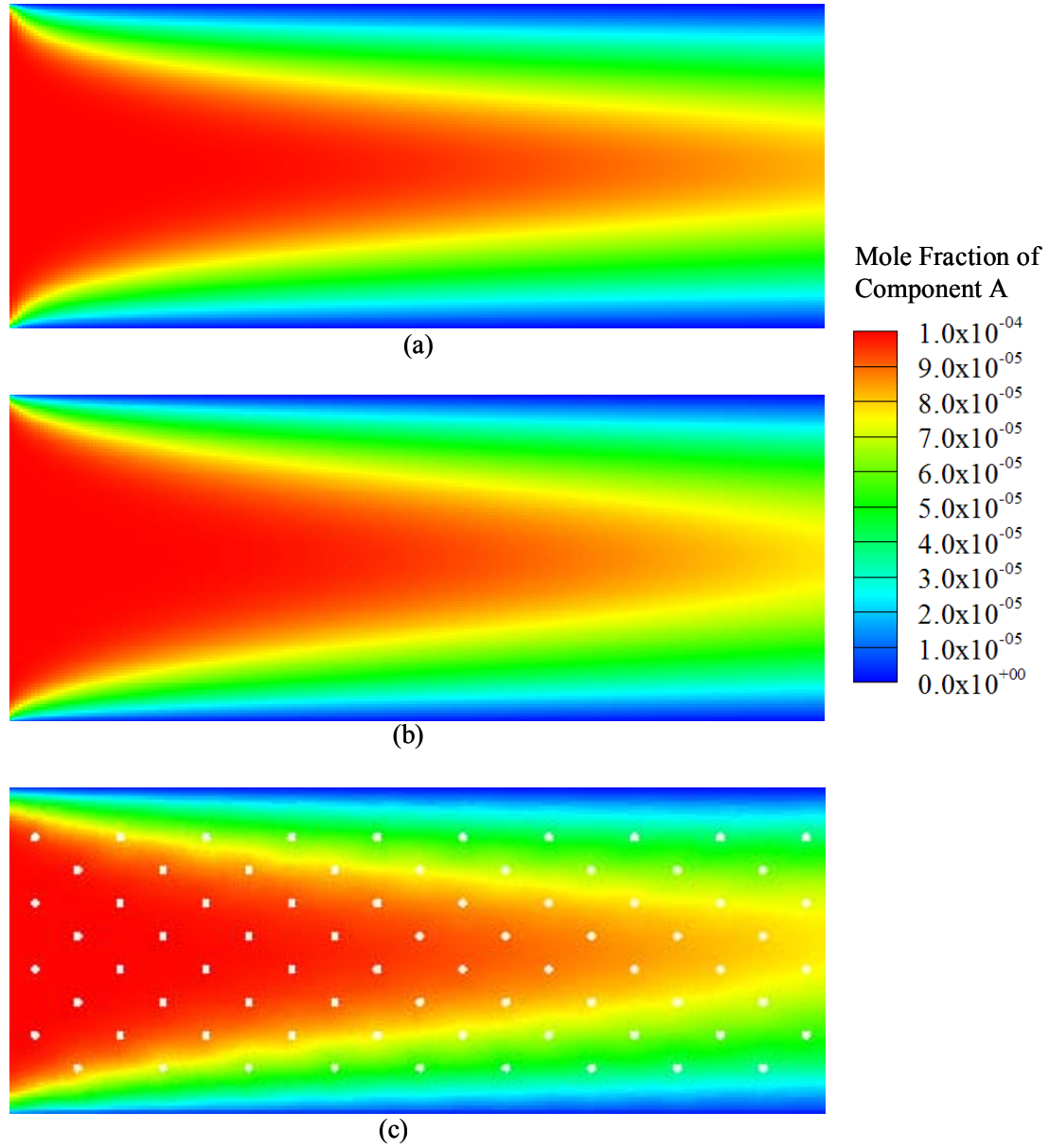
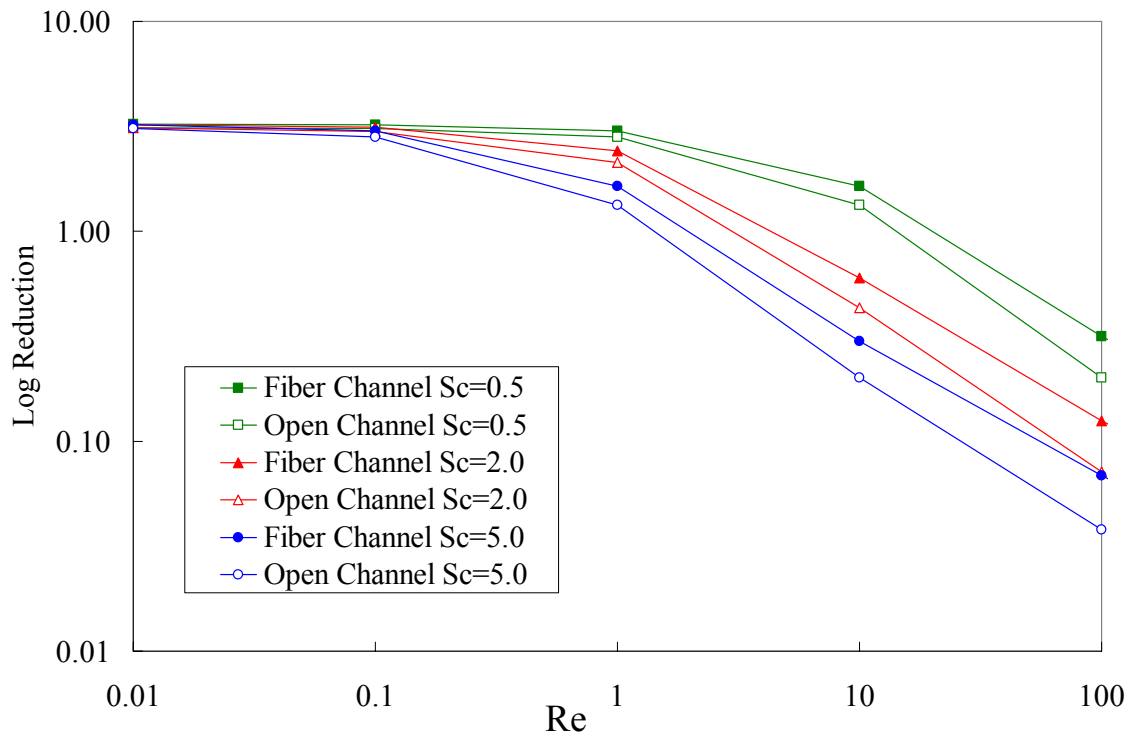


**Fig. 6.13. Concentration contours of component A for  $Re = 100$  and  $Sc = 0.5$  in (a) open channel with parabolic velocity profile (b) open channel with flat velocity profile (c) fiber channel geometry ( $(d_{ch}/d_f) = 40$ ,  $FV = 1.57\%$  and  $(a/b) = 1.5$ )**

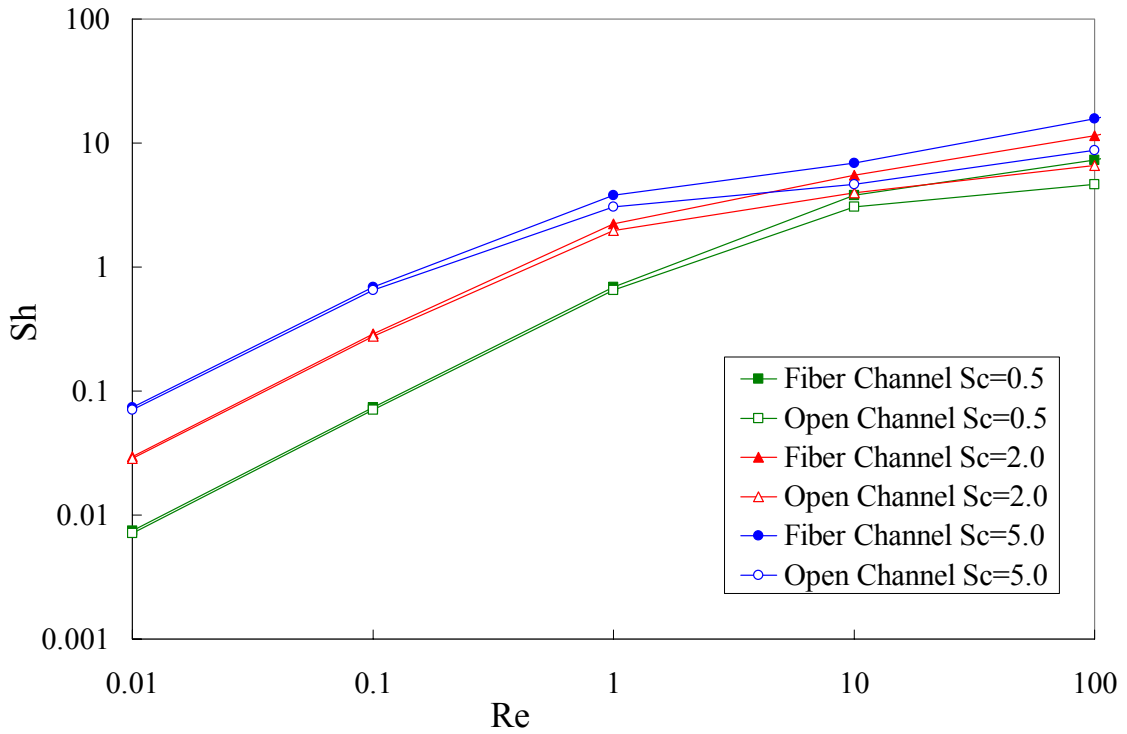
Fig. 6.14 shows the log reductions of component A for the open channel geometry with parabolic velocity profiles and a specific case of fiber channel ( $d_{ch}/d_f = 40$ ,  $FV = 1.57\%$  and  $(a/b) = 1.5$ ) geometry for a wide range of  $Re$  (0.01-100) and  $Sc$  (0.5-5.0). Fig



6.15 shows the  $Sh$  versus  $Re$  plot for the same cases. The results show a decrease in log reduction and an increase in  $Sh$  numbers with increasing  $Re$ . The log reduction in concentration of A was found to be higher in low  $Sc$  (high diffusivity) cases as expected. As observed before, the fiber channels show better performance compared to the open channels for similar operating conditions.



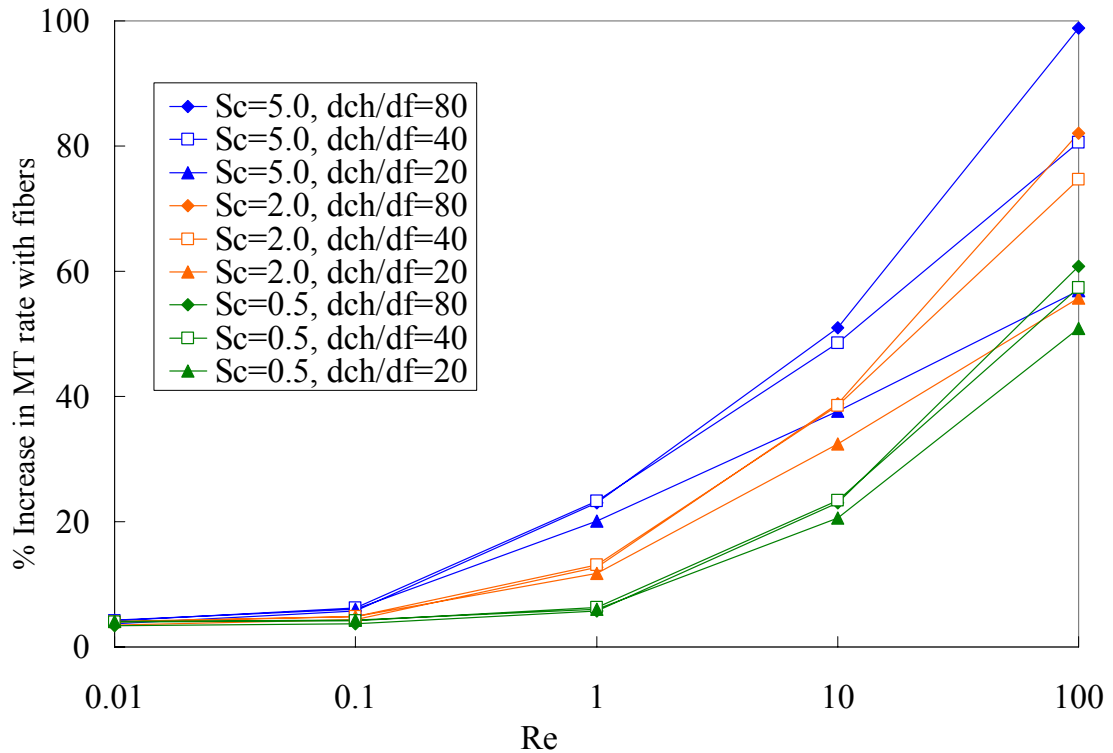
**Fig. 6.14.** Log reduction of component A for the open and the fiber channel ( $(d_{ch}/d_f) = 40$ ,  $FV = 1.57\%$  and  $(a/b) = 1.5$ ) geometries for various  $Re$  and  $Sc$



**Fig. 6.15. Sh for the open and the fiber channel ( $(d_{ch}/d_f) = 40$ ,  $FV = 1.57\%$  and  $(a/b) = 1.5$ ) geometries for various Re and Sc**

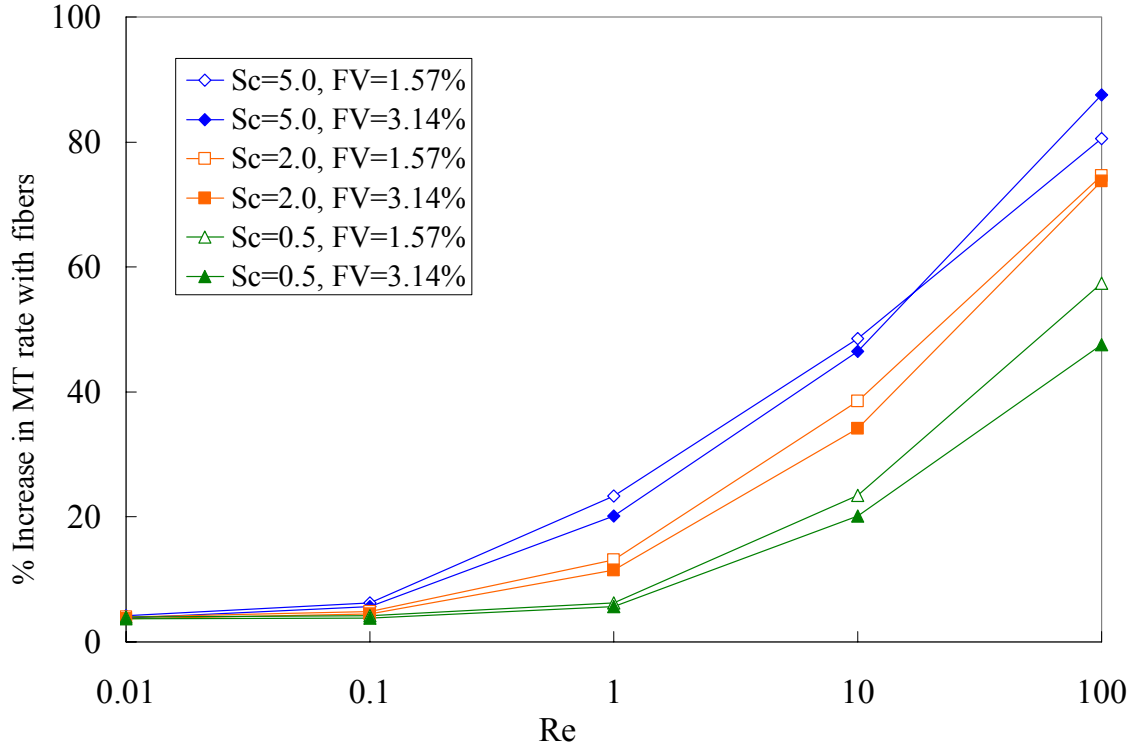
The main focus of this study is the change in the mass transfer rates due to inclusion of fibers in channels and not the mass transfer rates or conversions in fiber or open channels as such. Also, for any given Re and Sc shown above, it is not possible to give a specific value for the mass transfer coefficient (or rate) or the log reduction in fiber or open channels; these values are dependent on actual diffusivity of the problem and hence are not fixed. But, the percentage increase in mass transfer rate from open channel (with parabolic velocity profiles) to fiber channel geometries can be calculated for any Re and Sc, as it is independent of the actual diffusivity (equations 6.25 - 6.26). Therefore, in the rest of the plots here only the percentage increases in mass transfer rates due to inclusion fibers in the channels will be shown.

Fig 6.16 shows the effect of fiber diameter on percentage increases in mass transfer rates due to the inclusion of fibers in channel geometries (equation 6.26). Results obtained for various fiber diameters or  $d_{ch}/d_f$  ratios (with constant  $d_{ch} = 400 \mu m$ ) and  $Sc$  are shown as a function of  $Re$ . The percentage increases in mass transfer rates improved with a decrease in fiber diameter. This is expected as decrease in fiber diameter results in more uniform velocity profiles. After an initial increase, the mass transfer rates are expected to become constant with further decrease in fiber diameters, as the velocity profile becomes more or less flat, i.e., approaches plug flow conditions. This is evident from the fact that for any given  $Sc$ , the increase observed when going from  $d_{ch}/d_f = 20$  to 40 is more than that from  $d_{ch}/d_f = 40$  to 80.



**Fig. 6.16. Effect of fiber diameter on percentage increase in mass transfer rate due to inclusion of fibers in channel geometries (FV = 1.57% and (a/b) = 1.5)**

Fig. 6.17 illustrates the effect of fiber volume loading on percentage increases in mass transfer rates due to the inclusion of fibers in channel geometries (equation 6.26). With an increase in fiber volume loading, the velocity profiles are expected to become more uniform and hence lead to improvement in mass transfer rates. For the fiber loadings used in this study, the observed results show only small variations between 1.57% and 3.14% fiber loadings. The percentage increase in mass transfer rate increased or decreased with in fiber loading, depending on the Re and Sc regimes in consideration. This can be attributed to other factors that also play a role. As the 'a/b' ratio was kept constant in all the geometries in Fig. 6.17, the value of 'a' decreases with decreasing fiber diameter. The decreasing 'a' value can negatively effect the mass transfer rates. The effect of 'a/b' or 'a' on the mass transfer rates in fiber geometries will be discussed later in this section. Also, any increase in fiber volume loading leads to a decrease in the residence time in the channel which can further lead to lower mass transfer rates. These two factors have the opposite influence to that of the increasing uniformity in velocity profiles achieved by increasing fiber volume percentage. Hence, the results show mixed trends.



**Fig. 6.17. Effect of fiber volume loading on percentage increases in mass transfer rates due to inclusion of fibers in channel geometries ( $d_{ch} = 400 \mu m$ ,  $(d_{ch}/d_f) = 40$  and  $(a/b) = 1.5$ )**

The effect of fiber distribution ( $a/b$  ratio) on the percentage increases in mass transfer rates (equation 6.26) for fiber channels with  $d_{ch} = 400 \mu m$ ,  $(d_{ch}/d_f) = 40$  and  $FV = 1.57\%$  is shown in Fig 6.18. There is a significant improvement observed with increase in ' $a/b$ ' from 1.0 to 1.5 for all  $Re$  and  $Sc$  shown. This implies that the fiber distribution inside the channel has a significant effect. In the geometry with  $a/b$  of 1.5, the flow patterns (velocity profiles) show preferential flow paths (higher velocities) closer to the wall (Figs. 6.11 (c) and 6.12 (c)), this lead to higher mass transport rates. On the other hand when  $a/b=1.0$ , the fibers are closer to the wall and hence there is less flow near the wall than between the fibers. Therefore, the mass transfer rates for  $a/b=1.0$  are lower than

that for  $a/b=1.5$ . Similarly, a decrease in value of 'a' for same  $a/b$  also negatively effects the conversion and mass transfer rate in fiber channels.

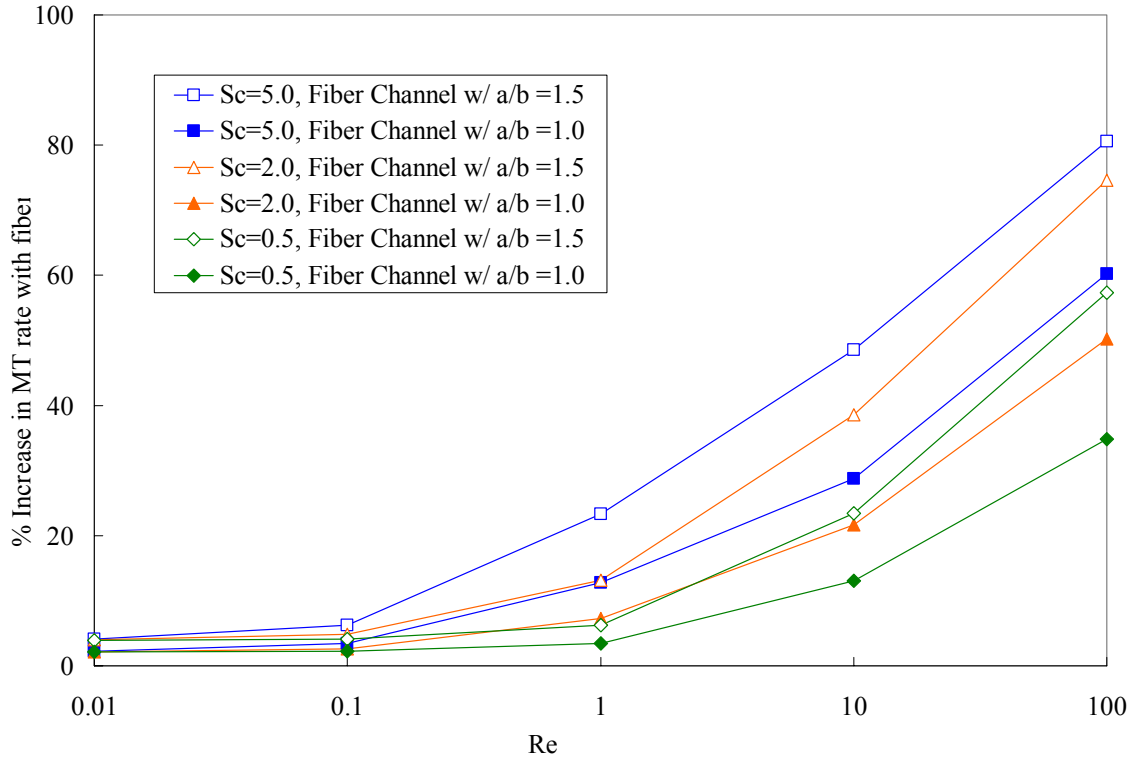


**Fig. 6.18. Effect of fiber distribution ( $a/b$ ) on percentage increases in mass transfer rates with inclusion fibers in channel geometries ( $d_{ch} = 400 \mu m$ ,  $(d_{ch}/d_f) = 40$  and  $FV = 1.57\%$ )**

Fig 6.19 shows the percentage increase in mass transfer rates for the open channel geometry with flat velocity profiles over that with parabolic velocity profiles (equation 6.28). This data was also compared with the percentage increase in mass transfer rate in a specific fiber channel geometry ( $d_{ch}/d_f = 80$  and fiber volume  $= 1.57\%$  and  $a/b = 1.5$ ). This fiber geometry was chosen as it showed the maximum increase in mass transfer rates. The mass transfer rates for both the cases shown are more or less equal for most of the  $Re$  and  $Sc$  ranges. This shows that the presence of fibers (inert structures) in the fluid flow paths can help achieve plug-flow like conditions. For the highest  $Re$  and  $Sc$  the fiber

channel was found to be even better than that in open channel with flat velocity profile. This is possible as the preferential flow of fluid near the wall in high  $a/b$  fiber channels can lead to mass transfer rates even higher than that in plug flow conditions.

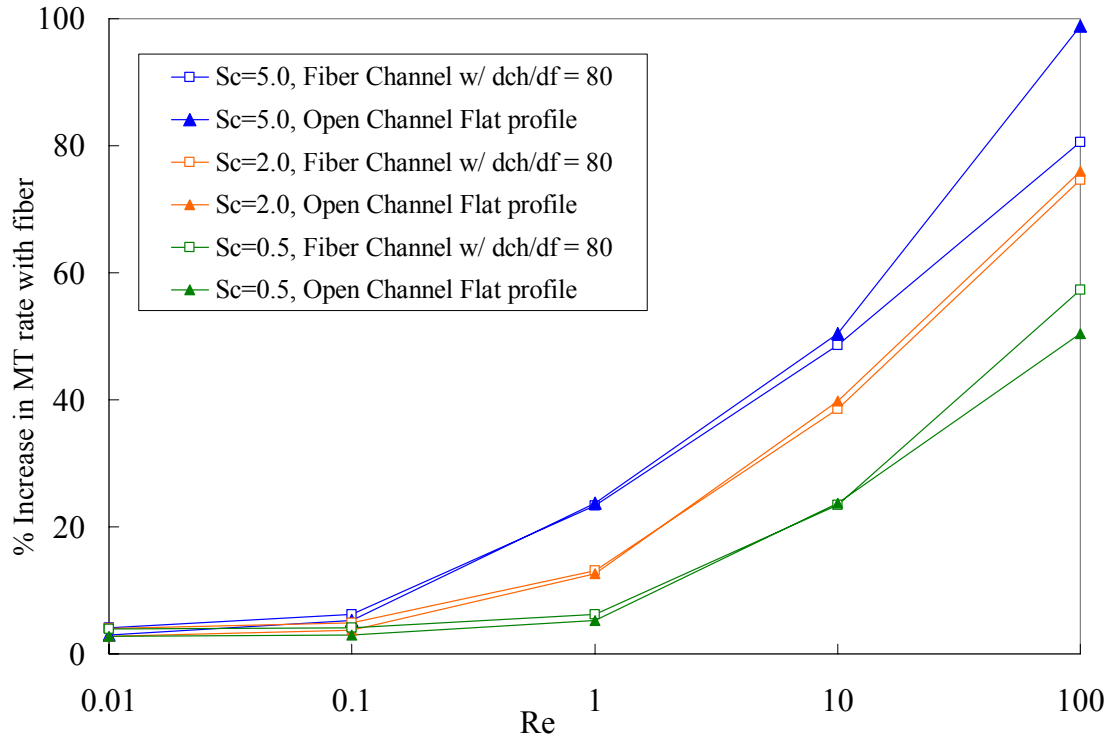


**Fig. 6.19. Percentage increase in mass transfer rates in open channels with flat velocity profiles and comparisons with that in a specific fiber channel geometry ( $d_{ch}/d_f = 80$ ,  $FV = 1.57\%$  and  $a/b = 1.5$ ).**

Fig. 6.20 shows the  $H_2S$  and Hexane data from Fig. 6.10 along with the data points for the same systems obtained from the results of dimensionless variable study (Fig 6.16). Since both the data points match very well the dimensionless number study is verified and can be used to predict results in these 2D geometries for any reaction/adsorption system of interest.

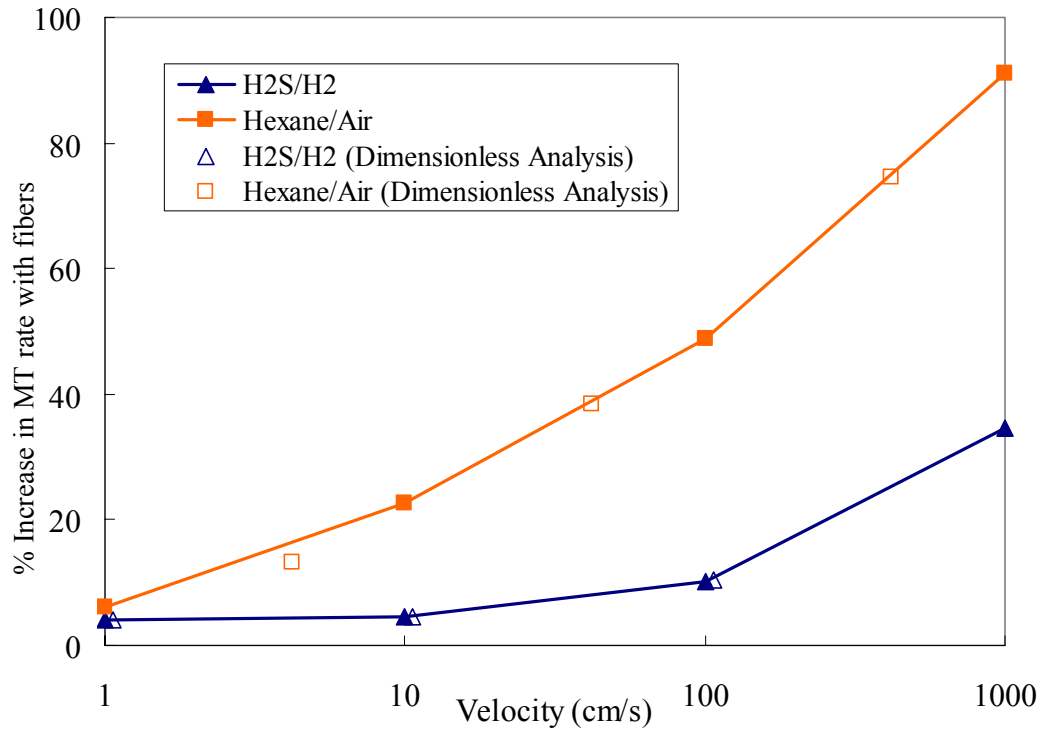


**Fig. 6.20. Percentage increases in MT rates for H<sub>2</sub>S/H<sub>2</sub> and Hexane/Air systems for various velocities ( $d_{ch} = 400 \mu m$ ,  $(d_{ch}/d_f) = 40$ ,  $FV = 1.57\%$  and  $(a/b) = 1.5$ ), as obtained using direct simulations and also using the results from dimensionless analysis study.**

As diffusivity and velocity occur either in  $Sc$  or  $Re$  alone and not in both, the effects of these variables can be easily interpreted from Fig. 6.14 - 6.20. But, viscosity and density both occur in  $Sc$  as well as  $Re$  and hence the exact effect of these variables is not so obvious in the above results. In order to understand the effect of density on mass transfer rates,  $Sh$  for two different gas densities in the open channel geometry are plotted in Fig. 6.21 with all the other physical quantities (variables) kept constant. This data was obtained from the earlier results of Fig. 6.15. The results for both the densities nearly overlap one another. Similar results were also obtained with density variation in all the fiber channel geometries. This signifies that the mass transfer rates are almost



independent of the density variations for the conditions examined in this study. An increase in density increases  $Re$  (tends to increase MT rate) but it also decreases  $Sc$  (tends to decrease MT rate), these effects more or less cancel each other and hence the resultant effect of density on mass transfer rates is almost negligible.

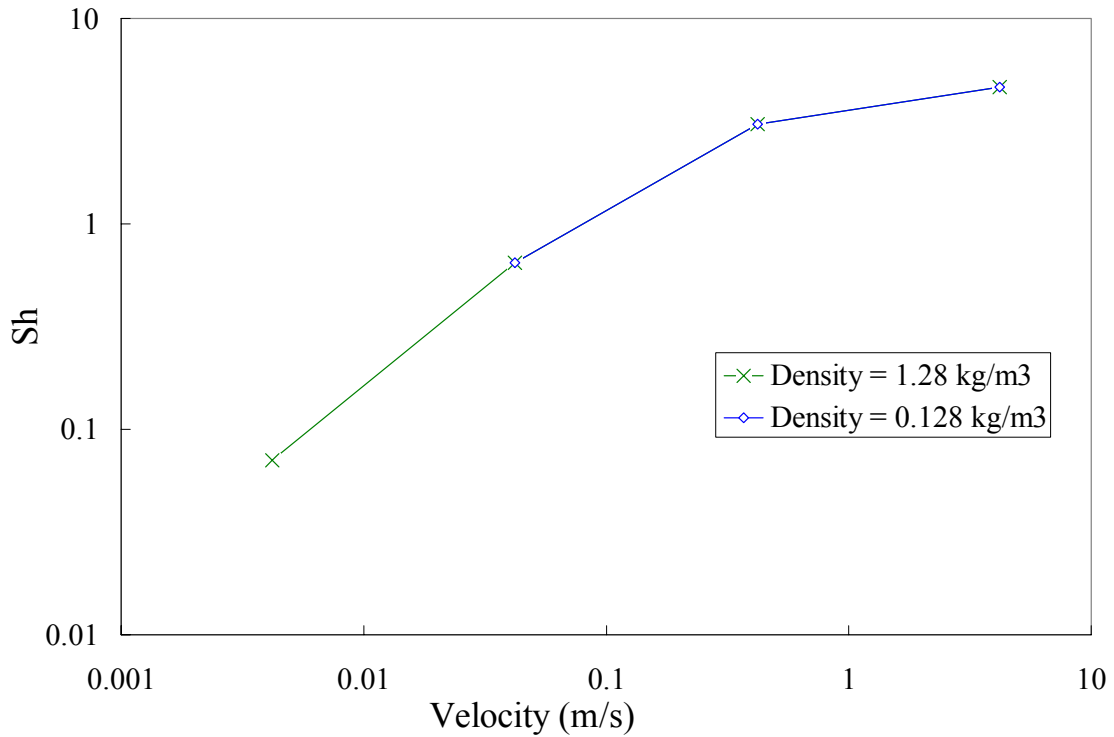


**Fig. 6.21.  $Sh$  versus velocity for two different gas densities in the open channel geometry with rest of the physical quantities kept constant.**

Fig 6.22 shows the  $Sh$  variation in a fiber channel geometry for two different viscosities as calculated from the results obtained in dimensionless analysis before (Fig. 6.15). Similar results were also obtained for the open channel geometry. Hence, like density, viscosity of the gas stream also seems to have very weak or almost no effect on the mass transfer rates for the conditions used in this study. Similar explanation as that given for density variation can also be given for the negligible effect of viscosity

variation on mass transfer rates. These observations are in agreement with traditional mass transfer models for fluid solid contacting systems which predict a very weak dependence of mass transfer rates on viscosity ( $k_m \propto \mu^0 \sim \mu^{1/6}$ ) as well as fluid density ( $k_m \propto \rho^0 \sim \rho^{-1/6}$ ) for laminar flows[6.1].

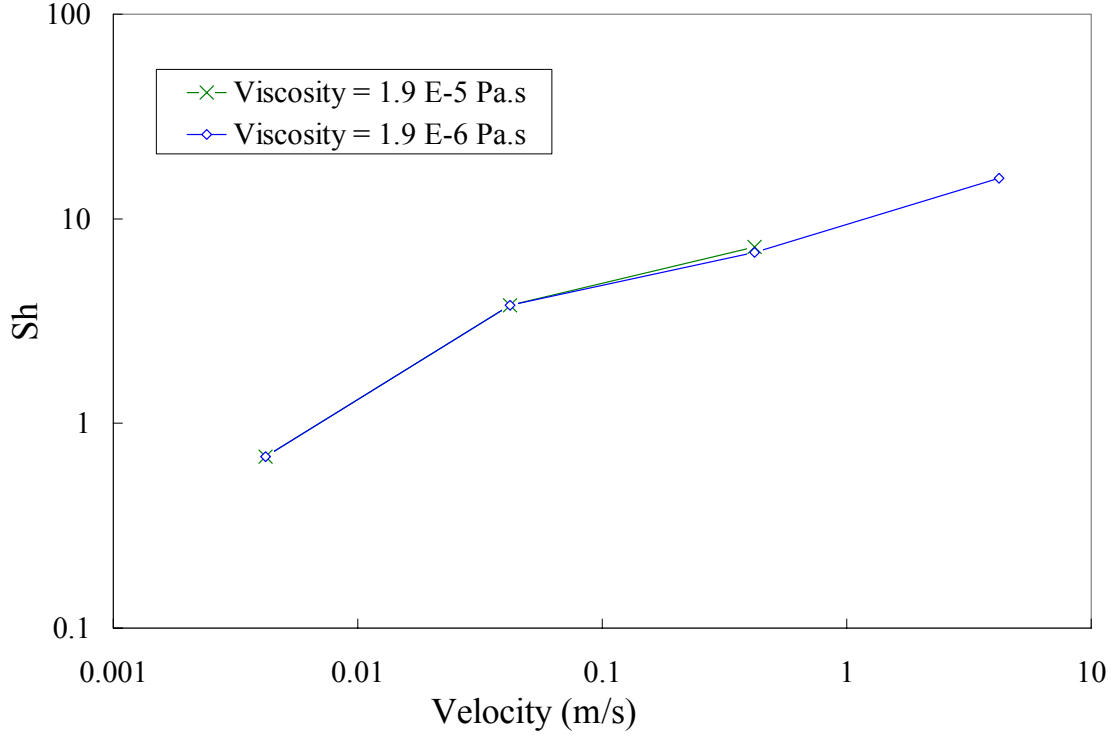


**Fig. 6.22. Sh vs velocity for two different gas viscosities in a fiber channel geometry ( $d_{ch} = 400 \mu m$ ,  $(d_{ch}/d_f) = 40$ ,  $FV = 1.57\%$  and  $(a/b) = 1.5$ ) with rest of the physical quantities kept constant.**

## VI. 5.2. Static Mixing Study

As described before the static mixing efficiency of the fibers in MFECS was examined by analyzing the extent of mixing (COV) of two different gas streams in fiber and open geometries. The x-velocity and the component A concentration contours for the flow

conditions and geometries described in section VI.3.2 are shown in Fig. 6.23 and 6.24, respectively. The concentration contours look very similar. Fig. 6.25 shows the concentration profiles in the outlet planes of the fiber and open geometries. These profiles overlap each other, signifying almost equal extent of mixing in both the geometries.

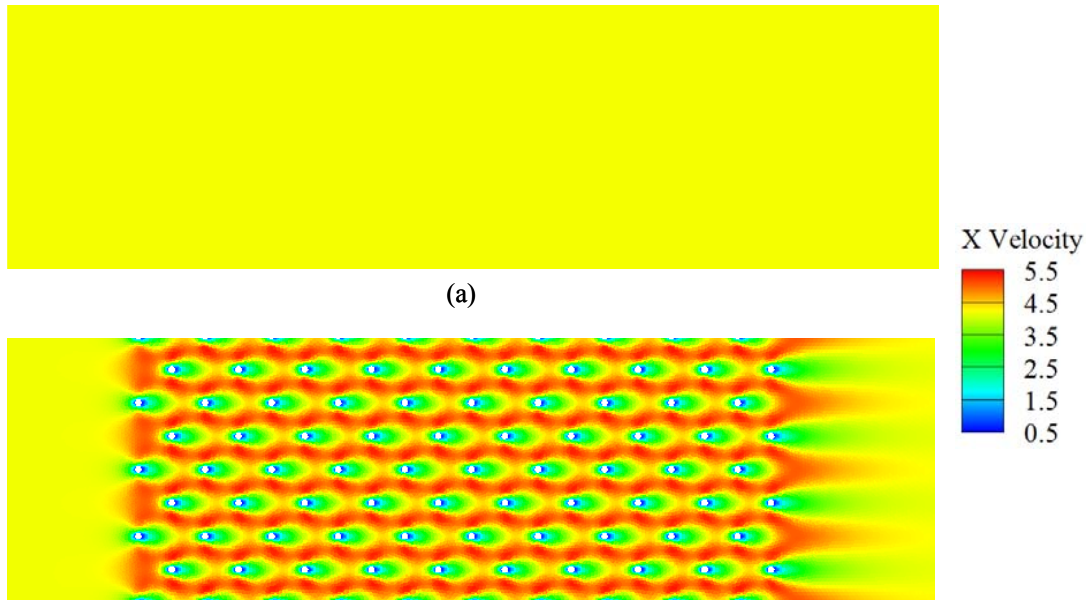


**Fig. 6.23. velocity profiles for simulations demonstrating the extent of mixing for an open and a fiber geometry.**

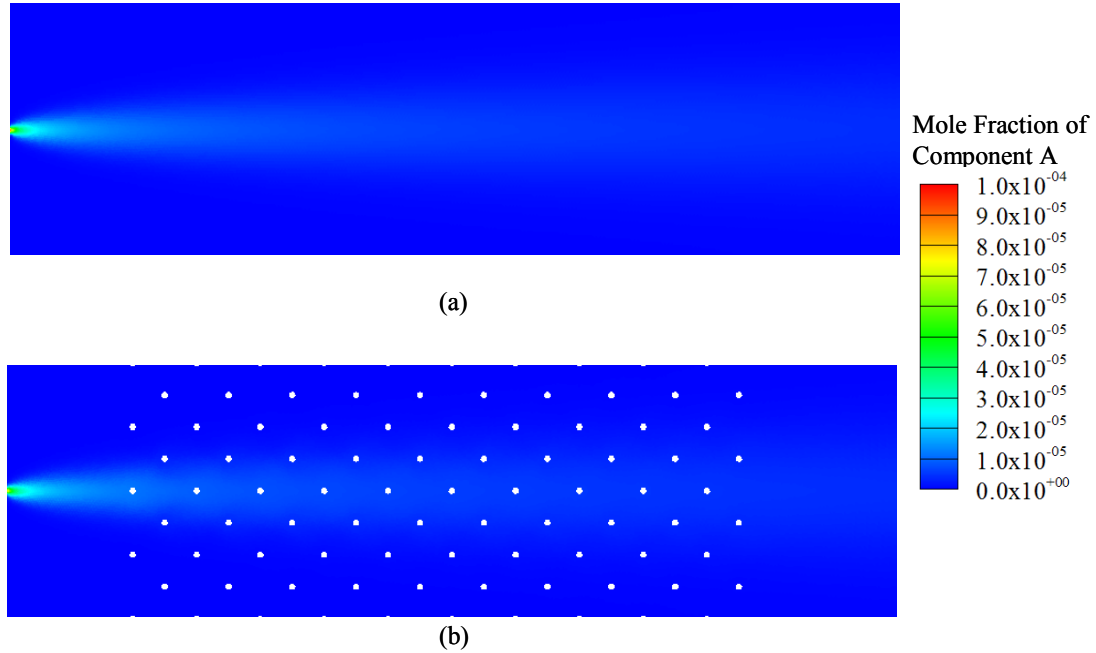


**Fig. 6.24. Concentration profiles showing the extent of mixing for an open and a fiber geometry.**

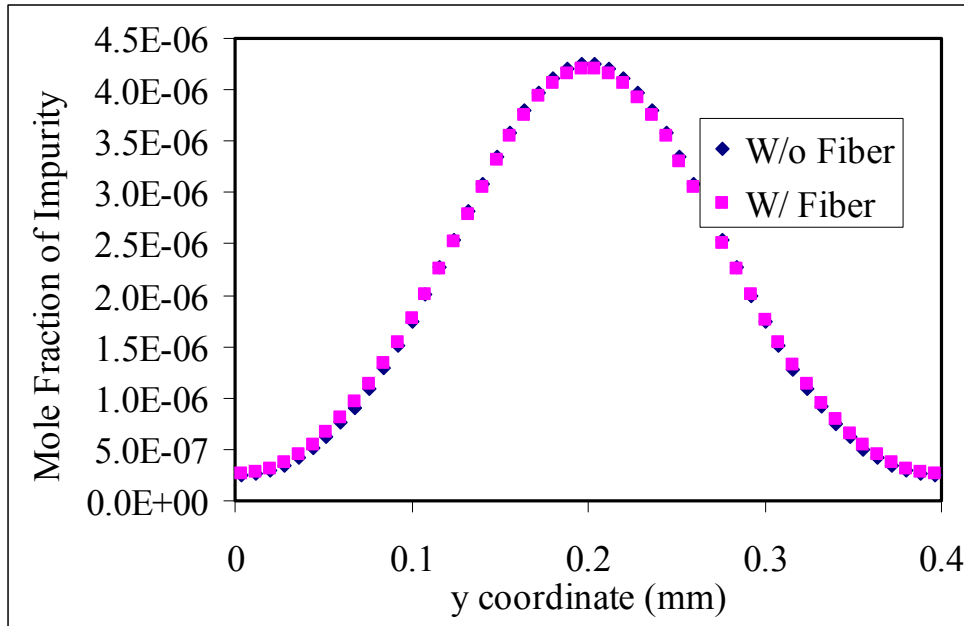


**Fig. 6.25. Concentration profiles in the outlet planes of fiber and open geometries.**

Further, the COV values were calculated for the concentrations on the outlet planes. These values are presented in Table 6.6, which are almost identical for open and

fiber geometries. This further confirms that the extent of mixing is almost independent of the fiber presence even for the highest velocities (tested in the mass transfer study). Therefore, it can be safely said that static-mixing does not play any role in the enhancement of mass transfer rates seen in the previous section. This implies that the elimination of the parabolic velocity profiles is the only reason for observed enhancement in mass transfer rates in fiber channels (MFECS).

**Table 6.6. COV values for fiber and open geometries.**

	<b>With Fibers</b>	<b>Without Fibers</b>
<b>COV</b>	<b>0.9002</b>	<b>0.8982</b>

## **VI. 6. Conclusions**

Fibers (inert structures), if present in the fluid path in fluid-solid contacting systems, can have a significant effect on the mass transfer rates depending on Re and Sc of the problem. The extent of this effect of the fibers was found to be dependent on multiple factors like velocity, diffusivity, fiber diameter, channel diameter, fiber diameter, fiber volume percentage and fiber distribution inside the channel. For the conditions of this study, viscosity and density of the gas mixture were found to have almost no influence on the gas phase mass transfer rates, whereas increase in channel diameter, increase in velocity, decrease in diffusivity, decrease in fiber diameter, increasing ‘a/b’ ratio were found to have a positive influence on the percentage increase in mass transfer rates due to fibers. The increase in fiber volume fraction had mixed effects on the mass transfer rates. This enhancement in mass transfer rates resulting from the presence of fibers was found to be due to the elimination of parabolic velocity

profiles which would otherwise be present in open channel geometries. The effect of static mixing of fibers was found to be almost negligible for the flow conditions used in this study and those of interest for MFECS applications.

## **VI.7. Nomenclature**

$a$  = Distance between the wall and nearest row of fibers (m)

$b$  = Distance between the consecutive fiber rows (m)

$C_A$  = Concentration of A (ppmv or mol/m<sup>3</sup>)

$C_{Ai}$  = Concentration of A at location  $i$  (ppmv or mol/m<sup>3</sup>)

$C_{AM}$  = Mean concentration of A (ppmv or mol/m<sup>3</sup>)

$C_{A0}$  = Inlet concentration of A (ppmv or mol/m<sup>3</sup>)

COV = Coefficient of variation

$D_{AB}$  = Diffusion coefficient (m<sup>2</sup>/s)

$d_{ch}$  = Channel width (m)

$d_f$  = Fiber diameter (m)

$f$  = Friction factor

$f_i$  = Function value at a grid level  $i$  ( $i=1, 2$  and  $3$ )

Kn = Knudsen number

$k_m$  = Mass transfer coefficient (m/s)

$L$  = Length of the channels

$M$  = Molecular weight (g/gmol)

$m$  = Total number of grid points in the outlet

$N_i$  = Number of grid points at grid level  $i$  ( $i = 1, 2$  and  $3$ )

$n$  = Number of spatial dimensions (for 2D,  $n = 2$ )

$p'$  = Formal order of accuracy

$p''$  = Observed order of accuracy

$p$  = Pressure (Pa)

$\frac{\Delta P}{L}$  = Pressure drop across unit length of the bed (Pa/m)

$R$  = Gas constant (J/mol/K)

$Re$  = Reynolds number

$r$  = Grid refinement factor or radial (or normal) coordinate

$Sc$  = Schmidt number

$Sh$  = Sherwood number

$T$  = Temperature (K)

$T_0$  = Inlet Temperature (K)

$U$  = Velocity component parallel to wall (m/s)

$U_w$  = Wall velocity (m/s)

$U_s$  = Fluid slip velocity (m/s)

$\frac{\partial U}{\partial n}$  = Tangential velocity gradient normal to the surface (1/s)

$u_0$  = Inlet Velocity (m/s)

$\vec{V}$  = Velocity vector  $\left(\vec{V} = u \hat{i} + v \hat{j} + w \hat{k}\right)$  (m/s)

$x$  and  $y$  = Cartesian coordinate system axes (m)

Symbols

$\vec{\nabla}$  = Gradient operator

Greek letters

$\varepsilon$  = Void fraction (ratio of the volume of all the voids in a material to the total volume)

$\phi_i$  = Shape factor of  $i^{\text{th}}$  material

$\mu$  = Viscosity (kg/m/s)

$\rho$  = Fluid Density (kg/m<sup>3</sup>)

$\sigma$  = Variance

$\sigma_{\text{max}}$  = Maximum value of  $\sigma$

$\sigma_v$  = Tangential momentum accommodation coefficient

$\tau_{xx}, \tau_{yy}$  = Normal stress (N/m<sup>2</sup>)

$\tau_{xy}, \tau_{yx}$  = Shear stress (N/m<sup>2</sup>)



## **CHAPTER VII**

### **CONCLUSIONS & RECOMENDATIONS FOR FUTURE WORK**

#### **VII.1 Conclusions**

Conclusions from each of the individual studies are presented at the end of the respective chapters. An overview of all the factors studied and inferences obtained in this work is mentioned here. Theoretical as well as experimental comparisons of MFECS were made with the conventional reactor systems. Various factors which result in enhancement in contacting efficiency (higher mass transport rates and lower pressure drops) in MFECS were explored and quantified. These factors include:

(i) Uniformity and high voidages:

Hexane adsorption breakthrough tests demonstrated the significant influence of channeling in packed beds. This negative influence was successfully eliminated in MFECS structures with help of uniformity and high voidages inherently present in this materials. This was shown to significantly improve breakthrough times and adsorbent utilizations in MFECS compared to packed beds.

(ii) Composite bed designs:

A composite bed design which used thin MFECS layers in series with packed beds was shown to combine the advantages of high capacity of packed beds and high efficiency of the microfibrous materials.

(iii) Pleated structures:

Pleated structures of MFECS were shown to significantly benefit from lower effective velocities, which enable lower pressure drops as well as higher residence times which in turn lead to higher conversions. This was demonstrated using mathematical models and experimental data for a high throughput (flow rate) application - ozone decomposition for aircraft cabin air purification application. Comparisons with monoliths and packed beds showed MFECS with pleat factors above four outperformed all the other conventional reactors.

(iv) Effect of fibers:

CFD simulations in simple 2D channels were used to demonstrate the effect of fibers in reducing the parabolic velocity peaks and hence achieving uniform (plug flow) velocity profiles which give higher conversions. Significant enhancement in mass transfer rates were observed with inclusion of fibers in channel geometries. The effect of various variables like velocity, diffusivity, viscosity, density, fiber diameter, etc. on mass transfer rates in fiber geometries was successfully analyzed with help of a dimensionless variable study. Static mixing was shown to have no significant effect on the fluid-wall mass transfer coefficients in channel geometries.

## **VII.2. Recommendations for Future Work**

### **VII.2.1. Optimization of MFEC/MFES Structures**

With the help of the analysis from the two case studies (hexane breakthrough tests and ozone decomposition) used in this research, optimization of MFEC/MFES structures (i.e. their internal dimensions such as voidage, particle diameters, fiber diameters, etc.)

can be sought. This would be critical to make the best use of these novel structures. From the results in the theoretical comparisons for the ozone converter study it can be seen that there would be a further improvement in effective reaction rates with decreasing particle sizes in the MFEC as that could further lower the transport resistances. Also the effect of voidage on the pressure drops can be further investigated. These issues to some extent are also dependent on the limitations from a practical standpoint of media preparation. So an optimum based on the theoretical analysis and practical feasibility needs to be found.

The optimum structural dimensions might vary with kinetics, heat of reactions involved and operating conditions of the application. Many prior studies involving MFEC like CO oxidation in air, preferential oxidation of CO in reformat streams, etc. exhibited improved rates. The reaction rates for some of these reactions involve negative orders of reactant concentrations and also involve selectivity issues. The results from the theoretical overall performance comparisons of various reactor types for a first order reaction in the ozone study was very much in line with the experimental observations and hence this could be further extended to cases with non linear kinetics. The internal effectiveness factors for reactions with negative and/or fractional order kinetics could be more than one. In a situation like this the effect of reactor geometry on the effective reaction rates could be an interesting aspect to study. Selectivity based evaluation of the reactors will be made for cases with multiple reactions occurring simultaneously. A study of how the reactor geometry can influence the selectivity of a system with multiple reactions occurring in series and/or parallel can be attempted.

Also the above mentioned CO oxidation applications and many other potential applications of MFEC involve highly exothermic reactions. The heat transfer effects or

ignition-extinction behavior for a non-isothermal case could be incorporated into the comparative study. The performance evaluation criteria for a situation involving heat transfer effects might be different than that used in ozone case study presented before. The definition may involve entropy minimization which is most widely used in the heat exchanger designs.

### **VII.2.2. Reasons for Increased Flow Mal-distributions in Small Particle Beds**

Hexane breakthrough experiments have shown that there is considerable influence of flow mal-distributions on the effective mass transport rate to the solid surface especially with small particle beds. The reason for the increased flow mal-distributions in small particle beds has been attributed to particle clustering. But as mentioned earlier the causes for this increased clustering effect in small particle beds are not clear. One potential reason could be in small particle beds the asperities or the roughness on the particle surface is in the range of particle dimension. This could lead to particles interlocking with each other which could in turn cause cluster formation.

Another reason for flow mal-distributions apart from clustering could be high pressure drops in small particle beds which increase the tendency of fluid flowing through bed to widen any existing non-uniformities or flow by-passes in the bed which can increase channeling through them. The small size of the particles also helps any internal rearrangement of the particles that the flowing fluid tends to create in order to widen the existing non-uniformities in bed. Which of these above listed factors is playing a major role in creating flow mal-distributions is yet to be determined. Some of the

experiments and theoretical (CFD) analysis that can be used to understand the factors leading to flow mal-distributions will be described further.

### **VII.2.3. Experiments Involving Spray Dried Spherical Particles**

Spherical particles of a very narrow size range can be made by using spray drying techniques. Catalytic reaction/adsorption breakthrough tests with these uniform size particles can help understand the effects of particle shapes on flow mal-distributions. Experiments can be run with varying particle sizes and varying particle dilutions and comparisons can be made with MFEC/MFES similar to that made in the studies before. Also all of these experimental variations can be conducted with crushed and sieved (irregularly shaped) particles of the same materials. Comparisons of the axial dispersion coefficients obtained from the spherical particle beds with the corresponding results obtained from irregularly shaped particles can be made. This will help determine if the asperity of the irregularly shaped particles leads to particle clustering and thereby flow maldistributions.

### **VII.4. Bed Voidage variations using capillary Tubes**

The variations in the voidage of packed beds could be achieved by using narrow capillary tubes as reactors. The diameters of the tubes would be in the range of a couple of particles diameters or less. By varying tube to particle diameter ratios (by either changing particles sizes or tube diameters) the effective voidages can be affected. Voidages of up to 70% can be achieved in this method using spherical particles packed in cylindrical and/or square channels. Axial dispersion coefficients and effective reaction

rates can be found from experimental studies for various bed voidages created by this method. Although these voidages are not as high as typical MFEC voidages they can give some insight into the effect of bed voidage on the transport coefficients.

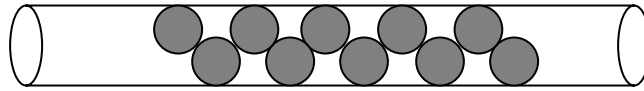


**Fig. 7.1 Small tube to particle diameters can be used to achieve varying voidages**

#### **VII.2.4. MFEC Ozone Converter Tests**

Ozone conversion and pressure drops of MFEC structures with various pleat factors, various particle and fiber diameters and voidages can be measured, while the higher pleat factors and higher voidages can be used to reduce pressure drops. Particle size variations can be used to understand and enhance the mass transport rates. Monoliths of various cpsi, wall thicknesses and catalyst washcoating thicknesses can be tested. If possible, variations of packed beds with different catalyst particle sizes can also be tested. Different catalysts (precious metals and metal oxides) can be tested for reaction rates. With this approach an improvement in surface reaction rates can be targeted. The catalyst life under practical operating conditions can be tested. The effect of contacting system (monolith, packed bed or MFEC) on the life of catalyst can be studied

Commercial ozone converters also remove some additional pollutants like common Volatile Organic Compounds (VOCs) found in the airport environments. VOC removal by catalytic oxidation has other applications like power plant exhaust gases

treatment. So, VOC oxidation tests can also be conducted on pleated MFEC structures separately or in parallel with the ozone decomposition.

#### **VII.2.5. CFD Analysis**

Initial results using CFD tools for understanding the flow fields in the MFEC have shown great benefits. The experimental determination of mass/heat transfer coefficients for small particle beds is difficult owing to the high transport rates, which make them more sensitive to errors involved in experimental measurements. Also CFD simulations for determining heat transfer/ mass transfer coefficients are easy compared to the experiments and could provide ample insight into the problem.

The effect of flow maldistributions can be simulated using CFD particle cluster models, in which a group of catalyst/adsorbent particles are placed closer to each other than to the other adjacent particles. This could be compared with a packed bed with uniformly placed particles. The difference in the effective reaction rates between these two cases could be used to estimate the effective axial dispersion coefficients resulting from particle clustering.

Further, CFD simulations can be used for a heat transfer study aimed at analyzing exothermic reactions. The effect of heat transfer rates and multiple steady state phenomena can be determined using CFD. The effect of high intra-bed conductivities due to metal fibers used in the MFEC can also be explored. The analogy between heat and mass transport could also be utilized in extending the results from a heat transfer study to mass transfer case and vice versa.

## REFERENCES

- [1.1] B.J. Tatarchuk, M.R. Rose, A. Krishnagopalan, J.N. Zabasajja, D. Kohler, US Patent 5 080 963.
- [1.2] B.J. Tatarchuk, US Patent 5 096 663.
- [1.3] B.J. Tatarchuk, M.F. Rose, A. Krishnagopalan, US Patent 5 102 745.
- [1.4] B.J. Tatarchuk, M.F. Rose, G.A. Krishnagopalan, J.N. Zabasajja, D.A. Kohler, US Patent 5 304 330.
- [1.5] B.K. Chang, Y. Lu and B. J. Tatarchuk, Chem. Eng. J., 115 (2006) 195.
- [1.6] B.K. Chang, Y. Lu, H. Y. Yang, and B. J. Tatarchuk, J. of Mtrls. Eng. & Performance, 15 (2006) 439.
- [1.7] Y. Lu, H.Y. Yang, B.K. Chang, and B.J. Tatarchuk, ACS Symp. Series 914, Microreactor Technology and Process Intensification, Washington DC, 7-11Sept., (2003) paper No. 25.
- [1.8] B.K. Chang, Y. Lu, H. Y. Yang, and B. J. Tatarchuk, J. of Mtrls. Eng. & Performance, 15 (2006) 453.
- [1.9] M.W. Meffert, Preparation and characterization of sintered metal microfiber-based composite materials for heterogeneous catalyst applications, Ph.D. Dissertation, Auburn University, Auburn, AL, 1998.



- [1.10] A.P. Queen, High Efficiency adsorption filters via packed bed + polishing sorbent architectures for regenerable collective protection equipment, Masters Thesis, Auburn University, Auburn, AL, 2005.
- [1.11] D.R. Cahela and B. J. Tatarchuk, *Catalysis Today*, 69 (2001) 33.
- [1.12] D.K. Harris, D.R. Cahela and B.J. Tatarchuk, *Composites Part A: App. Sci. & Manufacturing*, 32 (2001) 1117.
- [1.13] O. Levenspiel, *Chemical Reaction Engineering*, 3<sup>rd</sup> ed, John Wiley and Sons, Inc., New York, 1999.
- [1.14] H. S. Fogler, *Elements of Reaction Engineering*, 3<sup>rd</sup> ed, Prentice Hall PTR, New Jersey, 1999.
- [1.15] R. M. Heck and R. J. Farrauto, *Catalytic Air Pollution Control: Commercial technology*, Van Nostrand Reinhold, New York, 1995.
- [1.16] *Encyclopedia of Environmental Control Technology*, Vol.1, Gulf Publishing Co. , 1989.
- [1.17] R.M. Heck, S.Gulati, R.J. Farrauto, *Chem. Eng. J*, 82 (2001) 149.
- [1.18] Cybulski and J.A. Moulijn, *Catalysis Reviews: Science and Engineering*, 36 (1994) 179.
- [1.19] J. Villiermaux and D. Schweich, *Ind. Eng. Chem. Res.* 33 (1994) 3025.
- [1.20] K.E. Voss, J.C. Dettling, S. Roth, R. Kakwani, Y.K. Lui, A. Gorel, G.W. Rice, US Patent No 7 078 004
- [1.21] J.T. Richardson, Y. Peng and D. Remue, *Applied Catalysis A: General* 204 (2000) 19.

- [1.22] J. T. Richardson, D. Remue and J. K. Hung Applied Catalysis A: General 250, (2003) 319.
- [1.23] Y. Peng and J. T. Richardson, Applied Catalysis A: General, 266 (2004) 235.
- [1.24] A.Y. Tonkovich, S. Perry, Y.Wang, D. Qiu, T. LaPlante, W.A. Rogers, Chem. Eng. Sci., 59 (2004) 4819.
- [1.25] Y. Tonkovich, J. L. Zilka, M. J. LaMont, Y. Wang and R. S. Wegeng, Chem. Eng. Sci., 54 (1999) 2947.
- [1.26] J.L. Hu, Y. Wang, D. VanderWiel, C. Chin, D. Palo, R. Rozmiarek, R.Dagle, J. Holladay, E. Baker, Chem. Eng. J., 93 (2003) 55.
- [1.27] H. Pennemann, V. Hessel and H. Löwe, Chem. Eng. Sci., 59 (2004) 4789.
- [1.28] K. F Jensen, ACS Symp. Series 914, Microreactor Technology and Process Intensification, Washington DC, 7-11Sept., (2003) paper No. 1.
- [1.29] P. D. I. Fletcher, S. J. Haswell, E. Pombo-Villar, B. H. Warrington, P. Watts, S.Y. F. Wong and X. Zhang, 58 (2002) 4735.
- [1.30] K. F. Jensen, Chem. Eng. Sci., 56 (2001) 293.
- [1.31] Z. D. Jiang, J. S. Chung, and G. R. Kim, Chem. Eng. Sci. 58 (2003) 1103.
- [1.32] D. Kunii and O. Levenspiel, Fluidization Engineering, 2<sup>nd</sup> ed., Butterworth-Heinemann, Boston, 1991.
- [1.33] P. N. Dwivedi and S. N. Upadhyay, Ind. Eng. Chem., Process Des. Dev., 16, (1977) 157.
- [1.34] V.Balakotaiah and S.M.S.Dommeti, Chem. Eng., Sci.,54 (1999) 1621.
- [1.35] E.Tronconi, A. Beretta, Catalysis Today, 52 (1999) 249.
- [1.36] P Fedkiw and J Newman, Chem Eng. Sci., 33 (1977) 1043.

- [1.37] N. Wakao, S. Kaguei and H. Nagai, Chem. Eng. Sci., 33 (1978) 183.
- [1.38] H Martin, Chem. Eng. Sci., 33 (1978) 913.
- [1.39] N Wakao and S Tanisho, Chem. Eng. Sci., 29 (1974) 1991.
- [1.40] S.S.E.H. Elnashaie, and S.S. Elshishini , Dynamic Modeling, Bifurcation and Chaotic Behavior of Gas-Solid Catalytic Reactors, Gordon and Breach Science Publishers, London, 1996.
- [1.41] M Suzuki and JM smith, Chem. Eng. J., 3 (1972) 256.
- [1.42] N. Wakao, T. Funazkri, Chem. Eng. Sci., 33 (1978) 1375.
- [1.43] G. Langer, A. Roethe, K. P. Roethe and D. Gelbin, Int. J. Heat mass Transfer, 21 (1978) 751.
- [1.44] D. M. Ruthven, Principles of Adsorption and Adsorption processes, New York: John Wiley and Sons, Inc., 1984, p. 209.
- [1.45] E. Tsotsas, Chem. Eng. and Processing, 31 (1992) 181.
- [1.46] G. Rexwinkel, A.B.M. Heesink and W.P.M. Van Swaaij, Chem. Eng. Sci., 52 (1997) 3995.
- [1.47] M. Winterberg and E. Tsotsas, AIChE J., 46 (2000) 1084.
- [1.48] A. Klerk, AIChE J., 49 (2003) 2022.
- [1.49] Subagyo, N. Standish and G.A. Brooks, Chem. Eng. Sci., 53 (1998) 1375.
- [1.50] M.M.J. Quina and R.M.Q. Ferreria, Chem. Eng. J., 75 (1999) 149.
- [1.51] T. Valdés-Solís, M. J. G. Linders, F. Kapteijn, G. Marbán and A. B. Fuertes, Chem. Eng. Sci., 59 (2004) 2791.
- [1.52] J.L. Williams, Catalysis Today, 69 (2001) 3.
- [1.53] M. F. Edwards and J. F. Richardson, Chem. Eng. Sci., 23 (1968) 109.

- [1.54] C. Akosman and J.K. Walters, Chem. Eng. Process., 43 (2004) 181.
- [1.55] R. Aris, Chem. Eng. Sci., 9 (1959) 266.
- [1.56] J.T. Richardson, Principles of catalyst development, Plenum press, New York, 1989.
- [1.57] J. D. Anderson, Computational Fluid Dynamics: The Basics with Applications, McGraw-Hill, New York, 1995.
- [1.58] S. Middleman, An Introduction to Fluid Dynamics: Principles of Analysis and Design. 2<sup>nd</sup> ed., Wiley, New York, 1998.
- [1.59] Anderson, D.A., Tannehill, J.C., Pletcher, R.H., Computational fluid mechanics and heat transfer, Mc Graw Hill, 1984.
- [1.60] H. P. A. Calis, J. Nijenhuis, B. C. Paikert, F. M. Dautzenberg, C. M. van den Bleek, Chemical Engineering Science 56 (2001) 1713.
- [1.61] M. Nijemeisland, A. G. Dixon, E. H. Stitt, Chem. Eng. Sci. 59 (2004) 5185.
- [1.62] A. Guardo, M. Coussirat, F. Recasens, M.A. Larrayoz, X. Escaler, Chem. Eng. Sci. 61 (2006) 4341.
- [1.63] A. Guardo, M. Coussirat, M.A. Larrayoz, F. Recasensa, E. Egusquiza, Chem. Eng. Sci. 60 (2005) 1733.
- [1.64] M. Masood, M.M. Ishrat, A.S. Reddy, International Journal of Hydrogen Energy 32 (2007) 2539.
- [1.65] A. Mohammadi, M. Yaghoubi and M. Rashidi, Intl. Comm. in Heat and Mass Trans., (2007), in press.
- [1.66] P. Canu and S. Vecchi, AIChE Journal Vol. 48 (2002) 2921
- [1.67] V. P. Zakharov, I. A. Zolotarskii, V. A. Kuzmin, Chem. Eng. J. 91 (2003) 249

- [1.68] A. G'omez, N. Fueyo and A. Tom, Comput. Chem. Eng. 31 (2007) 1419.
- [1.69] R. Farmer , R. Pike and G. Cheng, Comput. and Chem. Eng. 29 (2005) 2386.
- [1.70] D. A. Colman, Petroleum tech quaterly, 4 (1999) 75.
- [1.71] K. Fouhy, Chem. Eng., Nov (1999) 178.
- [1.72] J. T. Adeosun and A. Lawal, Sens Actuators B 110 (2005) 101.
- [1.73] M.N. Kashid, D.W. Agar and S. Turek, Chem. Eng. Sci. 62 (2007) 5102.
- [1.74] M. Engler, N. Kockmann, T. Kiefer, Peter Woias Chem. Eng. J. 101 (2004) 315.
- [1.75] D.M, Hobbs, F.J. Muzzio, Chem. Eng. J. 70 (1998) 93.
- [1.76] J. Z. Fang, D. J. Lee, Chem. Eng. Sci., 56 (2001) 3797.
- [1.77] [http://en.wikipedia.org/wiki/Finite\\_volume\\_method](http://en.wikipedia.org/wiki/Finite_volume_method)
- [1.78] <http://math.nist.gov/mcsd/savg/tutorial/ansys/FEM/>
- [1.79] <http://www.solid.ikp.liu.se/fe/index.html>
- [1.80] <http://www.nae.edu/nae/bridgecom.nsf/weblinks/MKEZ-5HUM3J?OpenDocument>
- [1.81] C. J. Roy, J. of Computational Physics, 205 (2005) 131.
  
- [2.1] T. C. Ho and B. S. White, Chem. Eng. Sci., 46 (1991) 1861.
- [2.2] R. J. Berger, J. Pérez-Ramírez, F. Kapteijn and J. A. Moulijn, Chem. Eng. J., 90 (2002) 173.
- [2.3] Rob J. Berger, Javier Pérez-Ramírez, Freek Kapteijn and Jacob A. Moulijn Chem. Eng. Sci., 57 (2002) 4921.
- [2.4] R. J. Berger, J. Pérez-Ramírez, F. Kapteijn and J. A. Moulijn, Applied Catalysis A: General, 227 (2002) 321.

- [2.5] C.T. Hsieh and J.M. Chen, J of Colloid and Interface Sci., 255 (2002) 248.
- [2.6] D. M. Ruthven, Principles of Adsorption and Adsorption processes, New York: John Wiley and Sons, Inc., 1984, p. 209.
- [2.7] R. Pfeffer, I&EC Fundamentals, 3 (1964) 380.
- [2.8] C. Tien, Adsorption Calculations and Modeling, Butterworth-Heinemann, 1994, p. 78.
- [2.9] A. Klerk, AIChE J., 49 (2003) 2022.
- [2.10] A. Gupta, V. Gaur and N. Verma, Chem. Eng. and Processing, 43 (2004) 9.
- [2.11] R.J. Berger, J. Ramirez, F. Kapteijn and J.A. Moulijn, Chem. Eng. J., 90 (2002) 173.
- [2.12] C. Akosman and J.K. Walters, Chem. Eng. Process., 43 (2004) 181.
- [2.13] G. Langer, A. Roethe, K. P. Roethe and D. Gelbin, Int. J. Heat mass Transfer, 21, (1978) 751.
- [2.14] E. Tsotsas, Chem. Eng. and Processing, 31 (1992) 181.
- [2.15] G. Rexwinkel, A.B.M. Heesink and W.P.M. Van Swaaij, Chem. Eng. Sci., 52 (1997) 3995.
- [2.16] H Martin, Chem. Eng. Sci., 33 (1978) 913.
  
- [3.1] H. Yang, Gas phase desulfurization using regenerable microfibrinous entrapped metal oxide based sorbents for logistic fuel cell applications, Ph.D. Thesis, Auburn University, Auburn, AL, 2007.

- [3.2] A.P Queen, High Efficiency adsorption filters via packed bed+ polishing sorbent architectures for regenerable collective protection equipment, Masters Thesis, Auburn University, Auburn, AL, 2005.
- [5.1] R. M. Heck and R. J. Farrauto, Catalytic Air Pollution Control: Commercial technology, Van Nostrand Reinhold, New York, 1995.
- [5.2] J. D. Spengler, S. Ludwig and R. A. Weker, Indoor Air, 14 (2004) 67.
- [5.3] National Research Council, The airliner cabin environment and the health of passengers and crew, National Academy Press, Washington, D.C., 2002, p.19.
- [5.4] E. H. Hunt and D. R. Space, The Airplane Cabin Environment-Issues Pertaining to Flight Attendant Comfort, International In-flight Service Management Organization Conference, Montreal, Canada, November, 1994.
- [5.5] A Torres, M. J.Utell and P.E.Morrow, Am J Respir Crit Care Med , 156 (1997) 728.
- [5.6] J. Lin, A. Kawai, T. Nakajima, Applied Catalysis B: Environmental 39 (2002) 157.
- [5.7] B. Dhandapani and S.T. Oyama, Appl. Cata. J. B, 11 (1997) 129.
- [5.8] R. Radhakrishnan, Structure and Ozone Decomposition Reactivity of Supported Manganese Oxide Catalysts, Ph.D. thesis, Virginia Polytechnic Institute and State University, Blacksburg, Virginia, 2001.
- [5.9] C. Heisig, W. Zhang and S. T. Oyama, Applied Catalysis B: Environmental 14 (1997) 117.

- [5.10] R.M. Heck, R.J. Farramo, H.C. Lee, Catal. Today, 13 (1992) 43.
- [5.11] R.M. Heck, S. Gulati, R.J. Farrauto, Chem. Eng. J, 82 (2001) 149.
- [5.12] J. L Williams, Catalysis Today, 69 (2001) 3.
- [5.13] E. Tronconi and A. Beretta, Catalysis Today, 52 (1991) 249.
- [5.14] M. Uberoi and C.J. Pereira, Ind. Eng. Chem. Res., 35 (1996) 113.
- [5.15] D.H. West, V. Balakotiah and Z. Jovanovic, Catalysis Today, 88 (2003) 3.
- [5.16] O. Levenspiel, Chemical Reaction Engineering, 3<sup>rd</sup> ed, John Wiley and Sons, Inc., New York, 1999.
- [5.17] D. R. Cahela and B. J. Tatarchuk, Catalysis Today, 69 (2001) 33.
- [5.18] D.K. Harris, D.R. Cahela and B.J. Tatarchuk, Composites Part A: App. Sci. & Manufacturing, 32 (2001) 1117.
- [5.19] R. Pfeffer, I&EC Fundamentals, 3 (1964) 380.
- [5.20] A. Kołodziej and J. Łojewska, Catalysis Today, 105 (2005) 378.
- [5.21] [http://www.catalysts.basf.com/Main/environmental/stationary\\_sources/indoor\\_air\\_quality/ozone\\_catalysts](http://www.catalysts.basf.com/Main/environmental/stationary_sources/indoor_air_quality/ozone_catalysts) (BASF DEOXO catalytic ozone converter – Product Information)
  
- [6.1] H. S. Fogler, Elements of Reaction Engineering, 3<sup>rd</sup> ed, Prentice Hall PTR, New Jersey, 1999.
- [6.2] O. Levenspiel, Chemical Reaction Engineering, 3<sup>rd</sup> ed, John Wiley and Sons, Inc., New York, 1999.
- [6.3] M. F. Edwards and J. F. Richardson, Chem. Eng. Sci., 23 (1968) 109.



- [6.4] R. B. Bird, W. E. Stewart & E. N. Lightfoot, Transport Phenomena, John Wiley & Sons Inc., New York, 2002, p.99.
- [6.5] R. L. Panton, Incompressible Flow, 2<sup>nd</sup> Ed., John Wiley and Sons, New York, 1996 p. 359.
- [6.6] [http://en.wikipedia.org/wiki/Buckingham\\_%CF%80\\_theorem](http://en.wikipedia.org/wiki/Buckingham_%CF%80_theorem)
- [6.7] P.N. Dwivedi and S.N. Upadaya, Ind. Eng. Chem., Process Des. Dev., 16, (1977) 157.
- [6.8] H. Yang, Gas phase desulfurization using regenerable microfibrous entrapped metal oxide based sorbents for logistic fuel cell applications, Ph.D. Thesis, Auburn University, Auburn, AL, 2007.
- [6.9] M.R. Karanjikar, Low temperature oxidation of CO using microfibrous entrapped catalysts for fire escape mask application, Ph.D. Dissertation, Auburn University, Auburn, AL, 2005.
- [6.10] Duggirala, R. K., Roy, C. J., Saeidi, S. M., Khodadadi, J. M., Cahela, D. R., and Tatarchuk, B. J., Chem. Eng. Sci. (2005).
- [6.11] Pressure Drop Prediction in Microfibrous Flows using CFD. AIAA 17<sup>th</sup> Computational Fluid Dynamics Conference, AIAA (2005) 4618.
- [6.12] Fluent 6.3 user guide, Fluent Inc, Lebanon, NH, 2006.
- [6.13] C. J. Roy, J. of Comp. Physics, 205 (2005) 131.
- [6.14] P. J. Roache, Fundamentals of Computational Fluid Dynamics, Hermosa Publishers, New Mexico, 1998, p.487.

## **APPENDICES**

## Appendix 1. Matlab Program to Simulate Hexane Breakthrough Curves

```
% Q=KC^(1/nr) First order in time...4kmax X 4kmax Matrix solution
clear; clc; tic
global GDT2 ABC2 kmax nr
L=0.0055; Uo=0.0743; dil=1;
dia_par=211e-6; Phi=0.65;
Ko=136750; nr=6.5;
nu=1.56e-5; Dm=.835e-5; Dp=1.32e-6;
Xads=.30; Xfib=0.075; void=1-Xfib-Xads; dpfib=19e-6;

Xmax=1; Xmin=0;          % Max & Min X value
nmax=1200*1;             % # of grid Points in t
kmax=101;                % # of grid Points in x
DX=(Xmax-Xmin)/(kmax-1); DT=80/1/dil;
step=nmax/300;

dpeff=dia_par*Phi;
Uin=Uo/void; Leff=L*dil*0.57/Xads; ac=6/dpeff;
Re=dpeff*Uo/nu; Sc=nu/Dm; Pedp=Re*Sc;          % Peclet Number
Gama = (1-void)^(1/3); W = 2-3*Gama+3*Gama^5-2*Gama^6;
Sh = 1.26*((1-Gama^5)/W*Pedp)^(1/3) % Sherwood Number(Pfeffer's equation)
km=Sh*Dm/dpeff; kp=60*Dp/dpeff^2/Ko;

ReSc=Uo*dia_par/Dm
Pe_inf=6.7*dpeff*100;
Gama1 = 0.45+0.55*void;
Beta=1;
Pedp=1/(Gama1*void/ReSc+dil/Pe_inf/(1+dil*Beta*Gama1*void/ReSc));

Km=km*ac*Leff/Uin*DT; Kp=kp*Leff/Uin*DT;
Kk=Kp*Ko/Km; PeL=Pedp*Leff/dia_par

r=DT/(PeL*DX^2); s=DT/(2*DX); q=Xads/void/dil*Km;
a=(-r-s);          % Diagnol Below Body diagonol
b=(2*r+q+1);       % Body Diagnol elements
c=(s-r);           % Diagnol Above Body Diagnol

Y(1:4*kmax,1)=0;
Yexit(nmax,2)=0;

A=ones(kmax,1);
ABC2=spdiags([a*A b*A c*A], -1:1,kmax,kmax);
ABC2(1,1)=1+DX*PeL; ABC2(1,2)=-1;
ABC2(kmax,kmax-1)=-1; ABC2(kmax,kmax)=1;          % BC
```

```

for k=1:kmax
    ABC2(k,kmax+k)= -q;
    ABC2(kmax+k, k)=1;
    ABC2(kmax+k, kmax+k)= -1;
    ABC2(kmax+k, 2*kmax+k)=-Kk;
    ABC2(kmax+k, 3*kmax+k)=Kk;
    ABC2(2*kmax+k, kmax+k)=1;
    ABC2(3*kmax+k,2*kmax+k)=-Kp;
    ABC2(3*kmax+k,3*kmax+k)=(1+Kp);
end

for k=1:kmax-1:kmax
    ABC2(k,kmax+k)=0;
    ABC2(kmax+k,k)=0;
end

GD(1,1)=DX*PeL;
GD(2:4*kmax,1)=0;

Flag=0;
Area=DT/3;

for n=1:nmax
    GD(2:kmax-1,1)= Y(2:kmax-1,1);
    GD(3*kmax+2:4*kmax-1,1)=Y(3*kmax+2:4*kmax-1,1);
    GDt2=GD;
    options=optimset('Display','off');
    Y = fsolve(@AdsFreFun3,Y,options); % Call optimizer
    Yexit(n,2) =Y(kmax);

    if (mod(n,2)==0)
        Area=Area+(1-Y(kmax))*DT*4/3;
    else
        Area=Area+(1-Y(kmax))*DT*2/3;
    end

    if Flag == 0
        if Y(kmax)>=.01
            Flag=1;
            BTtime=(n-1)+1/(Y(kmax)-BTY)*(0.01-BTY);
            BTArea=BTAreat+(Area-BTAreat)/(Y(kmax)-BTY)*(0.01-BTY);
        else
            BTY=Y(kmax);
            BTAreat=Area;
        end
    end
end

```

```

    end
end

if (mod(n,step)==0)
    iter=n/step
    toc
end
end

BTCap=BTArea/Area*100           %Percentage Breakthrough capacity
KoEst=Area*void/Xads*dil
BTtime=BTtime*DT*Leff/Uin/60*Ko/KoEst
Yexit(:,1)=(1:nmax)*DT*Leff/Uin/60*Ko/KoEst;

for m=1:(nmax/step)
    Yexit2(m,:)=Yexit(m*step,:);
end

ToTime=toc
save('AdsFre6MEFC')

```

## Appendix 2. Matlab Programs for Reactor Comparisons for Ozone Conversion

### 2(a) Packed Beds

```
% PACKED BED REACTOR
clear; clc
T = 394; P0 = 101325; % Inlet Temperature(K)and Pressure(Pa)
kr = 1.769e8*exp(-21.05e3/8.314/T) % Reaction rate Const(1/s)
Rho = P0*29/(8314*T); % Density(kg/m3)
Mu =(0.740252+T*0.734642+T^2*(-0.00045)+T^3*1.37e-7)*1e-7 % Air Viscosity
(kg/m.s)
MAB = 2*(48*29/(48+29)); va=6.11*3; vb=19.7;
D = 0.00143e-4*T^1.75/(P0/101325*MAB^0.5*(va^0.3333+vb^0.3333)^2) % Ozone
Diffusivity in Air(m2/s)
Sc = Mu/(Rho*D); % Schmidt Number
De = D*0.6/2; % Effective Pore diffusivity inside catalyst support
Sph = 0.7; % Particle Shape factor
V0 = [5; 10; 15; 20];
L=0.02;

disp('PKD')
void = 0.40; % Bed voidage
dpPkd = [0.167 0.3 0.5 0.75 2]*1e-3; % Particle diameter(m)
for l = 1:length(dpPkd)
    dp=dpPkd(l)*Sph;
    PDT = (150*Mu*V0/dp^2*(1-void)^2/void^3+1.75*Rho*V0.^2/dp*(1-
void)/void^3)*L^2/Rho./V0.^2;% Pressure Drop("H2O/1cm Bed length)
    PDPkd(:,l)=PDT;

    ac = 6/dp; % External Area per unit catalyst volume of
catalyst(m2/m3)
    Re = dp*V0*Rho/Mu; % Reynolds Number
    Sh =(1-void)^0.5/void*Sc^(1/3)*Re.^(1/2); % Sherwood number
    kg = Sh*D/dp; % External Mass Transfer Coeff.(m/s)
    Phi = (kr/De)^.5 *(dp/6); % Thiele Modulus
    Eta = 1/3/Phi^2*(3*Phi*coth(3*Phi)-1);% Internal Effectiveness Factor
    keff = 1/(Eta*kr)+1./(kg*ac); keff=1./keff;

    kgPkd(:,l)=kg*ac;
    EtaPkd(:,l)=Eta;
    keffPkd(:,l)=keff;
    XPkd(:,l)=keff*(1-void)*L./V0./PDT
end
```

## Appendix 2(b). Monoliths

```

clear; clc
T = 394; P0 = 101325; % Inlet Temperature(K)and Pressure(Pa)
kr = 1.769e8*exp(-21.05e3/8.314/T) % Reaction rate Const(1/s)
Rho = P0*29/(8314*T); % Density(kg/m3)
Mu = (0.740252+T*0.734642+T^2*(-0.00045)+T^3*1.37e-7)*1e-7 % Air Viscosity
(kg/m.s)
MAB = 2*(48*29/(48+29)); va=6.11*3; vb=19.7;
D = 0.00143e-4*T^1.75/(P0/101325*MAB^0.5*(va^0.3333+vb^0.3333)^2) % Ozone
Diffusivity in Air(m2/s)
Sc = Mu/(Rho*D); % Schmidt Number
De = D*0.6/2 % Effective Pore diffusivity inside catalyst support
V0 = [5; 10; 15; 20];
L=0.0254*10;

% MONOLITHS
for l=1:5
    switch l
        case {1}
            Cpsi=100; tw=381; % Cells per Square inch & Wall Thickness
        case {2}
            Cpsi=200; tw=267; % Cells per Square inch & Wall Thickness
        case {3}
            Cpsi=400; tw=152.4; % Cells per Square inch & Wall Thickness
        case {4}
            Cpsi=400; tw=102; % Cells per Square inch & Wall Thickness
        case {5}
            Cpsi=900; tw=51; % Cells per Square inch & Wall Thickness
    end
    tc=25; % Washcoat thickness (micron)
    dch = (25.4e3/(Cpsi)^.5-tw-2*tc) % Monolith channel Dia(micron)
    ac = 4*dch/((dch+tc)*4*tc)*1e6; % External Area per unit catalyst volume of
    catalyst(m2/m3)
    void = (dch/(dch+tw+2*tc))^2 % Fractional area open
    CatVol = 4*(dch+tc)*tc/(dch+tw+2*tc)^2
    tc = tc*1e-6; % SI UNIT Conversion
    dch = dch*1e-6;
    Phi = (kr/De)^.5 *tc; % Thiele Modulus
    Eta = 1/Phi*tanh(Phi); % Internal Effectiveness Factor

    Vch = V0/void; % Velocity in the Channel
    Re = dch*Vch*Rho/Mu; % Monolith Reynolds No.
    for p=1:4
        if Re(p,1)<=1000

```

```

    f(p,1) = 13/Re(p,1);          % Friction factor in Monolith
    else
    f(p,1) = .031/Re(p,1)^(0.12);
    end
end
PDT1=(4*f*L/void^2/dch); PDT=PDT1;
PDT2=2*(1-void^2)/void^2;        % Pressure Drop in Monolith("H2O/cm of bed
Length)
PDT=PDT1;%+PDT2;
PDMonT(:,l)=PDT;

Gz = Re*Sc*dch/L;                % Graetz Number
Sh = 2.976 + 8.827 * (1000./Gz).^(-0.545).*exp(-48.2./Gz);
kg = Sh*D/dch^2;
keff = 1/(Eta*kr)+1./(kg*ac); keff=1./keff;

kgMon(:,l)=kg*ac;
EtaMon(:,l)=Eta;
keffMonC(:,l)=keff;
keffMonR(:,l)=keff*CatalVol;
XMon(:,l)=keff*CatalVol*L/V0./PDT
Voidage(:,l)=void;
CatalLoad(:,l)=CatalVol;
end

```



## Appendix 2(c). MFECS

```

clear; clc
T = 394; P0 = 101325; % Inlet Temperature(K)and Pressure(Pa)
kr = 1.769e8*exp(-21.05e3/8.314/T) % Reaction rate Const(1/s)
Rho = P0*29/(8314*T); % Density(kg/m3)
Mu =(0.740252+T*0.734642+T^2*(-0.00045)+T^3*1.37e-7)*1e-7 % Air Viscosity
(kg/m.s)
MAB = 2*(48*29/(48+29)); va=6.11*3; vb=19.7;
D = 0.00143e-4*T^1.75/(P0/101325*MAB^0.5*(va^0.3333+vb^0.3333)^2) % Ozone
Diffusivity in Air(m2/s)
Sc = Mu/(Rho*D); % Schmidt Number
De = D*0.6/2; % Effective Pore diffusivity inside catalyst support
Sph = 0.7; % Particle Shape factor
V0 = [5; 10; 15; 20];
L=0.003;

%MICROFIBROUS MATERIAL
dpMtl1 = 9.8e-6; % Metal Microfiber Diameter
dpMtl2 = 7.6e-6; % Metal Microfiber Diameter
dp = 163e-6*Sph; % Adsorbent Particle Diameter
MtlFrac1 = 0.006; % Metal Vol Fraction
MtlFrac2 = 0.006; % Metal Vol Fraction
CatFrac = 0.136; % Adsorbent Vol Fraction
VoidFrac = 1-MtlFrac1-MtlFrac2-CatFrac; % Void Fraction
Tau = 1+(1-VoidFrac)/2; % Tortuosity
FpAng = pi()/4; % Flow Path Angle Pi/4 or 45
%dpAvg = (1-VoidFrac)/(MtlFrac/(1.5*dpMtl)+AdsFrac/(sph*dpAds));
xiMtl1=MtlFrac1/(1-VoidFrac);
xiMtl2=MtlFrac2/(1-VoidFrac);
xiAds=CatFrac/(1-VoidFrac);
term1 = xiMtl1/(1.5*dpMtl1)+xiMtl2/(1.5*dpMtl2)+xiAds/(dp);
term2 = xiMtl1/(1.5*dpMtl1)^2+xiMtl2/(1.5*dpMtl2)^2+xiAds/(dp)^2;
xFD = VoidFrac^2/12/(1-VoidFrac);
ac=6/dp; % External Surface Area per unit Volume of Catalyst

Gama = (1-VoidFrac)^(1/3);
W = 2-3*Gama+3*Gama^5-2*Gama^6; % W factor in pfeffer's article
Phi = (kr/De)^.5 *(dp/6); % Thiele Modulus
Eta = 1/3/Phi^2*(3*Phi*coth(3*Phi)-1); % Internal Effectiveness Factor
PD1 = (72*Tau^2*Mu*(1-
VoidFrac)^2/(cos(FpAng))^2/VoidFrac^3*(term1^2+xFD*term2));
PD2 = (6*Tau^3*Rho*(1-VoidFrac)/VoidFrac^3/2/(cos(FpAng))^3*term1*(0.174+(0.6-
0.174)/4*VoidFrac));
PleatFac = [1 2 3 4 5]; % Pleat Factor

```

```

for l=1:length(PleatFac)
    Veff = V0/PleatFac(l);           % Effective Velocity
    PDT = (PD1*Veff+PD2*Veff.^2)*L^2/Rho./V0.^2;
    PDCm32(:,l)=(Rho*V0.^2*(1-(1/PleatFac(l)^2)))/(9.8*25.4); % Pressure Drop in
Mcr(mm of H2O/5mm of bed Length)
    PDCm3(:,l)=PDT;

    Re = dp*Veff*Rho/Mu;             % Reynolds Number
    Pe = Re*Sc;                      % Peclet Number
    Sh = 1.26*((1-Gama^5)/W.*Pe).^(1/3); % Sherwood Number
    kg = Sh*D/dp;
    keff = 1/(Eta*kr)+1./(kg*ac); keff=1./keff;

    kgCm3(:,l)=kg*ac;
    EtaCm3(:,l)=Eta;
    keffCm3C(:,l)=keff;
    keffCm3R(:,l)=keff*CafFrac;
    XCm3(:,l)=keff*CafFrac*L*PleatFac(l)./V0./PDT
    Voidage(:,l)=VoidFrac;
End

```

### Appendix 3(a). FLUENT Journal File for Creating Planes in the Channel Geometry

```
/surface
(define a 0.0)
(define b 0.4)
line-surface
Plane-1
a 0 a b
line-surface
Plane-2
(+ a 0.1) 0 , b
line-surface
Plane-3
(+ a 0.2) 0 , b
line-surface
Plane-4
(+ a 0.3) 0 , b
line-surface
Plane-5
(+ a 0.4) 0 , b
line-surface
Plane-6
(+ a 0.5) 0 , b
line-surface
Plane-7
(+ a 0.6) 0 , b
line-surface
Plane-8
(+ a 0.7) 0 , b
line-surface
Plane-9
(+ a 0.8) 0 , b
line-surface
Plane-10
(+ a 0.9) 0 , b
line-surface
Plane-11
(+ a 1.0) 0 , b
q
```

### Appendix 3(b). FLUENT Journal File for Obtaining Velocity Profiles for various Re

```
(define iter 5000)
(define MFR 0.018948)
(define PG -10000)
;-----
; CHANGE INLET VELOCITY - TO ALTER Re# to 1000
/define/pc/massflow
(/ MFR 1) (/ PG 1) 0.5 2 313 1 0
; INITIALIZE SOLUTION
/solve/initialize/initialize-flow
Y
; ITERATE
/solve/iterate
iter
; WRITING CASE & DATA FILES
wcd Period_Rel1000
Y
; WRITING PROFILE
/file/wrpr
ProfRel1000
3 ,
x-vel
y-vel
q
;-----
; CHANGE INLET VELOCITY - TO ALTER Re# to 100
/define/pc/massflow
(/ MFR 10) (/ PG 10) 0.5 2 313 1 0
; INITIALIZE SOLUTION
/solve/initialize/initialize-flow
Y
; ITERATE
/solve/iterate
iter
; WRITING CASE & DATA FILES
wcd Period_Rel100
Y
; WRITING PROFILE
/file/wrpr
ProfRel100
3 ,
x-vel
y-vel
q
;-----
; CHANGE INLET VELOCITY - TO ALTER Re# to 10
/define/pc/massflow
(/ MFR 100) (/ PG 100) 0.5 2 313 1 0
; INITIALIZE SOLUTION
/solve/initialize/initialize-flow
Y
; ITERATE
/solve/iterate
iter
```

```

; WRITING CASE & DATA FILES
wcd Period_Re10
Y
; WRITING PROFILE
/file/wrpr
ProfRe10
3 ,
x-vel
y-vel
q
;-----
; CHANGE INLET VELOCITY - TO ALTER Re# to 1
/define/pc/massflow
(/ MFR 1000) (/ PG 1000) 0.5 2 313 1 0
; INITIALIZE SOLUTION
/solve/initialize/initialize-flow
Y
; ITERATE
/solve/iterate
iter
; WRITING CASE & DATA FILES
wcd Period_Re1
Y
; WRITING PROFILE
/file/wrpr
ProfRe1
3 ,
x-vel
y-vel
q
;-----
; CHANGE INLET VELOCITY - TO ALTER Re# to 0.1
/define/pc/massflow
(/ MFR 10000) (/ PG 10000) 0.5 2 313 1 0
; INITIALIZE SOLUTION
/solve/initialize/initialize-flow
Y
; ITERATE
/solve/iterate
iter
; WRITING CASE & DATA FILES
wcd Period_Re0-1
Y
; WRITING PROFILE
/file/wrpr
ProfRe0-1
3 ,
x-vel
y-vel
q
;-----
; CHANGE INLET VELOCITY - TO ALTER Re# to 0.01
/define/pc/massflow
(/ MFR 100000) (/ PG 100000) 0.5 2 313 1 0
; INITIALIZE SOLUTION

```

```
/solve/initialize/initialize-flow
Y
; ITERATE
/solve/iterate
iter
; WRITING CASE & DATA FILES
wcd Period_Re0-01
Y
; WRITING PROFILE
/file/wrpr
ProfRe0-01
3 ,
x-vel
y-vel
q
;-----THE END-----
```

### Appendix 3(c). FLUENT Journal File for Running Various Re-Sc Cases in Channel

#### Geometry

```
(define iter 5000)
(define iter2 2000)
;-----
; CHANGE INLET VELOCITY - TO ALTER Re#1000
/file/rpr
ProfRe1000
/solve/set/equ/flow/y
; INITIALIZE SOLUTION
/solve/initialize/initialize-flow
Y
;-----
; CHANGE MATERIAL PROPERTIES - DIFFUSIVITY - TO ALTER Sc#
/define/materials/change-create
mixture-template
, , , , , , Y , , 3.37e-5 , ,
; ITERATE
/solve/iterate
iter
; WRITING CASE & DATA FILES
wcd Sc0.5_Re1000
; WRITING MASS FRACTION FILES
/report/surface-integral/mass-weighted-avg
2
3
5
6
7
8
9
10
11
12
13
14
15

c6h14
Y
Conc_Re1000.xls
Y
;-----
/solve/set/equ/flow/n
; CHANGE MATERIAL PROPERTIES - DIFFUSIVITY - TO ALTER Sc#
/define/materials/change-create
mixture-template
, , , , , , Y , , 8.41e-6 , ,
; ITERATE
/solve/iterate
```





8  
9  
10  
11  
12  
13  
14  
15

```
c6h14
Y
Conc_Re100.xls
Y
;-----
/solve/set/equ/flow/n
; CHANGE MATERIAL PROPERTIES - DIFFUSIVITY - TO ALTER Sc#
/define/materials/change-create
mixture-template
, , , , , , Y , , 8.41e-6 , ,
; ITERATE
/solve/iterate
iter2
; WRITING CASE & DATA FILES
wcd Sc2.0_Re100
; WRITING MASS FRACTION FILES
/report/surface-integral/mass-weighted-avg
, , , , , , , , , , , , , , , ,
```

```
c6h14
Y
Conc_Re100.xls
Y
;-----
; CHANGE MATERIAL PROPERTIES - DIFFUSIVITY - TO ALTER Sc#
/define/materials/change-create
mixture-template
, , , , , , Y , , 3.37e-6 , ,
; ITERATE
/solve/iterate
iter2
; WRITING CASE & DATA FILES
wcd Sc5.0_Re100
; WRITING MASS FRACTION FILES
; WRITING MASS FRACTION FILES
/report/surface-integral/mass-weighted-avg
, , , , , , , , , , , , , , , ,
```

```
c6h14
Y
Conc_Re100.xls
Y
;-----
;-----
; CHANGE INLET VELOCITY - TO ALTER Re#10
/file/rpr
```



```

; CHANGE MATERIAL PROPERTIES - DIFFUSIVITY - TO ALTER Sc#
/define/materials/change-create
mixture-template
, , , , , , Y , , 3.37e-6 , ,
; ITERATE
/solve/iterate
iter2
; WRITING CASE & DATA FILES
wcd Sc5.0_Re10
; WRITING MASS FRACTION FILES
/report/surface-integral/mass-weighted-avg
, , , , , , , , , , , , , , , ,

c6h14
Y
Conc_Re10.xls
Y
;-----
(define iter 8000)
(define iter2 5000)
;-----
; CHANGE INLET VELOCITY - TO ALTER Re#1
/file/rpr
ProfRe1
/solve/set/equ/flow/y
; INITIALIZE SOLUTION
/solve/initialize/initialize-flow
Y
;-----
; CHANGE MATERIAL PROPERTIES - DIFFUSIVITY - TO ALTER Sc#
/define/materials/change-create
mixture-template
, , , , , , Y , , 3.37e-5 , ,
; ITERATE
/solve/iterate
iter
; WRITING CASE & DATA FILES
wcd Sc0.5_Re1
; WRITING MASS FRACTION FILES
/report/surface-integral/mass-weighted-avg
2
3
5
6
7
8
9
10
11
12
13
14
15

c6h14

```

```

Y
Conc_Rel.xls
Y
;-----
/solve/set/equ/flow/n
; CHANGE MATERIAL PROPERTIES - DIFFUSIVITY - TO ALTER Sc#
/define/materials/change-create
mixture-template
, , , , , , Y , , 8.41e-6 , ,
; ITERATE
/solve/iterate
iter2
; WRITING CASE & DATA FILES
wcd Sc2.0_Rel
; WRITING MASS FRACTION FILES
/report/surface-integral/mass-weighted-avg
, , , , , , , , , , , , , ,

c6h14
Y
Conc_Rel.xls
Y
;-----
; CHANGE MATERIAL PROPERTIES - DIFFUSIVITY - TO ALTER Sc#
/define/materials/change-create
mixture-template
, , , , , , Y , , 3.37e-6 , ,
; ITERATE
/solve/iterate
iter2
; WRITING CASE & DATA FILES
wcd Sc5.0_Rel
; WRITING MASS FRACTION FILES
/report/surface-integral/mass-weighted-avg
, , , , , , , , , , , , , ,

c6h14
Y
Conc_Rel.xls
Y
;-----
;-----
; CHANGE INLET VELOCITY - TO ALTER Re#0.1
/file/rpr
ProfRe0-1
/solve/set/equ/flow/y
; INITIALIZE SOLUTION
/solve/initialize/initialize-flow
Y
;-----
; CHANGE MATERIAL PROPERTIES - DIFFUSIVITY - TO ALTER Sc#
/define/materials/change-create
mixture-template
, , , , , , Y , , 3.37e-5 , ,
; ITERATE

```

```

/solve/iterate
iter
; WRITING CASE & DATA FILES
wcd Sc0.5_Re0.1
; WRITING MASS FRACTION FILES
/report/surface-integral/mass-weighted-avg
2
3
5
6
7
8
9
10
11
12
13
14
15

c6h14
Y
Conc_Re0_1.xls
Y
;-----
/solve/set/equ/flow/n
; CHANGE MATERIAL PROPERTIES - DIFFUSIVITY - TO ALTER Sc#
/define/materials/change-create
mixture-template
, , , , , Y , , 8.41e-6 , ,
; ITERATE
/solve/iterate
iter2
; WRITING CASE & DATA FILES
wcd Sc2.0_Re0.1
; WRITING MASS FRACTION FILES
/report/surface-integral/mass-weighted-avg
, , , , , , , , , , , , , , , ,

c6h14
Y
Conc_Re0_1.xls
Y
;-----
; CHANGE MATERIAL PROPERTIES - DIFFUSIVITY - TO ALTER Sc#
/define/materials/change-create
mixture-template
, , , , , Y , , 3.37e-6 , ,
; ITERATE
/solve/iterate
iter2
; WRITING CASE & DATA FILES
wcd Sc5.0_Re0.1
; WRITING MASS FRACTION FILES
/report/surface-integral/mass-weighted-avg

```



```

wcd Sc2.0_Re0.01
; WRITING MASS FRACTION FILES
/report/surface-integral/mass-weighted-avg
, , , , , , , , , , , , , , , ,

c6h14
Y
Conc_Re0_01.xls
Y
;-----
; CHANGE MATERIAL PROPERTIES - DIFFUSIVITY - TO ALTER Sc#
/define/materials/change-create
mixture-template
, , , , , , Y , , 3.37e-6 , ,
; ITERATE
/solve/iterate
iter2
; WRITING CASE & DATA FILES
wcd Sc5.0_Re0.01
; WRITING MASS FRACTION FILES
/report/surface-integral/mass-weighted-avg
, , , , , , , , , , , , , , , ,

c6h14
Y
Conc_Re0_01.xls
Y
;-----THE END-----

```